Evaluation of the ECM Structures of Fibrotic Tissues by Using Raman Microspectroscopy

Dissertation

der Mathematisch-Naturwissenschaftlichen Fakultät
der Eberhard Karls Universität Tübingen
zur Erlangung des Grades eines
Doktors der Naturwissenschaften
(Dr. rer. nat.)

vorgelegt von
Chuan-En Lu
aus Taipei/Taiwan

Tübingen
2023

Gedruckt mit Genehmigung der Mathematisch-Naturwissenschaftlichen Fakultät der Eberhard Karls Universität Tübingen.

Tag der mündlichen Qualifikation:	01.08.2023
Dekan:	Prof. Dr. Thilo Stehle
1. Berichterstatterin:	Prof. Dr. Katja Schenke-Layland
2. Berichterstatter:	Prof. Dr. Peter Loskill

Table of Contents

List of figures

List of publications

Publications related to thesis

[§]: Authors contributed equally

1. **Chuan-En Lu**, Ruth E Levey, Giulio Ghersi, Nathan Shueller, Simone Liebscher, Shannon L. Layland, Katja Schenke-Layland, Garry P. Duffy, Julia Marzi. Monitoring the macrophage response towards biomaterial implants using label-free imaging. Materials Today Bio Volume 21, August 2023, 100696.

2. Lucas Becker[§], **Chuan-En Lu[§]**, Ivonne Aidee Montes-Mojarro, Suzan Khalil, Ali Nsair, Falko Fend, Julia Marzi, Katja Schenke-Layland. Raman Microspectroscopy Identifies Fibrotic Tissues in Collagen-related Disorders via Deconvoluted Collagen Type I Spectra. Acta Biomater. 2023 Mar 15; S1742-7061(23)00150-2.

3. Rachel Beatty[§], **Chuan-En Lu[§]**, Julia Marzi, Ruth E Levey, Daniel A. Carvajal Berrio, Giulia Lattanzi, Robert Wylie, Raymond O'Connor, Eimear Wallace, Eimear B Dolan, Shannon L. Layland, Katja Schenke-Layland, Garry P Duffy. The Foreign Body Response to an Implantable Therapeutic Reservoir in a Diabetic Rodent Model. Tissue Eng Part C Methods. 2021 Oct; 27(10):515-528.

Additional publications

1. Jeyagaran Abiramy[§], **Chuan-En Lu[§]**, Aline Zbinden, Andreas L. Birkenfeld, Sara Y. Brucker, Shannon L. Layland. Type 1 Diabetes and Engineering Enhanced Islet Transplantation. Advanced Drug Delivery Reviews. 2022 Aug 21; 114481.

2. Max Urbanczyk[§], Abiramy Jeyagaran[§], Aline Zbinden, **Chuan-en Lu**, Julia Marzi, Shannon L. Layland, Garry P. Duffy, Katja Schenke-Layland. Decorin improves pancreatic β-cell function and regulates ECM expression in vitro. Matrix Biol. 2022 Dec 30: S0945-053X(22)00154-8.

Contribution

No.	1	2	3
Publication status	Published	Published	Published
Number of authors	11	10	13
Position of the candidate in the list of authors	1	Shared 1st authorship	Shared 1st authorship
Scientific ideas by the candidate (%)	35%	30%	25%
Data generation (%)	60%	30%	50%
Interpretation and analysis by candidate (%)	45%	30%	45%
Paper writing by candidate (%)	60%	30%	40%

List of Abbreviations

αSMA	α smooth muscle actin
AGE	advanced glycation end product
CT	computed tomography
Col I	collagen type I
Col III	collagen type III
ECM	extracellular matrix
FBR	foreign body response
HSP47	heat shock protein 47
IF	immunofluorescence
IL	interleukin
LDA	linear discriminant analysis
MRI	magnetic resonance imaging
MVA	multivariate analysis
NLOI	nonlinear optical imaging
PCA	principal component analysis
PDGF	platelet-derived growth factor
PSR	picrosirius red staining
PVDF	polyvinylidene fluoride
RMS	Raman microspectroscopy
ROS	reactive oxygen species
SHG	second harmonic generation
STZ	streptozotocin
TCA	true component analysis
TGFβ	transforming growth factor β
TPU	thermoplastic polyurethane
TNFα	tumor necrosis factor α

Abstract

Fibrosis is a pathological process of excessive extracellular matrix (ECM) proteins deposition within tissues undergoing chronic inflammation. Fibrosis is highly related to a wide range of disorders across every organ and can cause negative effects on disease prognosis as well as life expectancy. It can be caused by numerous stimuli including implantation, aging, cancer, repetitive tissue damage, or disorders which are highly relevant to the chronic inflammatory reaction. Implantable medical devices can cause fibrotic capsule formation, which is triggered by the foreign body response (FBR). Fibrotic capsules can physically interfere with medical devices, thereby reducing therapeutic outcomes. The diagnostic evaluation of tissue fibrosis relies on the examination of tissue biopsies by gold-standard histochemical analysis. The definition, location and characteristics of the area of the fibrotic tissue can induce bias between individual pathologists with different clinical experiences, expertise and knowledge. Moreover, the limitations of histological staining involve invasive biopsy procedures and staining artifacts, which may cause errors in diagnostic results. The thesis mainly focused on the establishment of a new fibrotic assessment of implantation-driven FBR in streptozotocin (STZ)-induced diabetic animal model by using Raman microspectroscopy (RMS). ECM compositions as well as pro-inflammatory and regenerative macrophage activation states were investigated. We demonstrated the capability of RMS to discriminate collagen type I (Col I) between diabetic and non-diabetic rodent models via advanced glycation end products (AGEs) which were integrated into collagen fibers in diabetic groups. Furthermore, in combination with multivariate analysis (MVA), we revealed that RMS can be used to discern pathological fibrotic tissues and healthy tissues via the secondary structural differences based on the Raman spectrum of Col I, which can provide a non-biased clinical assessment. In addition to ECM characterization, RMS has the potential for immune cell classification. Raman imaging was applied on tissue sections for immunophenotyping in accordance with the fluorescence-guided generation of M1/M2 macrophages. The classification was attributed to the differences in DNA methylation states in the nuclei between M1/M2 phenotypes. In conclusion, Raman imaging and microspectroscopy offer an advanced diagnostic approach to monitor the FBR and fibrosis investigation in a molecular-sensitive and marker-independent manner.

Zusammenfassung

Fibrotische Erkrankungen sind als pathologischer Prozess der übermäßigen Ablagerung von Proteinen der extrazellulären Matrix (EZM) im Bindegewebe eine irreversible Folge einer chronischen Entzündung. Fibrose steht in engem Zusammenhang mit einer Vielzahl von Erkrankungen in allen Organen und kann negative Auswirkungen auf die Krankheitsprognose sowie die Lebenserwartung haben. Fibrose kann durch zahlreiche Stimuli verursacht werden, einschließlich Implantation, Alterung, Krebs, wiederholte Gewebeschädigung oder chronische Entzündungen. Implantate können eine fibrotische Kapselbildung verursachen, die durch die Fremdkörperreaktion ausgelöst wird. Fibrotische Kapseln können die Funktionalität von Medizinprodukten physikalisch beeinträchtigen und dadurch die erwartete therapeutische Wirksamkeit verringern. Die diagnostische Beurteilung der Gewebefibrose beruht auf der Untersuchung von Gewebebiopsien durch histochemische Goldstandard-Analyse, welche je nach Lage und Eigenschaften von der individuellen Expertise des begutachtenden Pathologen abhängig sein kann. Darüber hinaus stellen histologische Färbungen invasive Biopsieverfahren dar und können durch Färbeartefakte zu Fehlern bei den diagnostischen Ergebnissen führen. Diese Dissertation beschäftigt sich mit der Etablierung einer neuen Methode zur Bewertung der implantationsgesteuerten Fremdkörperreaktion im Streptozotocin (STZ)-induzierten diabetischen Tiermodell unter Verwendung der Raman-Mikrospektroskopie (RMS). Die EZM-Zusammensetzungen sowie entzündliche und regenerative Aktivierungszustände von Makrophagen wurden untersucht. Wir haben das Potential der RMS gezeigt, Kollagen I zwischen diabetischen und nicht-diabetischen Nagetiermodellen über fortgeschrittene Glykosylierungs-Endprodukte zu unterscheiden, die in Kollagenfasern der Diabetes-Gruppe integriert waren. Darüber hinaus haben wir in Kombination mit multivariater Analyse gezeigt, dass RMS verwendet werden kann, um pathologische, fibrotische Gewebe und gesunde Gewebe zu unterscheiden. Raman Signaturen von Kollagen I weisen auf Unterschiede in der Sekundärstruktur hin, was auch von hoher klinischer Relevanz ist. Neben der EZM-Charakterisierung hat RMS das Potenzial für die Klassifizierung von Immunzellen. Die Raman-Bildgebung wurde auf Gewebeschnitte zur Immunphänotypisierung von M1/M2-Makrophagen angewendet. Die Klassifizierung wird Unterschieden in den

DNA-Methylierungsmustern zwischen M1/M2 zugeschrieben. Zusammenfassend bieten Raman-Bildgebung und Mikrospektroskopie einen fortschrittlichen diagnostischen Ansatz zur Überwachung der Fibroseuntersuchung auf molekularsensitive und markerunabhängige Weise.

Chapter 1

Introduction

1. Introduction

1.1. Tissue Fibrosis

The definition of tissue fibrosis is described as excessive scar tissue formation with abnormal ECM accumulation [1, 2]. The mechanism of pathways for fibrosis is mainly in response to inflammation and tissue damage [3]. Fibrotic diseases are a dynamic wound-healing process which normally results from the chronic inflammatory reaction induced by several triggers [4, 5]. The process of fibrosis involves inflammation, tissue remodeling, excessive collagen deposition with increasing expression of growth factors and proteolytic enzymes, followed by immune cell recruitment and activation within both innate and adaptive immune systems [5, 6]. Several types of immune cells including macrophages, neutrophils, natural killer cells, fibroblasts and myofibroblasts cells play critical roles in the ECM network [7]. ECM remodeling and deposition are favorable at the initial stage of wound repair processes; however, in tissue fibrosis, abnormal overproduction of ECM leads to excessive scar tissue formation [8]. Fibrosis can affect most organs in the body [9]. Healthy functional tissues can be replaced by progressive non-functional fibrotic tissues, which causes organ dysfunction or even worse – organ failure [10]. In the US, it has been reported that approximately 45% of deaths are highly associated with tissue fibrosis [11]. Although the mechanisms of fibrosis were widely investigated, no efficacious therapeutic regimen has been brought to the market to fully overcome pathological fibrogenesis [12, 13]. Moreover, the identification of fibrotic disorders is often at a late stage owing to diagnostic delay [14, 15]. One of the reasons is that the extent of the fibrosis deteriorates to a threshold which can provoke severe symptoms [16-18]. Current investigation methods are limited to visualization of tissue morphology, geometry and fibrillar collagen quantification, which impede the patients from receiving punctual therapies [19]. It has been reported that earlier diagnosis and treatment of several fibrotic diseases can significantly improve the prognosis and survival of patients [18, 20, 21]. Therefore, novel diagnostic tools for early-stage fibrosis detection are urgently required.

1.1.1. The Foreign Body Response-induced Fibrosis at the Subcutaneous Location

Medical implants have revolutionized the field of biomedical engineering and widely benefited the clinics in the areas of tissue regeneration and reconstruction, artificial pacemakers, biosensors as well as sustained drug release systems [22]. Nonetheless, even though countless patients have been benefited from implantable medical devices, foreign objects implanted in the body can provoke immunological responses and tissue repair reactions, which is well known as the FBR and inevitably induces tissue fibrosis [23]. The FBR at the subcutaneous interposition is similar to other implantation sites in the body [24, 25]. Once a foreign object is implanted, it causes damage to the surrounding tissues, inducing a cascade of reactions. There are two phases of the FBR process – acute inflammatory and chronic inflammatory (fibrous) stages [26, 27].

The first stage of the acute inflammatory reaction can occur rapidly after implantation [28]. It is initiated with unspecific protein adhesion on the surface of biomaterials to form an early provisional ECM [29]. These proteins are mostly from the blood serum and interstitial fluid, including fibronectin, vitronectin, albumin, globulin, fibrinogen and factor XII [30]. The composition of the matrix can result in different cellular responses toward the foreign body [31]. Therefore, the ideal properties on the surface can attract more defined proteins to present on the surface in favor of proper cellular interaction to mitigate fibrotic reaction [32]. The adsorbed proteins are recognized by several immune cells, which allow those cells to be attached to the surface. Apart from the presence of the implants with unspecific proteins, chemoattractant factors which are secreted by platelets and injured tissues further recruit neutrophils to accumulate in the injured region [33]. The neutrophils release reactive oxygen species (ROS), proteases as well as neutrophil extracellular traps and immune-regulatory cytokines. Physiologically, the main role of neutrophils is to provide first-line protection against pathogen invasion [34]. In the case of device implantation, the neutrophils can recruit additional immune cells as well as secrete the factors which aim for the degradation of the foreign objects [28, 35]. The monocytes are recruited to the site and undergo activation and differentiation into macrophages in response to the signals released by the neutrophils [36]. Macrophages can be classified into two

subsets with different functionalities – M1 and M2 macrophages [37, 38]. Until now, the classification of M1 and M2 is only based on in vitro settings [37, 38]. The in vivo condition is much more complex. Therefore, the spectrum of the subsets of these macrophages is grouped as “M1-like” and “M2-like” populations [39]. Proinflammatory macrophages are known as “M1-like” which predominate the macrophage population at the beginning. M1-like macrophages play a crucial role in the inflammatory reaction and proinflammatory cytokine secretion including tumor necrosis factor α (TNFα), interleukins (IL)-1b, IL-6, IL-8, proteolytic enzyme and ROS [40]. The attached macrophages undergo dynamic intracellular cytoskeleton remodeling, modulating morphological alterations, which induces elongation and flattening to adhere to the surface for the purpose of biomaterial degradation and phagocytosis [41, 42]. When the implanted biomaterials are degraded or eliminated successfully, the immunological reaction can be terminated at this stage [43].

However, the acute inflammatory reaction can be incapable of removing or breaking down the foreign object, which is so-called “frustrated phagocytosis” [44]. In this case, the second stage of the chronic inflammatory (fibrous) stage would occur. The population of M1-like macrophages progressively undergoes a transition to M2-like macrophages. M2-like phenotypes release anti-inflammatory mediators such as IL-10 and transforming growth factor β (TGFβ) and platelet-derived growth factor (PDGF) in an attempt to repair the wound and remodel the ECM components [45-47]. Another critical role of TGFβ is the recruitment, activation and proliferation of fibroblasts, which generate new ECM to encapsulate the implantation [46]. The fibroblasts can further differentiate into myofibroblasts, which is known as the fibroblast-to-myofibroblast transition. Myofibroblasts play the main role in tissue repair and fibrotic capsule formation [47]. One of the prominent characteristics of myofibroblasts is the high expression level of α-smooth muscle actin (αSMA), which is involved in myofibroblast maturity, focal adhesion and scar tissue contraction [48]. Moreover, the myofibroblast is the mediator of collagen formation, serving as the primary collagen-producing cell of tissue fibrosis [49]. The abovementioned FBR process remodels the ECM network in order to optimize cellular and molecular functions. Over time, this network could progressively thicken the capsular area and induce anoxic conditions in the microenvironment [50]. The fibrotic capsule could enclose the whole implanted object to isolate it from the surrounding tissues. For the

next section, we would highlight more on the interplay between ECM compositions and fibrosis progression.

1.1.2. Extracellular Matrix in Fibrosis

Tissue fibrosis can restore tissue integrity after injury; however, it often fails to regenerate the original functionality of the native tissues. The three-dimensional structure of the ECM of fibrotic tissues consists of an interstitial matrix and basement membrane. The most prominent components of fibrotic ECM are fibrillar collagens, primarily Col I, mainly secreted by fibroblasts and myofibroblasts [51, 52]. These fibrillar collagens originate from procollagen which is released into the ECM by exocytosis after pro-peptide ends removal through procollagen peptidases [51]. This process allows the collagen molecules to generate stiff and aligned fibers in order to support cell residence in the network. Fibrotic capsule formation is always accompanied by ECM remodeling as well as an imbalance of cytokines [53]. After the acute inflammatory process, recruited fibroblasts release molecules including hyaluronan and proteoglycans, both of which play important roles in mediating fibrotic response and have been reported to be potential targets to reverse fibrosis [54, 55]. The differences in ECM components between physiological and fibrotic conditions are illustrated in **Figure 1**. In physiological conditions, ECM remodeling is strictly regulated to maintain homeostasis to ensure no excessive ECM production. In fibrotic tissues, homeostasis is agitated due to cellular and molecular dysregulation, resulting in pathological fibrosis [56]. Myofibroblasts are the major cell type that overproduces fibrillar collagens, particularly Col I and collagen type III (Col III) to form a capsular network [57]. The features of collagens could be changed in the ECM by post-translational protein modification, especially cross-linking and conformation alternations [58]. The distribution of Col III fibers is randomly distributed in the fibrotic tissues and has been shown as unorganized patterns at the early stage of the tissue repair process, which is relevant to the modulation of fibrogenesis [59]. Subsequently, at the late stage, the abundant expression of dense Col I progressively replaces the population of Col III fibers [59]. Despite the fact that myofibroblasts have been considered to play the main role in ECM remodeling in fibrosis, macrophages play the central role of regulating the upstream signals of fibrogenesis [60]. Overall, the ECM network of the fibrotic tissues is not merely a consequence of fibrosis, the ECM has a

functional purpose such as affecting the population of cell types, cellular behavior and signaling based on the above-stated molecules [61].

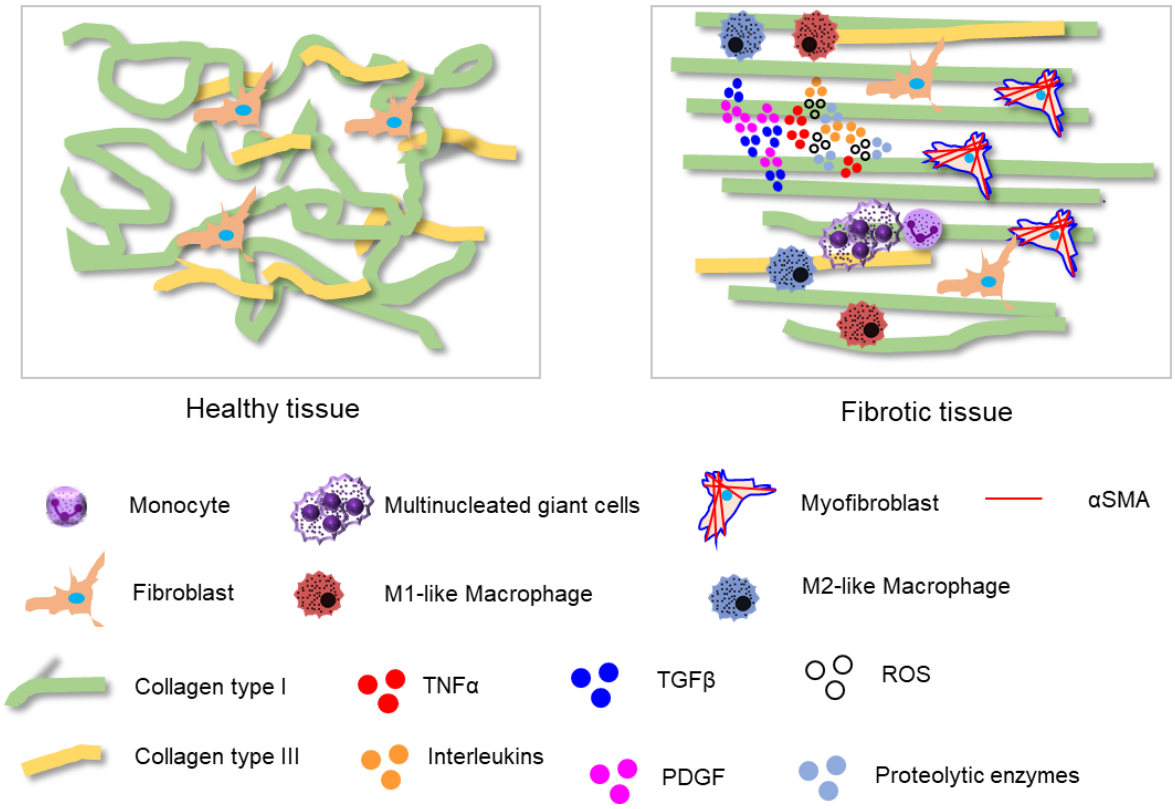

Figure 1. Diagram depicting the cellular and structural alterations that occur in the ECM remodeling during the progression of fibrosis.
In healthy tissues, ECM remodeling remains stably regulated for long-term homeostasis. The fibroblasts show low activity and the ECM protein formation has a steady metabolic turnover. Healthy tissues display loosely arranged collagen networks. In fibrotic tissues, the agitation of homeostasis results in fibrogenesis, inducing the over-proliferation of immune cells and the overproduction of collagens. Fibrotic tissues demonstrate parallelly aligned collagen fibers in the ECM.

1.1.3. Fibrosis in Diabetes

Tissues can be affected by hyperglycemic conditions. Chronic exposure to hyperglycemia can trigger a series of adverse effects on a number of organs [62]. High blood glucose concentration induces multiple fibrogenic pathways and affects immune cell behavior related to ECM remodeling, leading to organ malfunction [63]. There are two perspectives regarding the impact of diabetes on fibrotic tissue formation - cellular responses and molecular mechanisms [64-66]. Hyperglycemia can alter the function of macrophages [67]. As mentioned in previous sections, macrophages play a crucial role as a regulator to recruit and activate fibroblasts and myofibroblasts [68]. In a hyperglycemic environment, it has been reported that the elevated release of

intercellular adhesion molecule-1 and CCL2 results in increased recruitment of macrophages, which can exacerbate the final consequence of fibrosis [69, 70]. Furthermore, in a normal condition, the fibroblast-to-myofibroblast transition has been considered to be the main orchestrator for matrix synthesis and collagens that underwent glycation induce myofibroblast differentiation [52]. However, in a diabetic condition, it is reported that fibroblasts can be activated and that their collagen-deposition capacity is enhanced, which means hyperglycemia can stimulate several cellular responses in fibrotic tissue production [71]. The next aspect that modulates fibrosis in diabetes are cytokine and chemokine secretions. The inflammatory response is activated in a high blood glucose environment by means of stimulation of IL-1β, TNFα, CCL12 and TGFβs, which supports myofibroblast conversion and induces anti-protease enzymes to suppress ECM degradation [72]. Moreover, glucose can react with proteins in chronic hyperglycemic conditions to form advanced glycation end-products (AGEs) without enzymatic glycation [73]. The pathway of glycation on proteins is shown in **Figure 2**. Under hyperglycemic conditions, proteins with a longer half-life in the body undergo glycation reaction non-enzymatically to form early AGE products such as Schiff base and Amadori products [74]. One of the diagnostic indicators of diabetes, HbA1C, is an Amadori rearrangement product generated by the affinity of hemoglobin with glucose [75]. Over longer periods, advanced glycation can cause cross-linkage between protein and protein with several molecules involving n-carboxymethyl lysine, glyoxal-lysine dimer and pentosidine [74]. In the case of diabetic patients, during fibrotic tissue formation, collagens cross-linked with AGEs have secondary structural changes and possess stiffer properties and spontaneously regulate multiple fibrogenic signaling pathways [76]. To date, there are abundant research studies about tissue fibrosis in diabetic patients [74-76]; nevertheless, in the research area of tissue fibrosis induced by FBR, only limited studies were conducted.

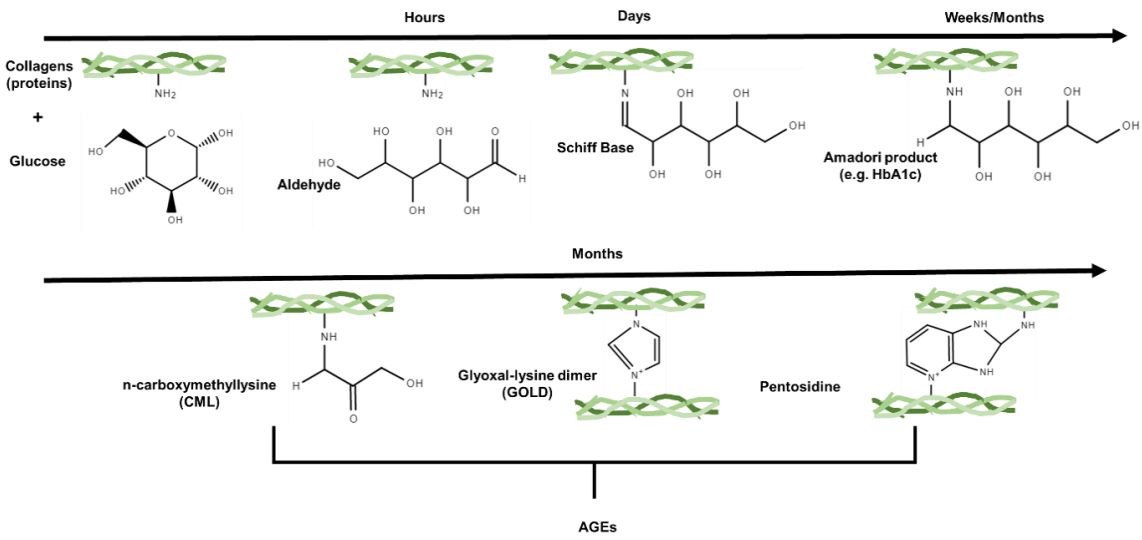

Figure 2. Glycation pathway and the formation of AGEs formation.
AGEs are proteins that undergo glycated reaction after exposure to hyperglycemia, reducing glucose bind to nonspecific proteins to form cross-linking molecules, inducing conformation changes in proteins. The figure was adapted and modified from Mark. E. Cooper et al. [77].

1.2. Raman Microspectroscopy

RMS has been utilized in various fields for decades. The “Raman scattering” or “Raman effect” that underlies this spectroscopic technique is discovered by the Indian physicist Dr. Chandrasekhara Venkata Raman in 1928 and he was also the winner of the Nobel Prize in Physics in the following years [78]. RMS has been utilized in wide-ranging applications. At first, it is used in chemistry to explore the chemical bonding from compounds. Chemical bonds mainly have three styles of motion: vibrational mode, rotational mode and translational mode [79]. RMS mainly detects the signals from vibrational modes, including symmetric and antisymmetric stretching, wagging, twisting, scissoring and rocking [80]. Therefore, every molecule possesses a specific fingerprint that can be identified in its Raman spectrum, for organic molecules, the fingerprint region is normally in the range of wavenumber from 400 -1800 cm^{-1}[79]. RMS is a powerful tool which not only is capable of distinguishing molecules with different molecular formulas but also has the capability to discriminate the small difference between molecules with the same formula including conformational and constitutional isomers as well as stereoisomers (geometric isomers, enantiomers, diastereomers and epimers) [81, 82].

1.2.1. The Theory of Light Scattering

While an incident beam of monochromatic radiation with a specific wavelength hits a surface of a specimen, a minor level (around 1 out of 10^7 photons) of the laser can be scattered in multiple wavelengths, namely “inelastic scattering” or “Raman scattering”; whereas, in most cases, the frequencies of most of the scattered light possesses the same value as the incident light [83, 84]. This scattering is named “Rayleigh scattering” as well as “elastic scattering” [85]. The difference between Raman scattering and Rayleigh scattering is easier to be explained by means of an energy transfer model [86] **(Figure 3)**. When a monochromatic radiation of frequency (ω_i) incident on a totally transparent object, all the photons can be transmitted (ω_t) without frequency change ($\omega_i = \omega_t$). When the incident of the light applies to a molecule, it is excited from an initial energy state of E_l and spontaneously reaches a virtual energy state [87]. Then the molecules relapse to the final energy state which represents E_f. The interplay between the radiation and the chemical bond of the molecule can lead to a frequency change, ω_s represents the frequency of the scattered radiation, which is also called vibrational transition [88]. For Rayleigh scattering, the initial energy state equals the final energy state ($E_i = E_f$) and the radiation frequencies of both incident and scattered light are the same ($\omega_i = \omega_s$). For Raman scattering, particularly the Stokes scattering, the frequency of the emitted radiation is lower than the incident radiation ($\omega_i > \omega_s$, $\omega_{fi} = \omega_i - \omega_s$), which means that the final energy state reaches a higher energy level [$E_f = E_i + h\omega_{fi}$] [89]. When the final stage of the radiation emission reduces to a lower level [$E_f = E_i - h\omega_{fi}$], the frequency becomes higher ($\omega_s > \omega_i$), this light scattering is named anti-Stokes scattering [90]. This theory is the foundation of Raman spectroscopy. The Raman spectrum is generated based on the changes in the above-stated frequencies between the incident and scattered lasers. However, instead of using the unit of ω to describe the transition of frequency, it is generally expressed as wavenumbers (*v),* or inverse-centimeter (cm^{-1}) to interpret the Raman shifts of molecules due to the fact that the value is directly proportional to the energy changes between the vibrational states (ΔE) [91]. When a sample is exposed to the laser from an objective, the scattered lights with various wavenumbers were filtered by the notch filter first to remove the signal from Rayleigh scattering, which has the same or higher wavelength of the incident light [92]. The photons that pass through

the notch filter would be dispersed by the spectrometers grating, which is the main factor that determines the resolution of resulting spectra, and finally detected by a charge-couple device camera to generate the spectrograph [93].

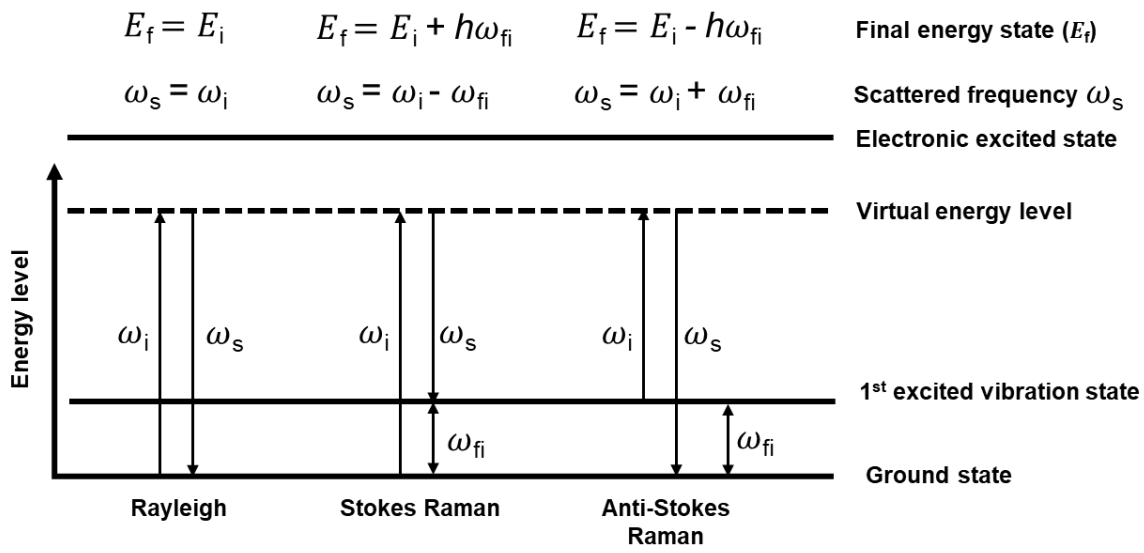

Figure 3. Energy level description of Rayleigh, Stokes and Anti-stokes scattering. Rayleigh scattering, the final energy state is equivalent to the initial stage. Stokes Raman, the final energy state of the scattered light is higher than the initial incident beam. Anti-stokes describes that the energy of scattered light is more intense than the incident beam. The figure was adapted and modified from Katherine J. I. Ember et al. [94].

1.2.2. Methods for the Visualization and Analysis of ECM Components

Histochemical stains have served as a tool for pathologists to perform biological evaluations for centuries. Since the first introduction of hematoxylin and eosin staining on tissue section in 1876 with great contribution to diagnosis and research for histopathological analysis [95], more specific stains such as Masson's trichrome [96], Movat's pentachrome [97] and picrosirius red staining (PSR) [98] appeared to be effective for visualization of biomolecular constituents. Nevertheless, the preparation process from the tissue fixation, biopsy and paraffin embedding to sample slides can be laborious for pathologists. Other limitations of those staining applications have been widely debated, for example, low binding specificity for markers, human or dye artifacts that influence imaging resolution and colorimetry, which can greatly affect the results of quantitative and qualitative analysis [99, 100]. Immunohistochemistry staining for the ECM proteins strengthens the specificity of the proteins by using highly specific marker-binding antibodies with direct or indirect fluorescent labeling [101]. By using

active fluorophore derivatives, target biomolecules can selectively be marked. In order to further improve the imaging quality, advanced optical techniques such as confocal laser scanning microscopy or super-resolution microscopy are utilized as powerful tools for observation [102]. Therefore, compared to conventional staining, it can provide reliable quantitative data for analysis. Nevertheless, the drawbacks include that those successful fluorescence-based methods are costly and sometimes require primary and secondary antibodies to carry out. Moreover, the targeting molecules are limited to proteins and nucleic acids, showing the incapability of fluorescence-based methods to visualize critical ECM components such as polysaccharides, small molecules and minerals [103]. RMS, nevertheless, is a non-invasive vibrational tool to gain detailed information in regard to molecular structures based on the interaction between the laser and chemical bonds [104]. Raman spectra which are representative of several ECM components have been widely reported [105-107], including collagens [108, 109], elastin [108], sulfated glycosaminoglycans [110], glycoproteins such as laminins [111], fibrillin [112], fibronectin [113]. RMS is capable of providing spatial distribution of ECM signals and in combination with multivariate analytical tools such as principal component analysis (PCA). Molecular alterations of specific ECM components can be interpreted based on particular peaks in the fingerprint regions (400-1800 cm^{-1}) of the spectra [80, 114].

Chapter 2

Objectives of the thesis

2. Objectives of the thesis

Tissue fibrosis investigation has always been essential in the field of tissue engineering and regenerative medicine. The conventional histological staining on tissue biopsies is still the gold standard, which is limited to morphological evaluation on collagen bundles. The evaluation depends on individual pathologists' experience and knowledge and can cause bias on various diagnostic outcomes or systematic errors. The aim of the thesis focused on the investigation of fibrosis in a molecular manner, ex vivo, by utilizing RMS. We examined the practicability of RMS to identify different disease states in the fibrotic tissues by identification of the distinct Raman signals based on molecular changes.

Fibrosis progression still mainly relies on quantitative evaluations of the amount of collagen fibers and the morphological changes in certain areas based on histopathological stains. Collagens are the primary ECM proteins found in the connective tissues, which can cause misunderstandings in the assessments. Therefore, one of the main purposes of this thesis is to ascertain the molecular information in pathological collagens within the fibrotic tissues. Raman spectra of Col I from fibrotic and physiological tissues were extracted and underwent MVA to decipher the molecular alternations. The differences can provide distinct recognition of the fibrotic tissues, which can be utilized to target precisely on the regions of interest for further assessments in the future.

In addition to collagen evaluation in tissue fibrosis, monitoring the population of macrophage subtypes has been widely considered a distinctive indicator to evaluate the stage of fibrosis as well as the biocompatibility of implantable biomaterials. Current analytical methods mainly rely on marker labeling. Rat tissues with implantation were used in this thesis. RMS was utilized to provide a proof-of-principle study to distinguish the population of M1-like and M2-like macrophages based on the molecular information in the nuclei spectra. Raman images were further validated quantitatively and qualitatively by conventional histochemical staining and immunofluorescence (IF) staining.

Chapter 3

Results and discussions

3. Results and discussions

3.1. Fibrotic Tissues Characterization

In vivo model has been widely adopted in fibrosis research since it was able to elucidate the complexity of molecular mechanisms and cellular populations for the fibrosis process [115]. Moreover, it is intriguing to evaluate the FBR for future diabetes-reversing implants. Therefore, STZ-induced diabetic female RccHan Wistar rats were utilized as a testing model in this case. Two biomaterials made of polyvinylidene fluoride (PVDF) and TPU (thermoplastic polyurethane)-chronoflex were implanted over 15 days on the back of the rats. The procedures were depicted in **Figure 4**.

Initial assessment of the FBR was conducted by histopathological staining, which has been considered as the gold standard and a fast detection method for tissue fibrosis [116, 117]. Modified Movat's pentachrome staining and PSR demonstrated the overview images of the skin morphology and the ECM structures of implant-free tissues and the fibrotic capsules (Lu et al., **Appendix 1**, Figure 1A). The major difference between pathological regions of fibrotic tissues and interstitial connective tissues can be identified by using the visualization of the dense and longitudinally oriented collagen fibers surrounding the implants. Therefore, the thickness of fibrotic capsules can be determined based on the morphological alterations compared to the interstitial connective regions. The fibrotic tissues induced by the implantable materials were identified straightforwardly, which can be easily guided based on the locations of the implantation. Movat's pentachrome staining was employed to several collagen-rich tissue sections from different fibrotic pathologies in specific organs from human tissues in another study (Becker & Lu et al., **Appendix 2**, Figure 1B). It is reported that histological stains are subject to observer bias and lack the capacity to identify representative pathological regions [118, 119]. Therefore, the recognition of fibrosis was determined by the pathologist, Dr. Montes-Mojarro, based on the distribution of collagens in Masson's trichrome images (Becker & Lu et al., **Appendix 2**, Figure 1A). Collagens are also the primary proteins in healthy mammalian tissues [120]. Hence, the similarity of the collagen distribution can occasionally be shown in the biopsy specimens and errors in the identification of the fibrotic regions can be easily made. Fibrotic tissue detection is highly correlated to the composition of certain types of

collagens, which is also indicative of the severity and different stages of FBR [121, 122]. Therefore, the major limitation of Movat's pentachrome staining is that it cannot be used to identify the collagen subtypes as well as differentiate pathological and healthy collagen fibers.

For the next step, PSR staining was applied to investigate the practicality of whether it can be a robust readout when differentiating between control and fibrotic tissues. In addition to the quantification of the amount of collagen content, PSR was developed to characterize the orientation and architectures of fibrillar collagens. The feature of natural birefringent properties of collagen could be enhanced by picrosirius red and the images can be obtained by using polarized microscopy [123, 124]. Although the definite indication of the colorimetry in PSR imaging remains controversial, the quantification of the ratio between reddish and greenish colors in PSR has been used for examination of the scar collagen states such as fiber thickness or maturation [125-127]. We demonstrated that the PSR is capable of discerning the collagen states between the fibrotic capsule and the interstitial connective tissues. The ratio of red/orange to yellow/green fibers showed significant differences between these tissue types and the red/orange fibers expressed more in the capsular areas (Lu et al., **Appendix 1**, Figure 1DE). Nevertheless, when we applied the PSR on human fibrotic tissues, although this method was sufficient to differentiate tissues between control and fibrosis in some cases, the alterations in the ratio of reddish and greenish fibers exhibited inconsistency throughout the fibrotic tissues and indicated no fibrosis-specific tendency throughout the fibrotic and control tissues. (Becker & Lu et al., **Appendix 2**, Figure 2B). Therefore, we further measured the difference in collagen orientation between the two groups. It has been informed that the pattern of collagen bundles can show a different distribution of fiber alignments in scar tissues [128, 129]. We found that the alignment of collagen fibers that were assessed by fiber orientation histograms indicated the tendency of collagen alignments in fibrotic tissues featured non-aligned collagen distribution; whereas, even distribution on various angles was shown in collagen network in control groups (Becker & Lu et al., **Appendix 2**, Figure 2CD). In order to calculate the statistical significance of the correlation between the orientation pattern and the fibrotic tissues, the quantification of the fiber alignment was conducted through coherency analysis (Becker & Lu et al., **Appendix 2**, Figure 2E). Nonetheless, the readout of coherency analysis of fiber alignment showed no

significant differences between control and fibrotic tissues, indicating PSR with polarized microscopy is insufficient in robustness for qualitative and quantitative analysis in fibrotic tissue characterization. Therefore, in this thesis, Raman imaging was employed to characterize the molecular and structural alterations in the fibrotic tissues.

Previous work by our group has demonstrated the great potential of RMS to investigate ECM architectures and biomolecules in tissue engineering in a marker-independent manner [109, 130, 131]. Raman imaging was acquired based on the true component analysis (TCA), which is a statistical method that contains the utilization of a linear combination of Raman spectra to interpret each pixel in a Raman scan. Fibrotic tissues were illustrated as color-coded intensity distribution heatmaps based on the most relevant spectra, which enabled the identification of the ECM components (Lu et al., **Appendix 1**, Figure 2AC and Beatty & Lu et al., **Appendix 3**, Figure 6). The composition of the ECM network can be recognized in one single scan, which was further validated by IF images with separated staining. Col, Col III and αSMA are widely utilized as fibrotic markers which are highly correlated to fibrotic tissue formation in several studies [132-134]. Similar trends of the distribution pattern of those signals were observed in both IF and Raman imaging, indicating Raman imaging can be used to localize fibrotic regions for future clinical uses (Lu et al., **Appendix 1**, Figure 2CD).

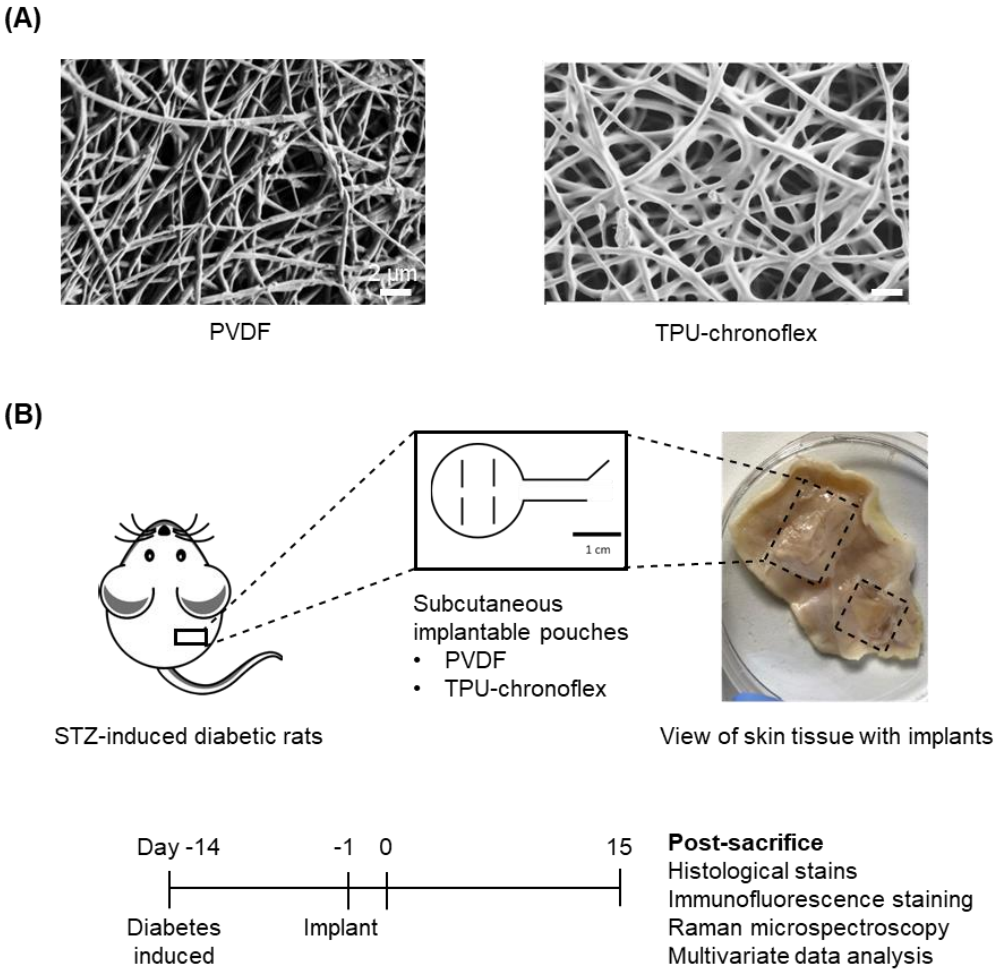

Figure 4. Implantable pouches and schematic of study design.
(A) Fabricated sheets, PVDF and TPU-chronoflex with 50 µm thickness and 2 µm pore size, generated by electrospinning method. (B) Diabetes was induced by utilizing STZ 14 days before implantation. PVDF and TPU-chronoflex pouches were implanted subcutaneously at the back of the diabetic rats over 15 days. The FBR was evaluated by histopathological staining, IF staining, RMS and multivariate data analysis. The figure was adapted from Lu et al., **Appendix 1**.

3.1.1. The Influence of Diabetes on ECM Composition in Rodent Model

Diabetes treatments have been tremendously enhanced in the last decade. Several diabetes-reversing implants such as closed-loop insulin delivery systems and cell-loaded encapsulation devices have been designed to alleviate the burden faced by diabetic patients [135, 136]. Nevertheless, the FBR caused by implantable devices still remains a problem in this field [137, 138]. The FBR is an altered wound-healing process; nevertheless, most studies concentrated on the wound-healing process of diabetic patients [139, 140], which cannot equally contribute to the understanding of FBR provoked by implants in the diabetic population. We published a study regarding in-depth investigation toward this concern [109]. We implanted TPU-based medical

devices on healthy and STZ-induced diabetic rats over 14 days and explored alterations in the FBR (Beatty & Lu et al., **Appendix 3**, Figure 1). We did not observe any difference in ECM expression levels of Col, Col III and αSMA in the fibrotic capsules between healthy and diabetic groups (Beatty & Lu et al., **Appendix 3**, Figure 5 and 6). Strong scientific evidence has supported that poor healing is one of the main features of diabetic wounds and is highly related to insufficient ECM formation and downregulation of myofibroblast activity [141, 142]. Nevertheless, in our results, the ECM proteins production and the expression level of αSMA of fibrotic tissues in the diabetic groups did not show similar results compared to general diabetic studies for poor wound healing (Beatty & Lu et al., **Appendix 3**, Figure 5 and 6). In fact, quantitative evaluation of the biomarkers occasionally might be insufficient to fully describe complex biological networks [143]. Therefore, an in-depth analysis of Col I alternations was conducted on extracted Raman spectra from the capsular areas. Molecular information was obtained via PCA by analyzing Col I spectra (Beatty & Lu et al., **Appendix 3**, Figure 7A). Two separated clusters between diabetic and healthy groups on the scatter plot were confirmed by the mean value of the PC-3 score (Beatty & Lu et al., **Appendix 3**, Figure 7B). The difference is potentially contributed to secondary structural differences in Col I based on the loading of PC-3, indicating the presence of AGE products (Beatty & Lu et al., **Appendix 3**, Figure 7CD). Fibrillar collagens, considered as a series of long half-life proteins, can potentially undergo non-enzymatic glycation under high blood glucose levels to form AGE products, causing irreversible cross-linkage between the fibers which alter the conformational structures [144, 145]. Moreover, the high expression level of free AGEs can bind to the receptors of AGEs, which play a vital role in cellular activity regulation. Peak shifts at 1430, 1277, 1047, 1038, 914, 867 and 814 cm^{-1} are relevant to AGE products (n-carbamylglutamate, glyoxal-lysine dimer, pentosidine or glucosepane) [146-148]. Nevertheless, the Raman signals that correspond to which subtypes of AGE products still require more studies for further validation. The spectra data which is representative of cross-linked AGEs can potentially be a substituted biomarker of glycosylated hemoglobin that has been widely used to monitor long-term glycemic control in diabetes. The diagnostic process potentially can only require low-intensity laser examination at a superficial layer of skin tissues in combination with machine learning without invasive procedures and time-consuming testing assay **(Figure 5)**.

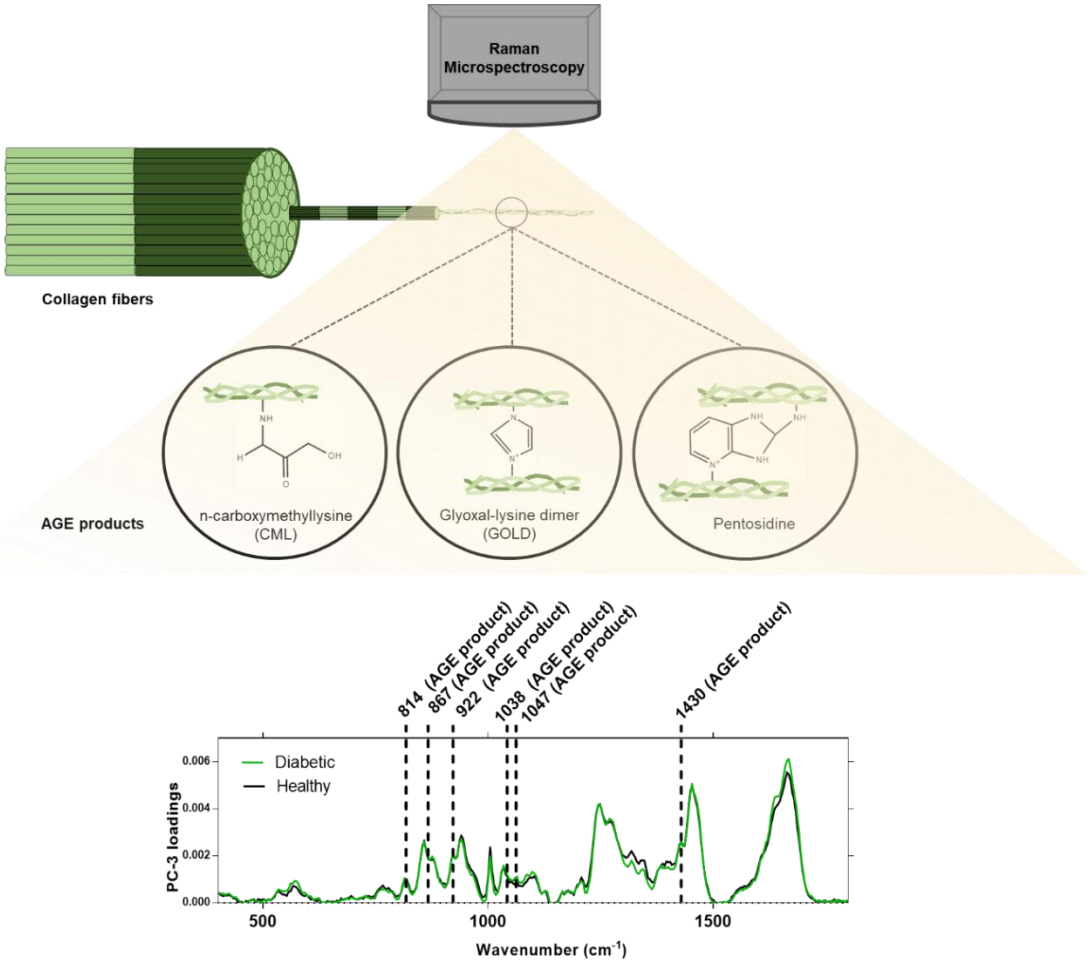

Figure 5. RMS identifies AGEs on collagen fibers in diabetic rodent model.
The presence of AGEs gives rise to irreversible cross-linkage between fibrillar collagen under hyperglycemic environment. RMS can identify the conformational structure of Col I, involving the crosslinking AGEs that bond to the fibers. The figure was adapted from Beatty & Lu et al. [109].

3.2. Raman Spectrum of Collagen I Discriminates Fibrotic Tissues Induced by PVDF and TPU-chronoflex

Challenges have existed in fibrotic disorder diagnosis for decades. Current available clinical modalities for tissue fibrosis often were used to evaluate late-stage fibrotic disorders with established collagen deposition [149]. Determination of stages of fibrotic diseases still requires a biopsy which is risky and can cause burdensome to the patients and the assessments highly rely on histological analysis [150]. Until now, some antifibrotic agents are available to decelerate fibrosis progression, meaning that molecule-sensitive methods are urgently required to monitor the interventions [151].

Therefore, to overcome the limitations of the conventional diagnostic tool, RMS was applied as a molecular-tracking technique to decipher the alterations in the Col I structure based on spectral data. Single Col I spectra were selected from different types of tissues, which were mainly from interstitial connective tissues and fibrotic capsules (Lu et al., **Appendix 1**, Figure 3A). PCA analysis was applied to the Col I spectra in order to discriminate the subtle differences between the two types of tissues (Lu et al., **Appendix 1**, Figure 3B). The scores plot of PC-1/PC-3 demonstrated two separated clusters that contributed to the changes in Col I signatures. The result was further confirmed by the mean value of PC-3 scores, showing a significant difference between Col I spectra extracted from interstitial connective tissues and fibrotic capsules (Lu et al., **Appendix 1**, Figure 3CD).

The biological assignments were contributed by PC-3 loading. The peaks were assigned to amide I, tyrosine, amide III, phenylalanine, proline and hydroxyproline. These alterations are highly relevant to conformational differences in Col I fibers, which might have an influence on the stability of the collagen triple helix. During the process of tissue remodeling, collagen production highly depends on proline and hydroxyproline [152, 153]. The importance of hydroxyproline to collagen content has been shown to be a potential molecular target for evaluation in fibrotic disorders [154, 155]. In addition, the fibrillar collagens are originally from procollagen mainly consisting of repeating tripeptides (glycine-proline-hydroxyproline) [156, 157]. Proline can undergo hydroxylation to generate and infiltrate the endoplasmic reticulum for post-translational modification [158]. The modified polypeptides are then secreted by exocytosis to the extracellular location followed by ends cleavage via procollagen peptidases [159]. The spectra peak at 815 cm^{-1} and 856 cm^{-1} (proline and hydroxyproline) showed decreased amplitude levels in the fibrotic capsules compared to interstitial connective tissues, which can be explained by the mechanism of the collagen formation process. Recent research evaluated wound healing activity by administration of proline and hydroxyproline by using a rodent model [160]. The results exhibited proline and hydroxyproline can activate muscle regeneration with relatively low fibrotic tissue expression. A more recent study utilized a murine model to evaluate wound healing activity by administration of proline and hydroxyproline [160]. The results showed that proline and hydroxyproline might induce muscle regeneration with less fibrotic tissue. It has been also reported that sufficient hydroxylation of proline

resides at collagen is vital for the physical stability of the triple helical structure [161]. Studies using recombinant Col I showed that non-hydroxylated triple helix is not able to achieve self-assembling into supramolecular fibril under physiological conditions [162, 163].

Overall, these results indicated that RMS along with MVA algorithms has great promise to identify fibrotic alterations that can be applied to future clinical practice **(Figure 6)**. RMS, as a hyperspectral imaging technique, can combine with a deep-learning framework to decipher pathological features of fibrosis on a spectral and spatial level. This thesis provided a proof-of-principle insight into ex vivo tissue specimens to discriminate the fibrotic capsule and physiological tissues based on in-depth analysis of high information-content spectra data. Nevertheless, several limitations at the present include: 1) Insufficient Col I spectra data in the database since even in the same fibrotic disorder, significant molecular heterogeneity was found in different species and individuals [164]. 2) Temporal problems, such as long acquisition time to acquire high-resolution spectra data as well as laborious post-processing noise removal procedures and MVA/TCA analysis on large datasets, hinder the application to achieve real-time imaging for clinical use with high quality. Hopefully, analysis of hyperspectral datasets has been reported to be operated by using artificial intelligence techniques [165, 166], which might give rise to the development of high throughput molecular imaging tools for fibrosis diagnosis in the future.

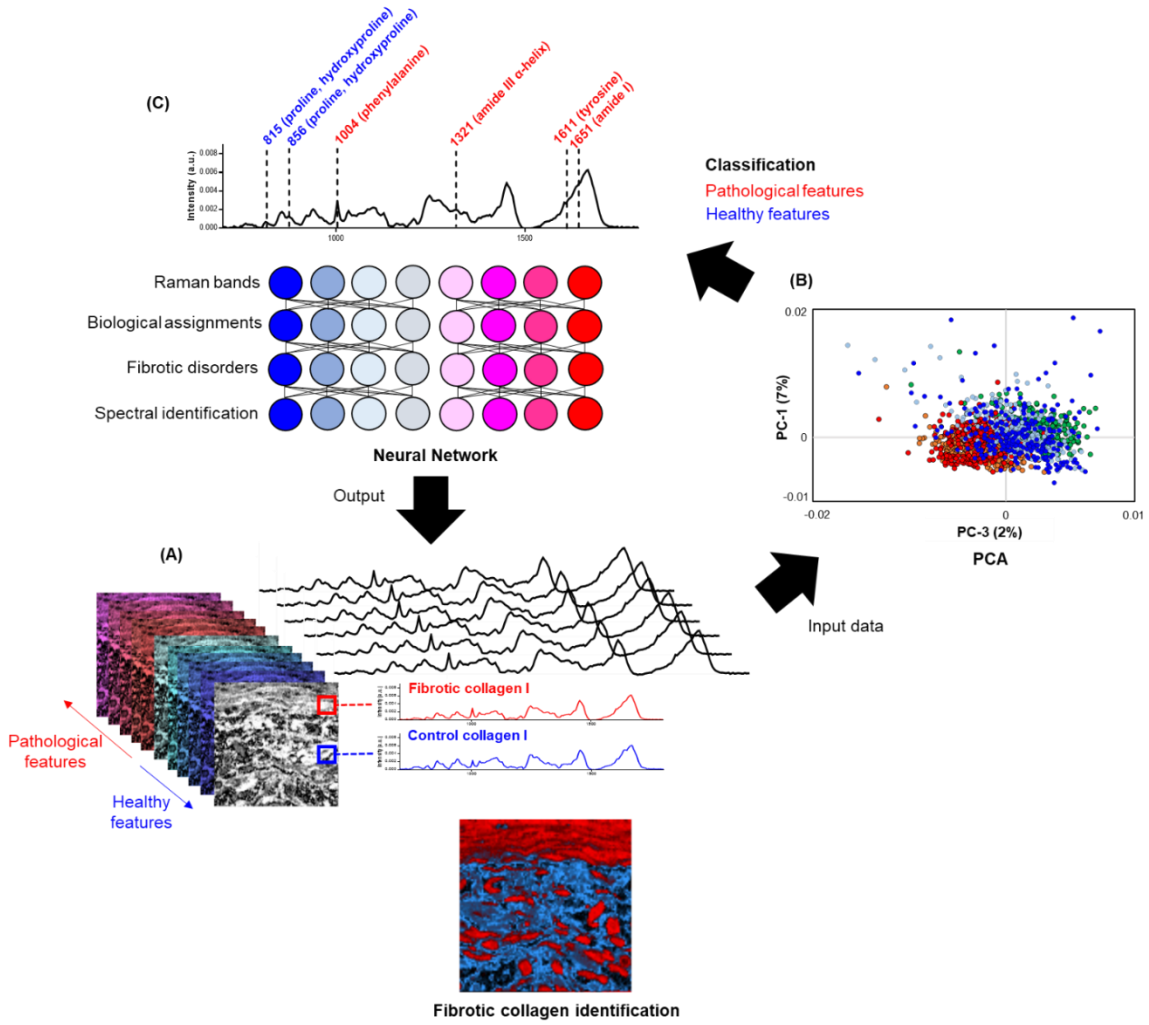

Figure 6. Potential automatic discrimination of fibrotic regions in fibrotic disorders. A flow chart of identification of fibrotic pathologies by using RMS in combination with deep learning. (A) Raman spectra of Col I were collected from the scanning areas and underwent pre-processing as input data. (B) PCA analysis classifies the potential spectra that might be indicated as pathological Col I and deciphers the elements in the Col I spectra. (C) An architectural basis of convolutional neural network: the characteristics of Col I spectra can be trained and underwent in-depth analysis. The relationships in the network are developed and a meta-database can be built as a training system. Raman bands can be assigned to specific biological features such as secondary structures, amino acids or peptides which are correlated with fibrotic disorders. The output data can be applied back to the input data from the (A) step or random Col I spectra from new patients. Finally, fibrotic tissue identification can also be generated as images for diagnostic use. The figures were adapted from Lu et al., **Appendix 1**.

3.3. RMS Identifies Fibrotic Tissues Induced by Subcutaneous Implantation via Deconvoluted Col I Spectra

To further validate the conformation changes of Col I in the fibrotic region, Raman spectral data underwent deconvolution on the amide I band region. Gold standard methods to determine the protein secondary structures are X-ray crystallography,

multidimensional nuclear magnetic resonance (NMR) spectroscopy and circular dichroism spectroscopy [167, 168]. The use of X-ray crystallography requires protein specimens to undergo crystallization before measurement [169]. The X-ray beam incidents to the protein crystal, which can induce diffraction patterns that can be recorded by the crystallographer [170]. Every diffraction pattern corresponds to particular secondary structures such as α-helix, β-strands, β-turns and random coils [171]. However, most of the proteins can only remain their biological function in the solvent or under a hydrophilic condition [172]. Although NMR spectroscopy was developed to overcome this limitation which allows measuring the protein structure in solution, it is not suitable for large macromolecules and only confined to small ones (below 25 KDa) [173]. Circular dichroism spectroscopy can also be utilized for secondary structure determination in solution as well as suitable for proteins with large molecule weight [174]. However, the main problem is that the samples require dilution to optically transparent solution while examination, which means any object that causes light scattering can have an impact on the measurement [167]. Furthermore, the structural motif of β-turn is challenging to be detected by this spectroscopic method [175]. Therefore, we published a research to discriminate structural changes in Col I by using RMS [176]. In this thesis, similar methods were applied to the capsular areas surrounding the implants.

Raman spectroscopy has been considered as a promising way to decipher the protein secondary structure by means of the amide I band deconvolution (1550-1720 cm^{-1}) [176, 177]. The theory behind the determination method is based on the different patterns of hydrogen-bonding of the amide region (C=O and N-H groups) [178]. Each secondary structure, α-helix, β-sheets, β-turns and random coils, has its particular type of hydrogen-bonding pattern which arises from their conformation arrangements, inducing different patterns of Raman scattering signals [179]. Various Col I spectra from different types of tissues were extracted. Prior to deconvolution at the amide I region, a fitting procedure with the Lorentz algorithm on this region was applied followed by iterations of 1000 when fitting five functions of the sub-peaks. Each sub-peak with a certain range of wavenumbers represents a particular secondary structure: the peak position at 1685 cm^{-1} (β-turn, β-sheet or random coils), 1670 cm^{-1} (β-turn), 1657 cm^{-1} (α-helix) [180-182]. Herein, we highlighted that the topography of the spectral peak of amide I signal is regulated by the peak of 1605 cm^{-1}. The topography

of the amide I peak demonstrated a distinctive indicator for fibrotic tissue identification, showing similar topography in connective tissues but different from the shape of amide I band of fibrotic capsules **(Figure 7 B-F)**.

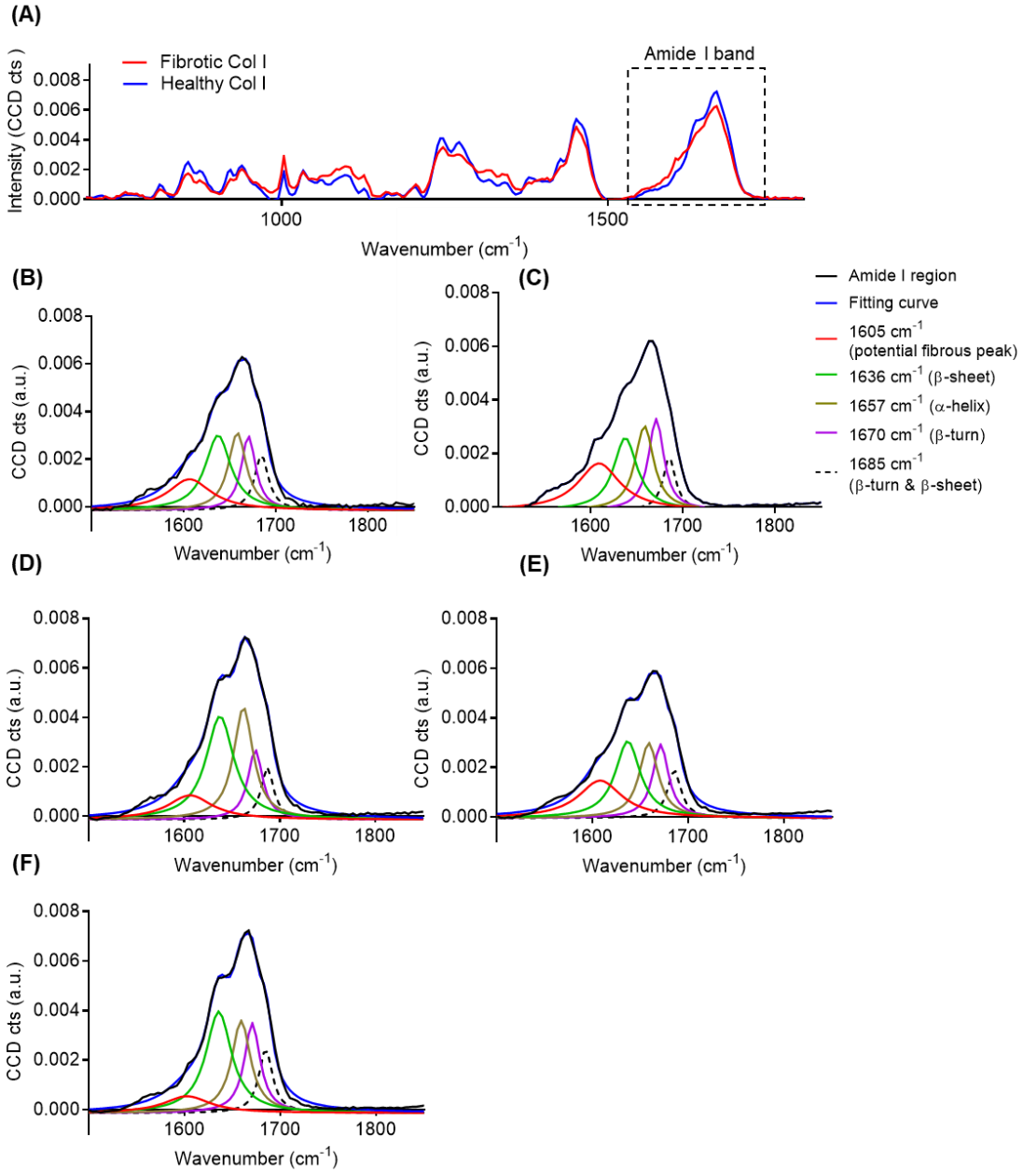

Figure 7.Spectral deconvolution of amide I band from Col I spectra from various tissue types. (A) Fingerprints of fibrotic and healthy Col I spectra. Amide I spectra deconvolution of (B) fibrotic capsule caused by PVDF (C) fibrotic capsule caused by TPU-chronoflex (D) Connective tissue from PVDF samples. (E) connective tissue from TPU-chronoflex samples. (F) Connective tissue from implant-free skin tissues. The original amide I region is demonstrated by a black line and the fitted amide I band is shown in a blue solid line. Sub-peaks were shown at 1605, 1636, 1657, 1670 and 1685 cm^{-1}, representing the secondary structure of Col I.

Furthermore, the quantitative peak intensities at 1605 cm^{-1} that originated from connective tissues and fibrotic tissues correlated to their tissue types **(Figure 8)**. The elevated peak intensity at 1605 cm^{-1} of the fibrotic Col I fiber can be biologically assigned to the amino acids of tyrosine and phenylalanine [183, 184]. Recently, a group proposed that the difference of this amino acid at the triple helix location of Col I might be a key factor that mediates the binding affinity of heat shock protein 47 (HSP47) [185]. HSP47 is gradually considered to be a particular chaperon to procollagen, which can play a vital role in the folding of Col I that occurs in fibrotic disorders [186]. Therefore, HSP47 received increasing attention as a novel therapeutic target for drug development that could be used to ameliorate or reverse tissue fibrosis [187, 188]. Collagens consist of a repetitious sequence of Glycine-Xaa-Yaa, where Xaa and Yaa are commonly proline and hydroxyproline, which are the targets of HSP47 binding [189]. The roles of these two amino acids regarding the homeostasis of collagen formation have been discussed in the previous section. Nonetheless, the sequence of Xaa and Yaa occasionally is replaced by leucine, arginine and tyrosine, which gives rise to different dissociation constants for the binding affinity between procollagen and HSP47 [157]. It has been reported a significant decline of the dissociation constant of the binding of HSP47 when Xaa or Yaa was occupied by phenylalanine, tyrosine and leucine, indicating higher binding affinity between procollagen and HSP47 [157]. Upregulation of the binding affinity of HSP47 can contribute to the overproduction of collagen, resulting in tissue fibrosis [186, 190]. This might explain the increased amplitude of the pathological fibrillar collagen at the Raman peak of 1605 cm^{-1}, which might show higher amounts of amino acids with aromatic rings such as tyrosine and phenylalanine [184, 191]. It was hypothesized that the procollagens with the higher expression level of aromatic amino acids bind with HSP47 better compared to those with common amino acids of Xaa and Yaa (proline and hydroxyproline). However, the sequence of fibrotic Col I required further examination, potentially via X-ray crystallography, multidimensional NMR spectroscopy and circular dichroism spectroscopy to offer more evidence for the results. Future application is to perform more fibrotic disorders and collect more spectra data of Col I from patients. The workflow is identical to **Figure 6**. The deconvoluted Raman peak at amide I band of Col can provide more nodes to the neural network, which potentially can benefit deep learning for further diagnosis with more information.

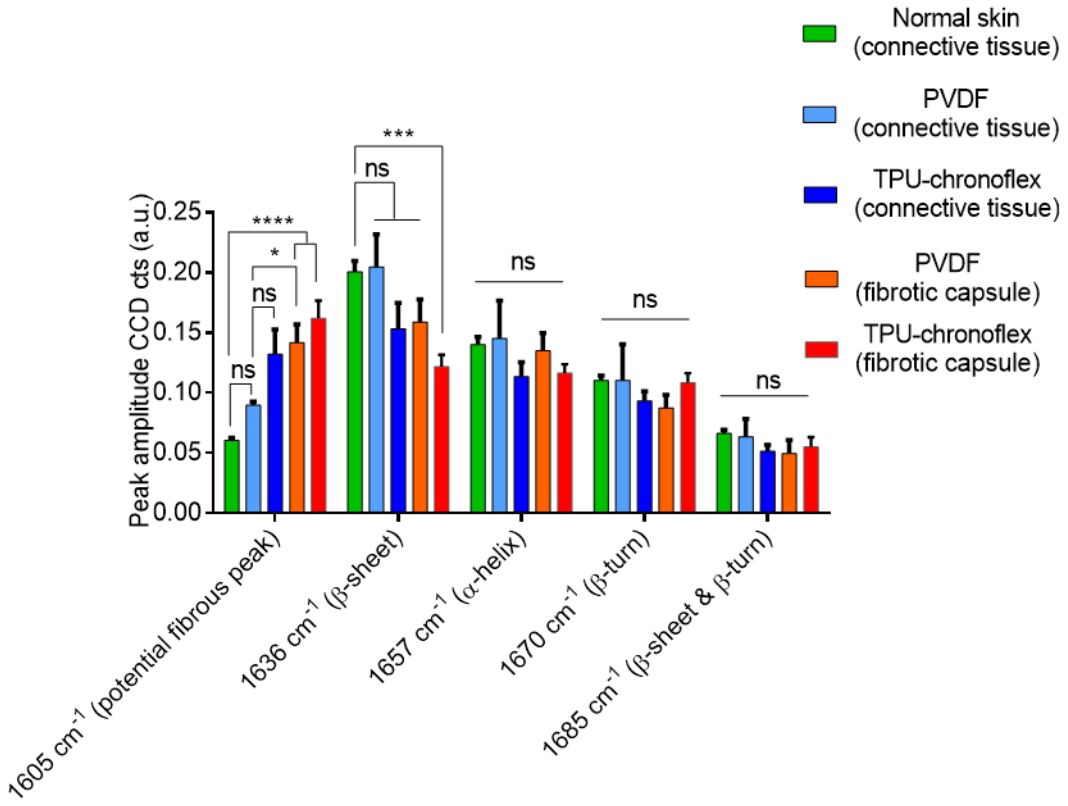

Figure 8. Qualitative evaluation of representative peaks of secondary structures of proteins under amide I band.
The spectral peak at 1605 cm-1 showed a high correlation with the fibrotic tissues. Statistical analysis: One-way ANOVA, p*< 0.05, p***< 0.001 and p****< 0.0001.

3.4. Macrophage Phenotype Classification

3.4.1. In Situ Immunophenotyping by RMS

The transition stage of the FBR from acute inflammation to chronic fibrotic tissue formation highly relates to macrophage polarization from M1-like macrophages to M2-like phenotype [192]. Macrophage polarization is one of the key factors that determine the biocompatibility of a medical device [193, 194]. Therefore, evaluation of the M1-like/M2-like population is essential to test a variety of implantable biomaterials. The current classification approach of tissue-resident macrophages mainly relies on immunohistochemistry [195, 196]. Recently, our group published a proof-of-concept study using RMS on an in vitro polarization model to discern different phenotypes of monocyte-derived macrophages [196]. Fluorescence-activated cell sorting method was utilized for the purpose of sorting the populations of M1 and M2 subtypes.

However, in comparison to single-cell assessment in suspension, recognition of cells in the tissue environment remains challenging.

This thesis proposed a potential way to investigate the possibility of in situ immunophenotyping at the fibrotic regions. Prior to Raman imaging, IF staining was first applied to label either pan-macrophage with CD68, M1-like macrophage with CCR7 or M2-like macrophage with CD204 (Lu et al., **Appendix 1**, Figure 4A). Reference Raman spectra from nuclei were extracted from the fibrotic tissues based on these positive protein signals (Lu et al., **Appendix 1**, Figure 4B). The nuclei spectra from $CCR7^-/CD204^-$ cells were also extracted by means of TCA. Identical Raman peaks with a subtle difference at 1579 cm^{-1}, 1488 cm^{-1}, 1379 cm^{-1}, 1330 cm^{-1}, 879 cm^{-1}, 857 cm^{-1}, 786 cm^{-1} and 725 cm^{-1} could be identified among the nuclei regions, indicating DNA signatures within the three spectra. The extracted spectra were re-applied as reference spectra to the fibrotic regions within unstained tissues with PVDF and TPU-chronoflex implantation. By using TCA, the subtypes of macrophages were identified and localized to generate color-coded heat maps, which were comparable to IF images (Lu et al., **Appendix 1**, Figure 4C). The ratio of the numbers of M1-like ($CCR7^+$) and M2-like macrophages ($CD204^+$) was determined. M1-like/M2-like ratio has been widely shown to indicate the degree of inflammatory and fibrotic reaction against implants [197, 198].

The M1-like/M2-like ratio in the capsular area around TPU-chronoflex showed a 4-fold significant increase compared to PVDF (Lu et al., **Appendix 1**, Figure 4DE), highly correlating with the high expression level of Col I and thicker fibrotic capsule that were observed at previous ECM characterization via histopathological staining **(Figure 9)**. Several studies have shown that the prolonged presence of M1-like macrophages can result in severe FBR and fibrotic encapsulation by deteriorating the inflammatory activities, which can induce failure for implant integration [199, 200]. On the contrary, M2-like macrophages consistently secrete anti-inflammatory cytokines and can also maintain immune regulatory function to attenuate fibrotic capsule formation [199, 200]. Our findings suggested that TPU-chronoflex provoked more severe FBR compared to PVDF and indicated that RMS enabled the evaluation based on cellular and molecular levels to evaluate the FBR induced by the implants.

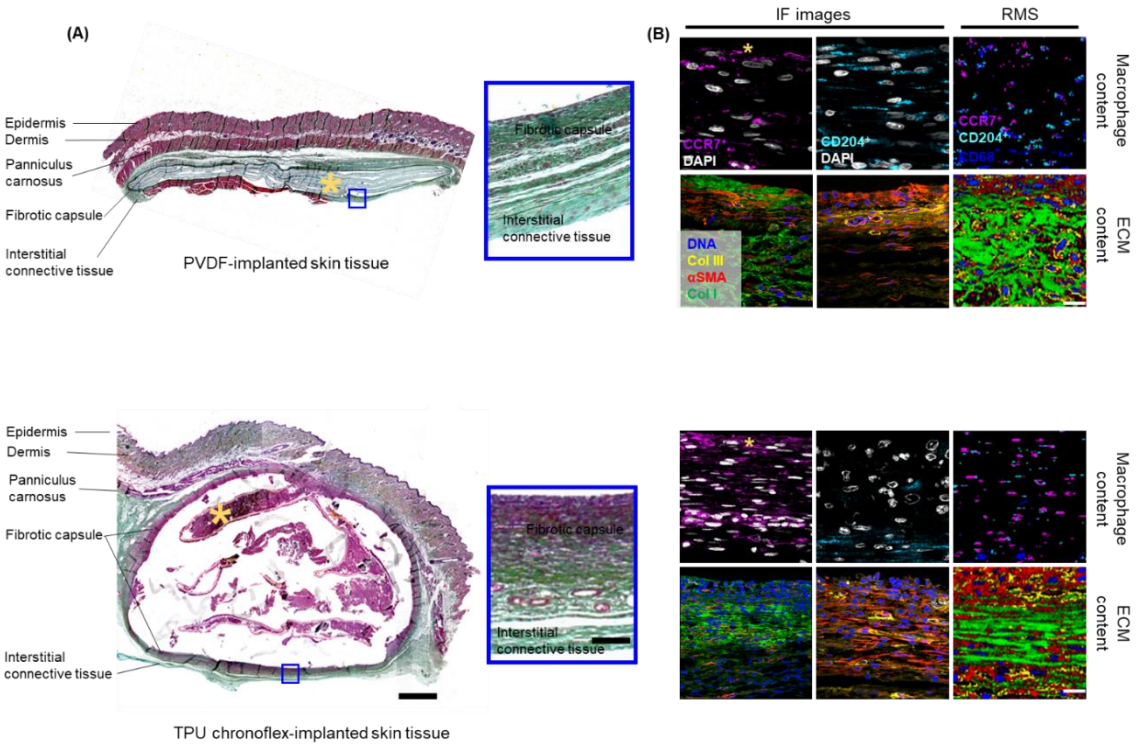

Figure 9. Investigation of fibrotic capsules induced by implantation by using marker–independent and marker–independent.
(A) Images of Movat's pentachrome staining illustrated the fibrotic capsules induced by PVDF and TPU-chronoflex. The regions of interest indicated morphological differences and in-depth analysis was required to decipher the components in the tissues. Scale bars: 1000 µm (left), 50 µm (right) (B) RMS enabled the identification of ECM components as well as immunophenotyping to evaluate the degree of FBR. Scale bars: 20 µm; Yellow asterisk: implant side. Illustration adapted from Lu et al., **Appendix 1**.

3.4.2. Identification of Epigenetic Alterations in M1-like/M2-like Macrophages via PCA Analysis Based on the Nuclei Spectra

Nuclei spectra data from M1-like and M2-like macrophages further underwent PCA analysis (Lu et al., **Appendix 1**, Figure 5). The biological assignments are investigated based on the identified Raman shifts in nuclei signatures. The alterations of the molecular information in nuclei between M1-like and M2-like macrophages can be deciphered in the PC-1 loading plot. The cluster of nuclei spectra from M1-like macrophages was distributed at a negative PC-1 score range, while M2-like nuclei-derived spectra data displayed positive score values (Lu et al., **Appendix 1**, Figure 5AB). Qualitative evaluations of the identified signatures demonstrated significantly increased signals from the M1-like nuclei at the peaks of 1579 cm^{-1}, 1488 cm^{-1}, 1342 cm^{-1}, 1330 cm^{-1}, 786 cm^{-1} and 725 cm^{-1}, these features are assigned to the pyrimidine

ring, guanine, phospholipid, 5-Methylcytosine and adenine (Lu et al., **Appendix 1**, supplementary Table S1). The nuclei spectra of M2-like macrophages conversely contained elevated peak intensities at 879 cm^{-1} and 857 cm^{-1}, which are assigned to hydroxyproline, proline, tryptophan and tyrosine (Lu et al., **Appendix 1**, Figure 5D).

These Raman band alterations were contributed to the epigenetic modifications, which might play a role in monocyte differentiation into macrophage as well as M1-like macrophage polarization into M2-like phenotype. Recent studies have shown that M1-like macrophages have a relatively higher degree of DNA methylation state [201], which is able to explain nuclei signatures in the M1-like phenotype. It has been reported that M2-like macrophage has a lower expression level of DNA methyltransferase 1, inducing downregulation of DNA methylation level [202]. Furthermore, the increased peak intensity which corresponds to proline was found in the nuclei of M2-like macrophages. As an epigenetic modifier, proline is the precursor of α-ketoglutarate, which is well known for the vital factors in cellular metabolism, especially in the Krebs cycle [203]. α-ketoglutarate can enter the nucleus and become substrates of ten-eleven translocation proteins and Jumonji C domain demethylases [204, 205]. These two enzymes play a crucial role in DNA and histone demethylation, which are the key components to activate macrophages polarizing into M2-like phenotypes to initiate the anti-inflammatory reaction [206]. Based on the results, we showed that RMS in combination with MVA potentially cannot only be utilized to conduct immunophenotyping but also can be used for biological interpretation of cellular activities as well as epigenetic modifications.

Chapter 4

Conclusions

4. Conclusions

The current fibrotic tissues assessment is limited to the conventional gold-standard histopathological analysis as well as IF staining for ECM characterization [99, 100, 207]. Several pioneering imaging techniques, involving magnetic resonance imaging (MRI), computed tomography (CT), second harmonic generation (SHG) and ultrasound elastography provide optical examinations on architectural characteristics of fibrosis [208, 209]; nonetheless, the investigation is still confined to morphological differences, geometrical and quantitative evaluation of collagen fibers, which only allows for late-stage fibrotic tissues diagnosis or during progressive dysfunction of organs. These advanced techniques are inadequate to monitor the progression of fibrotic tissue formation in a molecular manner [19]. These limitations hinder patients who suffer from fibrotic disorders from obtaining appropriate treatment at an early phase to mitigate the fibrosis.

In this thesis, the investigation of fibrotic tissues induced by the FBR was established by using non-destructive and marker-independent RMS. In combination with MVA, molecular information of Col I can be identified based on the spectral fingerprints caused by the vibrational and rotational modes of the molecules [210]. First of all, RMS was employed to compare the fibrotic capsule induced by implantation in diabetic and nondiabetic rodent models. The secondary structural difference in Col I can be discriminated between two groups even though the ECM composition of the fibrotic capsule did not show any difference. Furthermore, the PC-3 loadings plot depicted the presence of AGEs can give rise to irreversible cross-linkage between Col I fibers in a hyperglycemic environment. We proposed that the non-invasive detection of cross-linked AGEs via RMS can be an alternative indicator to track long-term blood glucose control for diabetic patients.

Secondly, RMS was utilized as a state-of-art diagnostic technique for high-speed and robust discrimination between connective and fibrotic tissues. PCA analysis demonstrated the different biomolecular signatures of the extracted Col I spectra from two types of tissues, indicating conformational differences in Col I. The biological assignments contributed to PC loading showed proline, hydroxyproline and amide I alterations in the triple helical structure which might be related to fibrotic disorders

[211]. Further validation of the secondary structure of Col I was conducted by amide I band deconvolution. Secondary structures of α-helix, β-sheets, β-turns and random coils have been reported to be highly relevant to the sub-peaks below the amide I band [180]. Compared to connective tissues, a significantly larger peak intensity at the position of 1605 cm^{-1} was found to be statistically correlative with fibrotic capsules. This molecular-sensitive method allows fibrosis detection beyond morphological and quantitative changes of the collagen bundles, which can be a promising diagnostic tool for future clinical application.

The current identification of tissue-resident immune cells typically depends on RNA expression, immunohistochemistry and flow cytometry [195, 196]. Macrophages played a crucial role in innate and adaptive immune systems, which has been extensively regarded as a factor to determine the biocompatibility of biomaterials [212]. Therefore, this thesis suggested a novel way to classify M1-like/M2-like macrophages by utilizing RMS in a marker-independent manner ex vivo. The reference nuclei spectra were extracted based on the co-localization of fluorescence-positive signals of M1-like and M2-like macrophages. These reference spectra were employed to unstained skin tissue sections with PVDF and TPU-chronoflex implantation. Heat maps with color codes were generated and demonstrated a high correlation with IF images. This is a pioneering analytical method establishment for in situ immunophenotyping surrounding implanted biomaterials, indicating a potential approach for future utilization of non-destructive and label-free examination.

The major limitation of our study was the use of the rodent model to investigate the tissue fibrosis induced by the implantation of biomaterials. It has been reported differences in FBR between human and animal models [213], which remains controversial to translate the positive preclinical results to humans. From the subcutaneous anatomy perspective, rodents have the structure of panniculus carnosus, which belongs to the striated muscle layer between the dermis and interstitial connective tissue [214]. It can cause contraction on the murine skin which can substantially affect the circumstance of subcutaneous implantation [215]. This anatomical structure is vestigial in human, only exists in regions of dartos muscle of scrotum, palmaris brevis which lies in the fascia and platysma muscle at the neck [216-218]. Therefore, the anatomical difference of subcutaneous location can affect the

histological interpretation as well as imaging analysis and is challenging to reflect it to humans. The other main difference of the skin tissue between murine and human can be attributed to biomechanical issues [219]. Large animals such as humans and pigs possess tight and thick skin (around 100 μm), where the epidermis contains five to ten cell layers [219, 220]. However, murine skin is relatively loose and thinner, the epidermis consists of two to three cell layers [219]. This means the change of compressive force on the implantable devices is not translational to human clinical trials. The other reason that might cause the FBR difference is immunological components [219]. The population of neutrophils and lymphocytes in peripheral blood is not identical between human and murine. Human has approximately 60 ± 10% of neutrophils and 40 ± 10% of lymphocytes; whereas, murine has 17.5 ± 7.5% and 82.5 ± 7.5%, respectively [221]. Although both murine and human have $CD8^+$ T cells, murine possesses a special kind of T cell, named as γd dendritic epidermal T cells [222-225]. γd dendritic epidermal T cells can produce FGF-9 to the injured site after implantation and activate the WNT signaling pathway which is highly related to hair follicle repair. This feature is only specific to the murine instead of the human. Moreover, several immune-regulatory cytokines that express in human, including IL-8, CXCL-7 and CXCL-11, are absent in murine, indicating a difference in tissue repair and angiogenesis between two species [223, 226, 227].

In order to bridge the gap between the interspecies differences, several strategies have been proposed. Firstly, the skin contraction resulted from the structure of panniculus carnosus in a murine model can be avoided by selecting a proper implantation site such as ears, skull and tail. These locations contain cartilages and bones underneath which can halt contraction from affecting the implantation [228]. Secondly, to simulate disease states and the immune system of human, genetically modified models such as knockout and transgenic models can be employed. In our study, STZ-induced diabetic rats were used as a testing model for potential implantable biomaterials for future diabetes-reversing implants. Nevertheless, even though STZ can cause apoptosis to insulin-producing cells in the pancreas to mimic the disease state of type 1 diabetes, the model is not representative for the real situation where the destruction of pancreatic β cells should be induced by autoimmune attacks. Type 1 diabetes is characterized by massive destruction due to the infiltration of lymphocytes and macrophages as well as the activation of autoreactive T cells [136].

This complex immune system can potentially have an influence on the FBR though the impact requires more studies for further explanation. To address the issue, Akita diabetic murine engrafted with an immune system that is nearly identical to diabetic humans can be a better model for the study [229, 230]. This model will be suitable for future human islet transplantation study since that immune system can reject transplanted islet allografts, which can be used for immune-isolation assessment for the transplantable device.

Overall, this proof-of-principle study showed a great potential of RMS as a diagnostic tool to investigate fibrotic disorders in a molecular manner. We demonstrated the capacity of RMS to discriminate Col I and classify the populations of M1-like and M2-like macrophages in fibrotic tissues. This procedure can be integrated with deep learning and offer pathologists a marker-independent, high-speed and automatic approach to perform fibrotic disorder investigation.

Chapter 5

Outlook

5. Outlook

The FBR-driven fibrotic capsule formation is the main obstacle for implantable medical devices. Despite nearly no standard approach specified for testing FBR induced by biomaterial implants, fibrotic disorders such as idiopathic pulmonary fibrosis, pulmonary fibrosis and hepatic fibrosis and cirrhosis can be evaluated by imaging diagnostic tools, including X-rays, CT scans and MRI [231, 232]. These analytical methods can be applied for the monitoring of fibrotic capsule progression for implantation. Nevertheless, imaging techniques are generally not available at primary healthcare centers due to the high prices as well as in need for experienced experts to operate the assessments. The imaging diagnosis of fibrosis in some cases can be difficult to be determined and validated, which requires patients to receive invasive tissue biopsy for a more definitive identification [233]. Furthermore, histopathological examination is determined by focally acquired specimens, which normally should not be representative of the entire organ. The results of this thesis highlighted the potential of RMS to detect pathological fibrotic tissues by generating color-coded Raman images based on specific spectral data. Every pixel of a scan contains a spectrum which indicates information about the biochemical structure of biological components.

RMS can be potentially applied to one of the intraoperative multimodal nonlinear optical imaging (NLOI) systems to assist clinical evaluation of pathology [234, 235]. This platform system can consist of multiple NLOI modalities including SHG, third harmonic generation, Raman spectroscopy, coherent anti-Stokes Raman spectroscopy, stimulated Raman spectroscopy, multiphoton fluorescence, fluorescence lifetime imaging microscopy and infrared spectroscopy. Coupling this NLOI system renders high molecular contrast and high spatial resolution in detection of intracellular dynamics and disease states [236]. Recently, the development of NLOI system has been translated from the bench to the bedside in various areas. The group of Prof. Stephen A. Boppart demonstrated the utilization of NLOI system for a needle biopsy on tumor tissues to improve the accuracy of cancer detection during tumor removal procedures [237]. The NLOI-based technology possesses the advantage of marker-independent visualization of pathological status [238]. It has been reported that

multiple NLOI modalities were applied to tissue microenvironments to promote the evaluation of tumor progression and metastasis based on the observation of crucial factors such as immune cells, collagens, blood vessels and oxy and deoxyhemoglobin [239, 240].

Toward translational research, early fibrosis diagnosis is essential to enhance the therapeutic outcomes before irreversible and non-functional fibrotic tissues replace native tissues and ultimately affect the functionality of the organs and the survival of the patients [241]. In 2017, Raman spectroscopy was first used to investigate to examine the pathological progress of liver fibrosis in rats [242]. In comparison with control groups, fibrotic tissues can be discriminated by PCA and linear discriminant analysis (LDA). Apart from Raman spectroscopy, several spectroscopic methods have been emerging to achieve fibrosis diagnosis examination in qualitative and quantitative manners. Autofluorescence spectroscopy was established to monitor different stages of hepatic fibrosis [243]. The alterations of the spectral data were observed based on the endogenous fluorophores of biological components including organic and inorganic compounds. Shaiju S. Nazeer et al. [243] showed differences in fluorophores of several biomarkers that are highly associated with the severity of liver fibrosis, including hemoglobin, lipofuscin-like substances and porphyrin in various stages of hepatic fibrosis. Along with MVA, it was able to classify mild and moderate hepatic fibrosis. Infrared spectroscopic imaging can also provide potential utility for fibrosis diagnosis. Infrared spectroscopy gains a deep understanding of molecular changes based on the frequencies difference of light absorption caused by various types of chemical bonds [244]. Similar to RMS, the spectra generated by infrared spectroscopy represent specific cellular and fibrotic biomarkers, including ECM proteins, lipids and polysaccharides [245]. Recently, Vidyani Suryadevara et al. [246] proposed infrared spectral microscopy as a novel tool to measure the grades of lung fibrosis on a murine bleomycin model. After undergoing PCA-LDA analysis, the spectra data differentiate various groups with different stages of fibrosis in accordance with the timeline from bleomycin treatment.

These spectroscopic approaches in combination with RMS, unlike histological assessment and morphological imaging techniques such as CT and MRI, can specifically characterize the molecular and compositional modifications in the

components related to fibrotic tissue formation. A potential future direction for spectroscopic methods in fibrosis research is to collect spectral data from various fibrotic disorders in different species in order to develop a database in combination with deep learning. These applications will be beneficial to future investigation of fibrosis on fresh tissue or in vivo and would allow direct diagnosis of unknown fibrotic disorders in the clinics.

Acknowledgements

I would like to express my genuine gratitude to my main supervisor Prof. Dr. Katja Schenke-Layland for the great support during my entire PhD career. I am grateful for her trust in the research and timely providing me with very constructive insights, so that I can complete various projects with peace of mind during my doctoral study. I would also like to thank to Dr. Aiden Flanagan, Prof. Dr. Garry Duffy and other colleagues at Boston Scientific and Galway University in Ireland for the great collaboration in the DELIVER program.

I would like to express my special thanks to our group leader Dr. Julia Marzi, who always gave me timely discussion whenever my research topic encountered any bottlenecks. In addition, she helped me to deal with various problems with peace of mind. More importantly, thanks to her scientific knowledge and professions, every paper underwent her proofreading and editing was successfully published. She will always be my role model. I also want to thank her for the German abstract in the thesis.

Moreover, I also would like to give my gratitude to my mentor Shannon Layland for providing me with any kind of help and advice, not only about scientific-related issues but also career discussions. I would like to thank Daniel A. Carvajal Berrio, Lucas Becker, Max Urbanczyk and Abiramy Jeyagaran for working and studying together with me and offering me good scientific suggestions during my PhD program.

I would like to express my deepest gratitude toward PhD thesis committees (Prof. Dr. Peter Loskill and Prof. Dr. Jennifer-Christina Ewald) to provide valuable questions and supports throughout the defense process. I thank everyone in Schenke-Layland lab for providing a friendly environment for me to work happily here, which makes me always have a feeling at home. Finally, I would like to thank my family and my friends for their continuous support.

Declaration

Ich erkläre hiermit, dass ich die zur Promotion eingereichte Arbeit mit dem Titel: ”Evaluation of the ECM Structures of Fibrotic Tissues by Using Raman Microspectroscopy” selbständig verfasst, nur die angegebenen Quellen und Hilfsmittel benutzt und wörtlich oder inhaltlich übernommene Zitate als solche gekennzeichnet habe. Ich erkläre, dass die Richtlinien zur Sicherung guter wissenschaftlicher Praxis der Universität Tübingen beachtet wurden. Ich versichere an Eides statt, dass diese Angaben wahr sind und dass ich nichts verschwiegen habe. Mir ist bekannt, dass die falsche Angabe einer Versicherung an Eides statt mit Freiheitsstrafe bis zu drei Jahren oder mit Geldstrafe bestraft wird.

Taipei, 23.04.26

I hereby declare that I have independently written the work submitted for the doctorate degree entitled: "Evaluation of the ECM Structures of Fibrotic Tissues by Using Raman Microspectroscopy". I have only used the specified sources and aids and have marked quotes that have been used literally or in terms of content as such. I declare that the guidelines for ensuring good scientific practice of the University of Tübingen have been observed. I swear under oath that this information is true and that I have not concealed anything. I am aware that the false statement of an affidavit will be punished with imprisonment of up to three years or with a fine.

Taipei, 23.04.26

Scientific Curriculum Vitae

Chuan-En Lu

Education

Sep. 2019– Aug. 2023	**Dr. rer. nat. candidate in Biology, Eberhard Karls Universität Tübingen** **Department of Biomedical Engineering** Advisor: Prof. Katja Schenke-Layland Thesis project: Evaluation of the ECM Structures of Fibrotic Tissues by Using Raman Microspectroscopy
Sep. 2017– Jun. 2019	**Master of Science in Biochemical Science and Technology** **National Taiwan University** Advisor: Dr. Chin-Tin Chen Thesis project: Development of nanostructured lipid carriers for a hydrophilic hypoxia-activated compound
Sep. 2011– Jun. 2016	**Bachelor of Science in Pharmacy** **Bachelor of Science in Biochemical Science and Technology (double major)** **National Taiwan University** Advisor: Dr. Chun-Jung Lin Independent project: The effects of hypoxic conditions on the expression of the multidrug and toxic compound efflux transporter (MATE1) on MDCK II cells

Employment

Jun. 2021 – July. 2022	**Visiting Researcher** Boston Scientific, NPD department, Galway, Ireland

Publications

*First co-authorship

Rachel Beatty*, **Chuan-En Lu***, Julia Marzi, Ruth E Levey, Daniel A. Carvajal Berrio, Giulia Lattanzi, Robert Wylie, Raymond O'Connor, Eimear Wallace, Eimear B Dolan1, Shannon L. Layland, Katja Schenke-Layland, Garry P Duffy. The Foreign Body Response to an Implantable Therapeutic Reservoir in a Diabetic Rodent Model. Tissue engineering. Part C, Methods vol. 27,10 (2021): 515-528. doi:10.1089/ten.TEC.2021.0163

Jeyagaran Abiramy*, **Chuan-En Lu***, Aline Zbinden, Shannon L. Layland. Type 1 Diabetes and Engineering Enhanced Islet Transplantation. Advanced drug delivery reviews vol. 189 (2022): 114481. doi:10.1016/j.addr.2022.114481

Max Urbanczyk*, Abiramy Jeyagaran*, Aline Zbinden, **Chuan-En Lu**, Julia Marzi, Shannon L. Layland, Garry Duffy, Katja Schenke-Layland. Decorin improves pancreatic β-cell function and regulates ECM expression in vitro. Matrix biology: journal of the International Society for Matrix Biology, S0945-053X (22)00154-8. 30 Dec. 2022, doi:10.1016/j.matbio.2022.12.005

Lucas Becker*, **Chuan-En Lu***, Ivonne Aidee Montes-Mojarro, Suzan Khalil, Ali Nsair, Falko Fend, Julia Marzi, Katja Schenke-Layland. Raman Microspectroscopy Identifies Fibrotic Tissues in Collagen-related Disorders via Deconvoluted Collagen Type I Spectra. Acta Biomater. 2023 Mar 15; S1742-7061(23)00150-2.

Chuan-En Lu, Ruth E Levey, Giulio Ghersi, Nathan Shueller, Simone Liebscher, Shannon L. Layland, Katja Schenke-Layland, Garry P. Duffy, Julia Marzi. Monitoring the macrophage response towards biomaterial implants using label-free imaging. Materials Today Bio Volume 21, August 2023, 100696.

Conferences

Chuan-En Lu, Julia Marzi, Daniel Carvajal Berrio, Shannon L. Layland, Garry P. Duffy and Katja Schenke-Layland. Examination of Foreign Body Response against Subcutaneous Implantation by Utilizing Raman Microspectroscopy. ePoster presentation at German Society for Matrix Biology (DGMB), 2021

Chuan-En Lu, Julia Marzi, Daniel Carvajal Berrio, Shannon L. Layland, Garry P. Duffy and Katja Schenke-Layland. Examination of Foreign Body Response against Subcutaneous Implantation by Utilizing Raman Microspectroscopy. ePoster presentation at Tissue Engineering and Regenerative Medicine International Society conference, 2021

Chuan-En Lu, Rachael Beatty, Julia Marzi, Shannon L. Layland, Aiden Flanagan, Martin Fawdry, Garry P. Duffy and Katja Schenke-Layland. Investigation of Foreign Body Response against Subcutaneous Diabetes-reversing Implantation Utilizing Raman Microspectroscopy, Poster presentation at Advanced Technologies and Treatments for Diabetes, Barcelona 2022

Chuan-En Lu, Julia Marzi, Aiden Flanagan, Martin Fawdry, Shannon L. Layland, Garry P. Duffy and Katja Schenke-Layland.. Investigation of Foreign Body Response against Subcutaneous implants via Raman Microspectroscopy. Oral presentation at Bioengineering in Ireland conference, Galway 2022

Chuan-En Lu, Rachael Beatty, Julia Marzi, Shannon L. Layland, Aiden Flanagan, Martin Fawdry, Garry P. Duffy and Katja Schenke-Layland. Investigation of Foreign Body Response against Subcutaneous Diabetes-reversing Implantation Utilizing Raman Microspectroscopy. Poster presentation at Tissue Engineering and Regenerative Medicine International Society conference, Krakow 2022

Awards

Best Poster award, German Matrix Biology Conference, 2022

3D Image at Front Cover, Tissue Engineering Part C, 2019

Marie-Curie ITN Scholarship, 2019-2022

References

[1] T.A. Wynn, T.R. Ramalingam, Mechanisms of fibrosis: therapeutic translation for fibrotic disease, Nat Med 18(7) (2012) 1028-1040.
[2] C.J. Mann, E. Perdiguero, Y. Kharraz, S. Aguilar, P. Pessina, A.L. Serrano, P. Muñoz-Cánoves, Aberrant repair and fibrosis development in skeletal muscle, Skeletal Muscle 1 (2011) 1-21.
[3] S. Ueha, F. Shand, K. Matsushima, Cellular and Molecular Mechanisms of Chronic Inflammation-Associated Organ Fibrosis, Frontiers in Immunology (2012) 3-71.
[4] S.A. Eming, P. Martin, M. Tomic-Canic, Wound repair and regeneration: mechanisms, signaling, and translation, Sci Transl Med 6(265) (2014) 265sr6.
[5] T.A. Wynn, T.R. Ramalingam, Mechanisms of fibrosis: therapeutic translation for fibrotic disease, Nat Med 18(7) (2012) 1028-40.
[6] S. Kolahian, I.E. Fernandez, O. Eickelberg, D. Hartl, Immune Mechanisms in Pulmonary Fibrosis, Am J Respir Cell Mol Biol 55(3) (2016) 309-22.
[7] E. Huang, N. Peng, F. Xiao, D. Hu, X. Wang, L. Lu, The Roles of Immune Cells in the Pathogenesis of Fibrosis, Int J Mol Sci 21(15) (2020) 5203-5230.
[8] M. Xue, C.J. Jackson, Extracellular Matrix Reorganization During Wound Healing and Its Impact on Abnormal Scarring, Adv Wound Care (New Rochelle) 4(3) (2015) 119-136.
[9] M. Zeisberg, R. Kalluri, Cellular mechanisms of tissue fibrosis. 1. Common and organ-specific mechanisms associated with tissue fibrosis, Am J Physiol Cell Physiol 304(3) (2013) C216-25.
[10] R.T. Kendall, C.A. Feghali-Bostwick, Fibroblasts in fibrosis: novel roles and mediators, Front Pharmacol 5 (2014) 1-13.
[11] D.P. Higgins, S. Hemsley, P.J. Canfield, Association of uterine and salpingeal fibrosis with chlamydial hsp60 and hsp10 antigen-specific antibodies in Chlamydia-infected koalas, Clin Diagn Lab Immunol 12(5) (2005) 632-9.
[12] E.S. White, M. Thomas, S. Stowasser, K. Tetzlaff, Challenges for Clinical Drug Development in Pulmonary Fibrosis, Front Pharmacol 13 (2022) 823085-823094.
[13] J.A. de Andrade, V.J. Thannickal, Innovative approaches to the therapy of fibrosis, Curr Opin Rheumatol 21(6) (2009) 649-55.
[14] P. Spagnolo, C.J. Ryerson, R. Putman, J. Oldham, M. Salisbury, N. Sverzellati, C. Valenzuela, S. Guler, S. Jones, M. Wijsenbeek, V. Cottin, Early diagnosis of fibrotic interstitial lung disease: challenges and opportunities, The Lancet Respiratory Medicine 9(9) (2021) 1065-1076.
[15] M. Sisto, D. Ribatti, S. Lisi, Organ Fibrosis and Autoimmunity: The Role of Inflammation in TGFβ-Dependent EMT, Biomolecules 11(2) (2021) 310-346.
[16] B. Ley, H.R. Collard, T.E. King, Jr., Clinical course and prediction of survival in idiopathic pulmonary fibrosis, Am J Respir Crit Care Med 183(4) (2011) 431-40.
[17] D.K. Hewadikaram, M. Bandara, A.N. Pattivedana, H.H.E. Jayaweera, K.M. Jayananda, W.A.M. Madhavi, A. Pallewatte, C. Jayasumana, S. Siribaddana, J.P. Wansapura, A novel ultrasound technique to detect early chronic kidney disease, F1000Res 7 (2018) 448-459.
[18] C. Labenz, A. Arslanow, M. Nguyen-Tat, M. Nagel, M.-A. Wörns, M.C. Reichert, F.J. Heil, D. Mainz, G. Zimper, B. Römer, H. Binder, E. Farin-Glattacker, U. Fichtner, E. Graf, D. Stelzer, R. Van Ewijk, J. Ortner, L. Velthuis, F. Lammert, P.R. Galle, Structured Early detection of Asymptomatic Liver Cirrhosis: Results of the population-based liver screening program SEAL, Journal of Hepatology 77(3) (2022) 695-701.

[19] S.B. Montesi, P. Désogère, B.C. Fuchs, P. Caravan, Molecular imaging of fibrosis: recent advances and future directions, J Clin Invest 129(1) (2019) 24-33.
[20] M. Mura, M.A. Porretta, E. Bargagli, G. Sergiacomi, M. Zompatori, N. Sverzellati, A. Taglieri, F. Mezzasalma, P. Rottoli, C. Saltini, P. Rogliani, Predicting survival in newly diagnosed idiopathic pulmonary fibrosis: a 3-year prospective study, European Respiratory Journal 40(1) (2012) 101-109.
[21] M. Molina-Molina, M. Aburto, O. Acosta, J. Ancochea, J.A. Rodríguez-Portal, J. Sauleda, C. Lines, A. Xaubet, Importance of early diagnosis and treatment in idiopathic pulmonary fibrosis, Expert Review of Respiratory Medicine 12(7) (2018) 537-539.
[22] S. Bhat, A. Kumar, Biomaterials and bioengineering tomorrow's healthcare, Biomatter 3(3) (2013) e24717.
[23] O. Veiseh, A.J. Vegas, Domesticating the foreign body response: Recent advances and applications, Adv Drug Deliv Rev 144 (2019) 148-161.
[24] W. Kenneth Ward, A review of the foreign-body response to subcutaneously-implanted devices: the role of macrophages and cytokines in biofouling and fibrosis, J Diabetes Sci Technol 2(5) (2008) 768-77.
[25] T.O. Socarrás, A.C. Vasconcelos, P.P. Campos, N.B. Pereira, J.P. Souza, S.P. Andrade, Foreign body response to subcutaneous implants in diabetic rats, PLoS One 9(11) (2014) e110945.
[26] W.J. Geelhoed, L. Moroni, J.I. Rotmans, Utilizing the Foreign Body Response to Grow Tissue Engineered Blood Vessels in Vivo, Journal of Cardiovascular Translational Research 10(2) (2017) 167-179.
[27] A. Carnicer-Lombarte, S.-T. Chen, G.G. Malliaras, D.G. Barone, Foreign Body Reaction to Implanted Biomaterials and Its Impact in Nerve Neuroprosthetics, Frontiers in Bioengineering and Biotechnology 9 (2021) 622524.
[28] A. Carnicer-Lombarte, S.T. Chen, G.G. Malliaras, D.G. Barone, Foreign Body Reaction to Implanted Biomaterials and Its Impact in Nerve Neuroprosthetics, Front Bioeng Biotechnol 9 (2021) 622524.
[29] O. Faruq, P.N. Chien, N. Dönmez, S.-Y. Nam, C.-Y. Heo, Functionalization of Silicone Surface with Drugs and Polymers for Regulation of Capsular Contracture, Polymers 13(16) (2021) 2731.
[30] G. Fumagall, V. Panichi, Chapter 151 - Biocompatibility of the Dialysis System, in: C. Ronco, R. Bellomo, J.A. Kellum, Z. Ricci (Eds.), Critical Care Nephrology (Third Edition), Elsevier, Philadelphia, 2019, pp. 918-922.e2.
[31] L. Vroman, A.L. Adams, G.C. Fischer, P.C. Munoz, Interaction of high molecular weight kininogen, factor XII, and fibrinogen in plasma at interfaces, Blood 55(1) (1980) 156-9.
[32] J. Kzhyshkowska, A. Gudima, V. Riabov, C. Dollinger, P. Lavalle, N.E. Vrana, Macrophage responses to implants: prospects for personalized medicine, J Leukoc Biol 98(6) (2015) 953-62.
[33] C. Davoust, B. Plas, A. Béduer, B. Demain, A.-S. Salabert, J.C. Sol, C. Vieu, L. Vaysse, I. Loubinoux, Regenerative potential of primary adult human neural stem cells on micropatterned bio-implants boosts motor recovery, Stem Cell Research & Therapy 8(1) (2017) 253-267.
[34] M. Blanter, M. Gouwy, S. Struyf, Studying Neutrophil Function in vitro: Cell Models and Environmental Factors, J Inflamm Res 14 (2021) 141-162.
[35] E. Mariani, G. Lisignoli, R.M. Borzì, L. Pulsatelli, Biomaterials: Foreign Bodies or Tuners for the Immune Response?, Int J Mol Sci 20(3) (2019) 636-678.

[36] A.N. Orekhov, V.A. Orekhova, N.G. Nikiforov, V.A. Myasoedova, A.V. Grechko, E.B. Romanenko, D. Zhang, D.A. Chistiakov, Monocyte differentiation and macrophage polarization, Vessel Plus 3 (2019) 10-30.
[37] S. Ivanovski, P.M. Bartold, Y.S. Huang, The role of foreign body response in peri-implantitis: What is the evidence?, Periodontol 2000 90(1) (2022) 176-185.
[38] N. Noskovicova, B. Hinz, P. Pakshir, Implant Fibrosis and the Underappreciated Role of Myofibroblasts in the Foreign Body Reaction, Cells 10(7) (2021) 1794-1820.
[39] P.J. Murray, Macrophage Polarization, Annu Rev Physiol 79 (2017) 541-566.
[40] J. Kzhyshkowska, A. Gudima, V. Riabov, C. Dollinger, P. Lavalle, N.E. Vrana, Macrophage responses to implants: prospects for personalized medicine, Journal of Leukocyte Biology 98(6) (2015) 953-962.
[41] F.Y. McWhorter, T. Wang, P. Nguyen, T. Chung, W.F. Liu, Modulation of macrophage phenotype by cell shape, Proceedings of the National Academy of Sciences 110(43) (2013) 17253-17258.
[42] J.M. Anderson, Biological Responses to Materials, Annual Review of Materials Research 31(1) (2001) 81-110.
[43] Implants that vanish, Nature Biomedical Engineering 3(8) (2019) 585-594.
[44] K. Hansen, B.T. Mossman, Generation of superoxide (O2-.) from alveolar macrophages exposed to asbestiform and nonfibrous particles, Cancer Res 47(6) (1987) 1681-6.
[45] K.L. Spiller, R.R. Anfang, K.J. Spiller, J. Ng, K.R. Nakazawa, J.W. Daulton, G. Vunjak-Novakovic, The role of macrophage phenotype in vascularization of tissue engineering scaffolds, Biomaterials 35(15) (2014) 4477-88.
[46] R.A. Ignotz, J. Massagué, Transforming growth factor-beta stimulates the expression of fibronectin and collagen and their incorporation into the extracellular matrix, J Biol Chem 261(9) (1986) 4337-45.
[47] J.C. Bonner, Regulation of PDGF and its receptors in fibrotic diseases, Cytokine Growth Factor Rev 15(4) (2004) 255-73.
[48] A.V. Shinde, C. Humeres, N.G. Frangogiannis, The role of α-smooth muscle actin in fibroblast-mediated matrix contraction and remodeling, Biochim Biophys Acta Mol Basis Dis 1863(1) (2017) 298-309.
[49] T.A. Wynn, Cellular and molecular mechanisms of fibrosis, J Pathol 214(2) (2008) 199-210.
[50] D.T. Luttikhuizen, M.C. Harmsen, M.J. Van Luyn, Cellular and molecular dynamics in the foreign body reaction, Tissue Eng 12(7) (2006) 1955-70.
[51] I. Bourgot, I. Primac, T. Louis, A. Noël, E. Maquoi, Reciprocal Interplay Between Fibrillar Collagens and Collagen-Binding Integrins: Implications in Cancer Progression and Metastasis, Front Oncol 10 (2020) 1488-1506.
[52] I.A. Darby, B. Laverdet, F. Bonté, A. Desmoulière, Fibroblasts and myofibroblasts in wound healing, Clin Cosmet Investig Dermatol 7 (2014) 301-11.
[53] G. Wick, A. Backovic, E. Rabensteiner, N. Plank, C. Schwentner, R. Sgonc, The immunology of fibrosis: innate and adaptive responses, Trends Immunol 31(3) (2010) 110-9.
[54] M. D'Urso, N.A. Kurniawan, Mechanical and Physical Regulation of Fibroblast-Myofibroblast Transition: From Cellular Mechanoresponse to Tissue Pathology, Front Bioeng Biotechnol 8 (2020) 609653.
[55] S. Albeiroti, A. Soroosh, C.A. de la Motte, Hyaluronan's Role in Fibrosis: A Pathogenic Factor or a Passive Player?, Biomed Res Int 2015 (2015) 790203.

[56] C. Bonnans, J. Chou, Z. Werb, Remodelling the extracellular matrix in development and disease, Nature reviews. Molecular cell biology 15(12) (2014) 786-801.
[57] F. Klingberg, B. Hinz, E.S. White, The myofibroblast matrix: implications for tissue repair and fibrosis, The Journal of pathology 229(2) (2013) 298-309.
[58] D.M. Hudson, M. Archer, J. Rai, M. Weis, R.J. Fernandes, D.R. Eyre, Age-related type I collagen modifications reveal tissue-defining differences between ligament and tendon, Matrix Biol Plus 12 (2021) 100070.
[59] X. Liu, H. Wu, M. Byrne, S. Krane, R. Jaenisch, Type III collagen is crucial for collagen I fibrillogenesis and for normal cardiovascular development, Proc Natl Acad Sci U S A 94(5) (1997) 1852-6.
[60] C.E. Witherel, D. Abebayehu, T.H. Barker, K.L. Spiller, Macrophage and Fibroblast Interactions in Biomaterial-Mediated Fibrosis, Adv Healthc Mater 8(4) (2019) e1801451.
[61] M.A. Karsdal, T. Manon-Jensen, F. Genovese, J.H. Kristensen, M.J. Nielsen, J.M. Sand, N.U. Hansen, A.C. Bay-Jensen, C.L. Bager, A. Krag, A. Blanchard, H. Krarup, D.J. Leeming, D. Schuppan, Novel insights into the function and dynamics of extracellular matrix in liver fibrosis, Am J Physiol Gastrointest Liver Physiol 308(10) (2015) G807-30.
[62] R. Basson, A. Bayat, Chapter 7 - Fibrosis and diabetes: Chronic hyperglycemia triggers organ-specific fibrotic mechanisms, in: D. Bagchi, A. Das, S. Roy (Eds.), Wound Healing, Tissue Repair, and Regeneration in Diabetes, Academic Press2020, pp. 121-147.
[63] I. Tuleta, N.G. Frangogiannis, Diabetic fibrosis, Biochim Biophys Acta Mol Basis Dis 1867(4) (2021) 166044.
[64] L. Alex, I. Russo, V. Holoborodko, N.G. Frangogiannis, Characterization of a mouse model of obesity-related fibrotic cardiomyopathy that recapitulates features of human heart failure with preserved ejection fraction, Am J Physiol Heart Circ Physiol 315(4) (2018) H934-h949.
[65] Y. Zhou, M.H. Poczatek, K.H. Berecek, J.E. Murphy-Ullrich, Thrombospondin 1 mediates angiotensin II induction of TGF-beta activation by cardiac and renal cells under both high and low glucose conditions, Biochem Biophys Res Commun 339(2) (2006) 633-41.
[66] D. de Gonzalo-Calvo, R.W. van der Meer, L.J. Rijzewijk, J.W. Smit, E. Revuelta-Lopez, L. Nasarre, J.C. Escola-Gil, H.J. Lamb, V. Llorente-Cortes, Serum microRNA-1 and microRNA-133a levels reflect myocardial steatosis in uncomplicated type 2 diabetes, Sci Rep 7(1) (2017) 47-61.
[67] A. Berbudi, N. Rahmadika, A.I. Tjahjadi, R. Ruslami, Type 2 Diabetes and its Impact on the Immune System, Curr Diabetes Rev 16(5) (2020) 442-449.
[68] P. Krzyszczyk, R. Schloss, A. Palmer, F. Berthiaume, The Role of Macrophages in Acute and Chronic Wound Healing and Interventions to Promote Pro-wound Healing Phenotypes, Front Physiol 9 (2018) 419-502.
[69] F.Y. Chow, D.J. Nikolic-Paterson, E. Ozols, R.C. Atkins, G.H. Tesch, Intercellular adhesion molecule-1 deficiency is protective against nephropathy in type 2 diabetic db/db mice, J Am Soc Nephrol 16(6) (2005) 1711-22.
[70] F.Y. Chow, D.J. Nikolic-Paterson, F.Y. Ma, E. Ozols, B.J. Rollins, G.H. Tesch, Monocyte chemoattractant protein-1-induced tissue inflammation is critical for the development of renal injury but not type 2 diabetes in obese db/db mice, Diabetologia 50(2) (2007) 471-80.

[71] C.R. Ban, S.M. Twigg, Fibrosis in diabetes complications: pathogenic mechanisms and circulating and urinary markers, Vasc Health Risk Manag 4(3) (2008) 575-96.
[72] I. Tuleta, N.G. Frangogiannis, Fibrosis of the diabetic heart: Clinical significance, molecular mechanisms, and therapeutic opportunities, Adv Drug Deliv Rev 176 (2021) 113904.
[73] V.P. Singh, A. Bali, N. Singh, A.S. Jaggi, Advanced glycation end products and diabetic complications, Korean J Physiol Pharmacol 18(1) (2014) 1-14.
[74] M.E. Cooper, Importance of advanced glycation end products in diabetes-associated cardiovascular and renal disease, Am J Hypertens 17(12 Pt 2) (2004) 31s-38s.
[75] K. Neelofar, J. Ahmad, Amadori albumin in diabetic nephropathy, Indian J Endocrinol Metab 19(1) (2015) 39-46.
[76] J.G. Snedeker, A. Gautieri, The role of collagen crosslinks in ageing and diabetes - the good, the bad, and the ugly, Muscles Ligaments Tendons J 4(3) (2014) 303-8.
[77] M.E. Cooper, Importance of advanced glycation end products in diabetes-associated cardiovascular and renal disease, American journal of hypertension 17 12 Pt 2 (2004) 31S-38S.
[78] G. Hiremath, A. Locke, A. Sivakumar, G. Thomas, A. Mahadevan-Jansen, Clinical translational application of Raman spectroscopy to advance Benchside biochemical characterization to bedside diagnosis of esophageal diseases, Journal of Gastroenterology and Hepatology 34(11) (2019) 1911-1921.
[79] K.I. Hadjiivanov, D.A. Panayotov, M.Y. Mihaylov, E.Z. Ivanova, K.K. Chakarova, S.M. Andonova, N.L. Drenchev, Power of Infrared and Raman Spectroscopies to Characterize Metal-Organic Frameworks and Investigate Their Interaction with Guest Molecules, Chemical Reviews 121(3) (2021) 1286-1424.
[80] E.T. Sato, H. Martinho, First-principles calculations of Raman vibrational modes in the fingerprint region for connective tissue, Biomed. Opt. Express 9(4) (2018) 1728-1734.
[81] M. Gawrilow, M.A. Suhm, Quantifying Conformational Isomerism in Chain Molecules by Linear Raman Spectroscopy: The Case of Methyl Esters, Molecules 26(15) (2021) 4523.
[82] J. Matysik, P. Hildebrandt, K. Smit, F. Mark, W. Gärtner, S.E. Braslavsky, K. Schaffner, B. Schrader, Raman spectroscopic analysis of isomers of biliverdin dimethyl ester, Journal of Pharmaceutical and Biomedical Analysis 15(9) (1997) 1319-1324.
[83] S.A. Ali, A. Irfan, A. Mazumder, S. Balendhran, T. Ahmed, S. Walia, A. Ulhaq, Helicity-selective Raman scattering from in-plane anisotropic α-MoO3, Applied Physics Letters 119(19) (2021) 193104.
[84] Y. Zhang, H. Hong, W. Cai, Imaging with Raman spectroscopy, Curr Pharm Biotechnol 11(6) (2010) 654-61.
[85] A.T. Young, Rayleigh scattering, Appl Opt 20(4) (1981) 533-5.
[86] M. Krstić, S. Ražić, Analytical Approaches to the Characterization of Solid Drug Delivery Systems with Porous Adsorbent Carriers, Current Medicinal Chemistry 2018 (2018) 3956-3972.
[87] R.R. Jones, D.C. Hooper, L. Zhang, D. Wolverson, V.K. Valev, Raman Techniques: Fundamentals and Frontiers, Nanoscale Research Letters 14(1) (2019) 231-245.

[88] C. di Lauro, 8 - Spectra of Symmetric Top and Linear Molecules, in: C. di Lauro (Ed.), Rotational Structure in Molecular Infrared Spectra, Elsevier, Boston, 2013, pp. 119-203.
[89] B. Chatterjee, N. Kalyani, S. Das, A. Anand, T.K. Sharma, Chapter 2 - Nano-realm for point-of-care (POC) bacterial diagnostics, in: V. Gurtler, A.S. Ball, S. Soni (Eds.), Methods in Microbiology, Academic Press2019, pp. 19-42.
[90] S. Li, Y. Li, R. Yi, L. Liu, J. Qu, Coherent Anti-Stokes Raman Scattering Microscopy and Its Applications, Frontiers in Physics 8 (2020) 598420.
[91] G.J. Fiechtner, J.R. Gord, Absorption and the dimensionless overlap integral for two-photon excitation, Journal of Quantitative Spectroscopy and Radiative Transfer 68(5) (2001) 543-557.
[92] B.L. Klarenaar, F. Brehmer, S. Welzel, H.J. van der Meiden, M.C. van de Sanden, R. Engeln, Note: Rotational Raman scattering on CO_2 plasma using a volume Bragg grating as a notch filter, Rev Sci Instrum 86(4) (2015) 046106.
[93] I. Pavić, J. Šoda, V. Gašparić, M. Ivanda, Raman and Photoluminescence Spectroscopy with a Variable Spectral Resolution, Sensors (Basel) 21(23) (2021) 7951-7962.
[94] K.J.I. Ember, M.A. Hoeve, S.L. McAughtrie, M.S. Bergholt, B.J. Dwyer, M.M. Stevens, K. Faulds, S.J. Forbes, C.J. Campbell, Raman spectroscopy and regenerative medicine: a review, npj Regenerative Medicine 2(1) (2017) 12-23.
[95] A. Javaeed, S. Qamar, S. Ali, M.A.T. Mustafa, A. Nusrat, S.K. Ghauri, Histological Stains in the Past, Present, and Future, Cureus 13(10) (2021) e18486.
[96] N.C. Foot, The Masson Trichrome Staining Methods in Routine Laboratory Use, Stain Technology 8(3) (1933) 101-110.
[97] H.Z. Movat, Demonstration of all connective tissue elements in a single section; pentachrome stains, AMA Arch Pathol 60(3) (1955) 289-95.
[98] L.C. Junqueira, G. Bignolas, R.R. Brentani, Picrosirius staining plus polarization microscopy, a specific method for collagen detection in tissue sections, Histochem J 11(4) (1979) 447-55.
[99] S.A. Taqi, S.A. Sami, L.B. Sami, S.A. Zaki, A review of artifacts in histopathology, J Oral Maxillofac Pathol 22(2) (2018) 279-250.
[100] J.E. Scott, R.A. Stockwell, On the use and abuse of the critical electrolyte concentration approach to the localization of tissue polyanions, J Histochem Cytochem 15(2) (1967) 111-3.
[101] S. Magaki, S.A. Hojat, B. Wei, A. So, W.H. Yong, An Introduction to the Performance of Immunohistochemistry, Methods in molecular biology (Clifton, N.J.) 1897 (2019) 289-298.
[102] M.S. Bergholt, A. Serio, M.B. Albro, Raman Spectroscopy: Guiding Light for the Extracellular Matrix, Front Bioeng Biotechnol 7 (2019) 303-316.
[103] J.J.A. Poole, L.B. Mostaço-Guidolin, Optical Microscopy and the Extracellular Matrix Structure: A Review, Cells 10(7) (2021) 1760-1785.
[104] S.M. Usmani, T.R. Mempel, Chapter 10 - Intravital Microscopy, in: B.D. Ross, S.S. Gambhir (Eds.), Molecular Imaging (Second Edition), Academic Press2021, pp. 167-192.
[105] A. Kunstar, A.M. Leferink, P.I. Okagbare, M.D. Morris, B.J. Roessler, C. Otto, M. Karperien, C.A. van Blitterswijk, L. Moroni, A.A. van Apeldoorn, Label-free Raman monitoring of extracellular matrix formation in three-dimensional polymeric scaffolds, J R Soc Interface 10(86) (2013) 20130464.
[106] M.S. Bergholt, J.-P. St-Pierre, G.S. Offeddu, P.A. Parmar, M.B. Albro, J.L. Puetzer, M.L. Oyen, M.M. Stevens, Raman Spectroscopy Reveals New Insights into

the Zonal Organization of Native and Tissue-Engineered Articular Cartilage, ACS Cent Sci 2(12) (2016) 885-895.
[107] M. Fosca, V. Basoli, E. Della Bella, F. Russo, G. Vadalà, M. Alini, J.V. Rau, S. Verrier, Raman Spectroscopy in Skeletal Tissue Disorders and Tissue Engineering: Present and Prospective, Tissue Engineering Part B: Reviews (2021) 949-965.
[108] B.G. Frushour, J.L. Koenig, Raman scattering of collagen, gelatin, and elastin, Biopolymers 14(2) (1975) 379-91.
[109] R. Beatty, C.E. Lu, J. Marzi, R.E. Levey, D. Carvajal Berrio, G. Lattanzi, R. Wylie, R. O'Connor, E. Wallace, G. Ghersi, M. Salamone, E.B. Dolan, S.L. Layland, K. Schenke-Layland, G.P. Duffy, The Foreign Body Response to an Implantable Therapeutic Reservoir in a Diabetic Rodent Model, Tissue Eng Part C Methods 27(10) (2021) 515-528.
[110] P. Casal-Beiroa, V. Balboa-Barreiro, N. Oreiro, S. Pértega-Díaz, F.J. Blanco, J. Magalhães, Optical Biomarkers for the Diagnosis of Osteoarthritis through Raman Spectroscopy: Radiological and Biochemical Validation Using Ex Vivo Human Cartilage Samples, Diagnostics (Basel) 11(3) (2021) 546-562.
[111] R.M. Spiers, J. Marzi, E.M. Brauchle, S.E. Cross, R.H. Vaughan, P.A. Bateman, S.J. Hughes, K. Schenke-Layland, P.R.V. Johnson, Donor age significantly influences the Raman spectroscopic biomolecular fingerprint of human pancreatic extracellular matrix proteins following collagenase-based digestion, Acta Biomater 99 (2019) 269-283.
[112] E. Brauchle, H. Bauer, P. Fernes, A. Zuk, K. Schenke-Layland, G. Sengle, Raman microspectroscopy as a diagnostic tool for the non-invasive analysis of fibrillin-1 deficiency in the skin and in the in vitro skin models, Acta Biomaterialia 52 (2017) 41-48.
[113] A. Kunstar, A.M. Leferink, P.I. Okagbare, M.D. Morris, B.J. Roessler, C. Otto, M. Karperien, C.A. van Blitterswijk, L. Moroni, A.A. van Apeldoorn, Label-free Raman monitoring of extracellular matrix formation in three-dimensional polymeric scaffolds, Journal of the Royal Society, Interface 10(86) (2013) 20130464-20130464.
[114] H. Lin, H.J. Lee, N. Tague, J.-B. Lugagne, C. Zong, F. Deng, J. Shin, L. Tian, W. Wong, M.J. Dunlop, J.-X. Cheng, Microsecond fingerprint stimulated Raman spectroscopic imaging by ultrafast tuning and spatial-spectral learning, Nature Communications 12(1) (2021) 3052.
[115] J. Padmanabhan, Z.N. Maan, S.H. Kwon, R. Kosaraju, C.A. Bonham, G.C. Gurtner, In Vivo Models for the Study of Fibrosis, Adv Wound Care (New Rochelle) 8(12) (2019) 645-654.
[116] T. Minamikawa, E. Hase, M. Ichimura-Shimizu, Y. Morimoto, A. Suzuki, T. Yasui, S. Nakamura, A. Tsutsui, K. Takaguchi, K. Tsuneyama, Assessment of Ultra-Early-Stage Liver Fibrosis in Human Non-Alcoholic Fatty Liver Disease by Second-Harmonic Generation Microscopy, Int J Mol Sci 23(6) (2022) 3357.
[117] D. Paramitha, M.F. Ulum, A. Purnama, D.H.B. Wicaksono, D. Noviana, H. Hermawan, 2 - Monitoring degradation products and metal ions in vivo, in: R.J. Narayan (Ed.), Monitoring and Evaluation of Biomaterials and their Performance In Vivo, Woodhead Publishing2017, pp. 19-44.
[118] J. Winters, M. Braunmuhl, S. Zeemering, M. Gilbers, T. Brink, B. Scaf, E. Guasch, L. Mont, M. Batlle, M. Sinner, S. Hatem, M. Mansour, L. Fabritz, L. Sommerfeld, P. Kirchhof, A. Isaacs, M. Stoll, U. Schotten, S. Verheule, JavaCyte, a novel open-source tool for automated quantification of key hallmarks of cardiac structural remodeling, Scientific Reports 10 (2020) 20074-20100.

[119] D. Mayerich, M.J. Walsh, A. Kadjacsy-Balla, P.S. Ray, S.M. Hewitt, R. Bhargava, Stain-less staining for computed histopathology, Technology (Singap World Sci) 3(1) (2015) 27-31.
[120] S. Ricard-Blum, The collagen family, Cold Spring Harb Perspect Biol 3(1) (2011) a004978.
[121] L. Arseni, A. Lombardi, D. Orioli, From Structure to Phenotype: Impact of Collagen Alterations on Human Health, Int J Mol Sci 19(5) (2018).
[122] I.N. Amirrah, Y. Lokanathan, I. Zulkiflee, M. Wee, A. Motta, M.B. Fauzi, A Comprehensive Review on Collagen Type I Development of Biomaterials for Tissue Engineering: From Biosynthesis to Bioscaffold, Biomedicines 10(9) (2022) 1407-1443.
[123] K.A. Wegner, A. Keikhosravi, K.W. Eliceiri, C.M. Vezina, Fluorescence of Picrosirius Red Multiplexed With Immunohistochemistry for the Quantitative Assessment of Collagen in Tissue Sections, J Histochem Cytochem 65(8) (2017) 479-490.
[124] J. Liu, M.-Y. Xu, J. Wu, H. Zhang, L. Yang, D.-X. Lun, Y.-C. Hu, B. Liu, Picrosirius-Polarization Method for Collagen Fiber Detection in Tendons: A Mini-Review, Orthop Surg 13(3) (2021) 701-707.
[125] L. Rich, P. Whittaker, Collagen and Picrosirius Red Staining: A polarized light assessment of fibrillar hue and spatial distribution, J. morphol. Sci 22 (2005) 97-104.
[126] T. Wong, A. Mead, P. Khaw, Matrix metalloproteinase inhibition modulates postoperative scarring after experimental glaucoma filtration surgery, Investigative ophthalmology & visual science 44 (2003) 1097-103.
[127] M.G. Monaghan, M. Holeiter, E. Brauchle, S.L. Layland, Y. Lu, A. Deb, A. Pandit, A. Nsair, K. Schenke-Layland, Exogenous miR-29B Delivery Through a Hyaluronan-Based Injectable System Yields Functional Maintenance of the Infarcted Myocardium, Tissue Engineering Part A 24(1-2) (2018) 57-67.
[128] U. Park, M.S. Lee, J. Jin, S. Lee, M. Hwang, Y. Wang, H.S. Yang, K. Kim, Coacervate-mediated Exogenous Growth Factor Delivery for Scarless Skin Regeneration, Acta Biomaterialia 90 (2019) 179-191.
[129] H. Hutson, T. Marohl, M. Anderson, K. Eliceiri, P. Campagnola, K. Masters, Calcific Aortic Valve Disease Is Associated with Layer-Specific Alterations in Collagen Architecture, PLOS ONE 11 (2016) 1-18.
[130] E. Brauchle, J. Kasper, R. Daum, N. Schierbaum, C. Falch, A. Kirschniak, T.E. Schäffer, K. Schenke-Layland, Biomechanical and biomolecular characterization of extracellular matrix structures in human colon carcinomas, Matrix Biol 68-69 (2018) 180-193.
[131] A.C. Biermann, J. Marzi, E. Brauchle, J.L. Wichmann, C.T. Arendt, V. Puntmann, E. Nagel, S. Abdelaziz, A.G. Winter, K.G.M. Brockbank, S. Layland, K. Schenke-Layland, U.A. Stock, Improved long-term durability of allogeneic heart valves in the orthotopic sheep model, Eur J Cardiothorac Surg 55(3) (2019) 484-493.
[132] S.J. Park, H. Choi, J.H. Kim, C.-S. Kim, Antifibrotic effects of eupatilin on TGF-β1-treated human vocal fold fibroblasts, PLOS ONE 16(3) (2021) e0249041.
[133] C.F. Hung, M.G. Rohani, S.S. Lee, P. Chen, L.M. Schnapp, Role of IGF-1 pathway in lung fibroblast activation, Respir Res 14(1) (2013) 102-114.
[134] E.F. Redente, S. Chakraborty, S. Sajuthi, B.P. Black, B.L. Edelman, M.A. Seibold, D.W. Riches, Loss of Fas signaling in fibroblasts impairs homeostatic fibrosis resolution and promotes persistent pulmonary fibrosis, JCI Insight 6(1) (2020) e141618.
[135] S. de Portu, L. Vorrink, R. Re, J. Shin, J. Castaneda, A. Habteab, O. Cohen, Randomised controlled trial of Advanced Hybrid Closed Loop in an Adult Population

with Type 1 Diabetes (ADAPT): study protocol and rationale, BMJ Open 12(2) (2022) e050635.
[136] A. Jeyagaran, C.E. Lu, A. Zbinden, A.L. Birkenfeld, S.Y. Brucker, S.L. Layland, Type 1 diabetes and engineering enhanced islet transplantation, Adv Drug Deliv Rev 189 (2022) 114481.
[137] W. Whyte, D. Goswami, S.X. Wang, Y. Fan, N.A. Ward, R.E. Levey, R. Beatty, S.T. Robinson, D. Sheppard, R. O'Connor, D.S. Monahan, L. Trask, K.L. Mendez, C.E. Varela, M.A. Horvath, R. Wylie, J. O'Dwyer, D.A. Domingo-Lopez, A.S. Rothman, G.P. Duffy, E.B. Dolan, E.T. Roche, Dynamic actuation enhances transport and extends therapeutic lifespan in an implantable drug delivery platform, Nature Communications 13(1) (2022) 4496.
[138] E.B. Dolan, C.E. Varela, K. Mendez, W. Whyte, R.E. Levey, S.T. Robinson, E. Maye, J. O'Dwyer, R. Beatty, A. Rothman, Y. Fan, J. Hochstein, S.E. Rothenbucher, R. Wylie, J.R. Starr, M. Monaghan, P. Dockery, G.P. Duffy, E.T. Roche, An actuatable soft reservoir modulates host foreign body response, Sci Robot 4(33) (2019) eaax7043.
[139] S.F. Spampinato, G.I. Caruso, R. De Pasquale, M.A. Sortino, S. Merlo, The Treatment of Impaired Wound Healing in Diabetes: Looking among Old Drugs, Pharmaceuticals (Basel) 13(4) (2020) 60-77.
[140] S. Patel, S. Srivastava, M.R. Singh, D. Singh, Mechanistic insight into diabetic wounds: Pathogenesis, molecular targets and treatment strategies to pace wound healing, Biomedicine & Pharmacotherapy 112 (2019) 108615.
[141] R. Wan, J.P. Weissman, K. Grundman, L. Lang, D.J. Grybowski, R.D. Galiano, Diabetic wound healing: The impact of diabetes on myofibroblast activity and its potential therapeutic treatments, Wound Repair Regen 29(4) (2021) 573-581.
[142] Y. Liu, Y. Liu, W. He, X. Mu, X. Wu, J. Deng, X. Nie, Fibroblasts: Immunomodulatory factors in refractory diabetic wound healing, Front Immunol 13 (2022) 918223.
[143] J.E. McDermott, J. Wang, H. Mitchell, B.J. Webb-Robertson, R. Hafen, J. Ramey, K.D. Rodland, Challenges in Biomarker Discovery: Combining Expert Insights with Statistical Analysis of Complex Omics Data, Expert Opin Med Diagn 7(1) (2013) 37-51.
[144] G. Fessel, Y. Li, V. Diederich, M. Guizar-Sicairos, P. Schneider, D.R. Sell, V.M. Monnier, J.G. Snedeker, Advanced Glycation End-Products Reduce Collagen Molecular Sliding to Affect Collagen Fibril Damage Mechanisms but Not Stiffness, PLOS ONE 9(11) (2014) e110948.
[145] A. Goldin, J.A. Beckman, A.M. Schmidt, M.A. Creager, Advanced Glycation End Products, Circulation 114(6) (2006) 597-605.
[146] C.A. Téllez S, T.O. Mendes, L. dos Santos, M.G.P. Silva, L. Pereira, P. Fávero, P. Singh, A.A. Martin, Combined in vivo confocal Raman spectroscopy and density functional theory to detect carboxymethyl(lysine) in the human stratum corneum, Vibrational Spectroscopy 100 (2019) 40-47.
[147] J.R. Beattie, A.M. Pawlak, M.E. Boulton, J. Zhang, V.M. Monnier, J.J. McGarvey, A.W. Stitt, Multiplex analysis of age-related protein and lipid modifications in human Bruch's membrane, The FASEB Journal 24(12) (2010) 4816-4824.
[148] F. Alsamad, B. Brunel, V. Vuiblet, P. Gillery, S. Jaisson, O. Piot, In depth investigation of collagen non-enzymatic glycation by Raman spectroscopy, Spectrochimica Acta Part A: Molecular and Biomolecular Spectroscopy 251 (2021) 119382.
[149] A.L. Tatler, Recent advances in the non-invasive assessment of fibrosis using biomarkers, Current Opinion in Pharmacology 49 (2019) 110-115.

[150] T. Minamikawa, E. Hase, M. Ichimura-Shimizu, Y. Morimoto, A. Suzuki, T. Yasui, S. Nakamura, A. Tsutsui, K. Takaguchi, K. Tsuneyama, Assessment of Ultra-Early-Stage Liver Fibrosis in Human Non-Alcoholic Fatty Liver Disease by Second-Harmonic Generation Microscopy, Int J Mol Sci 23(6) (2022) 3357-3374.
[151] M. Cohen-Naftaly, S.L. Friedman, Current status of novel antifibrotic therapies in patients with chronic liver disease, Therap Adv Gastroenterol 4(6) (2011) 391-417.
[152] S.M. Morris, Jr., Arginine metabolism: boundaries of our knowledge, J Nutr 137(6 Suppl 2) (2007) 1602s-1609s.
[153] A. Sica, A. Mantovani, Macrophage plasticity and polarization: in vivo veritas, The Journal of Clinical Investigation 122(3) (2012) 787-795.
[154] M. Polasek, B.C. Fuchs, R. Uppal, D.T. Schühle, J.K. Alford, G.S. Loving, S. Yamada, L. Wei, G.Y. Lauwers, A.R. Guimaraes, K.K. Tanabe, P. Caravan, Molecular MR imaging of liver fibrosis: A feasibility study using rat and mouse models, Journal of Hepatology 57(3) (2012) 549-555.
[155] P. Caravan, Y. Yang, R. Zachariah, A. Schmitt, M. Mino-Kenudson, H.H. Chen, D.E. Sosnovik, G. Dai, B.C. Fuchs, M. Lanuti, Molecular Magnetic Resonance Imaging of Pulmonary Fibrosis in Mice, American Journal of Respiratory Cell and Molecular Biology 49(6) (2013) 1120-1126.
[156] J. Bella, M. Eaton, B. Brodsky, H.M. Berman, Crystal and molecular structure of a collagen-like peptide at 1.9 A resolution, Science 266(5182) (1994) 75-81.
[157] R.Z. Kramer, J. Bella, P. Mayville, B. Brodsky, H.M. Berman, Sequence dependent conformational variations of collagen triple-helical structure, Nat Struct Biol 6(5) (1999) 454-7.
[158] M. Yamauchi, M. Sricholpech, Lysine post-translational modifications of collagen, Essays Biochem 52 (2012) 113-133.
[159] E.G. Canty-Laird, Y. Lu, K.E. Kadler, Stepwise proteolytic activation of type I procollagen to collagen within the secretory pathway of tendon fibroblasts in situ, Biochem J 441(2) (2012) 707-717.
[160] S. Jimi, S. Koizumi, K. Sato, M. Miyazaki, A. Saparov, Collagen-derived dipeptide Pro-Hyp administration accelerates muscle regenerative healing accompanied by less scarring after wounding on the abdominal wall in mice, Sci Rep 11(1) (2021) 18750.
[161] P. Rappu, A.M. Salo, J. Myllyharju, J. Heino, Role of prolyl hydroxylation in the molecular interactions of collagens, Essays Biochem 63(3) (2019) 325-335.
[162] S. Perret, C. Merle, S. Bernocco, P. Berland, R. Garrone, D.J. Hulmes, M. Theisen, F. Ruggiero, Unhydroxylated triple helical collagen I produced in transgenic plants provides new clues on the role of hydroxyproline in collagen folding and fibril formation, J Biol Chem 276(47) (2001) 43693-8.
[163] M. Nokelainen, H. Tu, A. Vuorela, H. Notbohm, K.I. Kivirikko, J. Myllyharju, High-level production of human type I collagen in the yeast Pichia pastoris, Yeast 18(9) (2001) 797-806.
[164] M.C. Willing, S.P. Deschenes, D.A. Scott, P.H. Byers, R.L. Slayton, S.H. Pitts, H. Arikat, E.J. Roberts, Osteogenesis imperfecta type I: molecular heterogeneity for COL1A1 null alleles of type I collagen, Am J Hum Genet 55(4) (1994) 638-47.
[165] C.C. Horgan, M. Jensen, A. Nagelkerke, J.P. St-Pierre, T. Vercauteren, M.M. Stevens, M.S. Bergholt, High-Throughput Molecular Imaging via Deep-Learning-Enabled Raman Spectroscopy, Anal Chem 93(48) (2021) 15850-15860.
[166] M. Taylor-Williams, G. Spicer, G. Bale, S.E. Bohndiek, Noninvasive hemoglobin sensing and imaging: optical tools for disease diagnosis, J Biomed Opt 27(8) (2022) 080901.

[167] S. Ngarize, H. Herman, A. Adams, N. Howell, Comparison of changes in the secondary structure of unheated, heated, and high-pressure-treated beta-lactoglobulin and ovalbumin proteins using fourier transform raman spectroscopy and self-deconvolution, J Agric Food Chem 52(21) (2004) 6470-7.
[168] J.T. Pelton, L.R. McLean, Spectroscopic methods for analysis of protein secondary structure, Anal Biochem 277(2) (2000) 167-76.
[169] J. Holcomb, N. Spellmon, Y. Zhang, M. Doughan, C. Li, Z. Yang, Protein crystallization: Eluding the bottleneck of X-ray crystallography, AIMS Biophys 4(4) (2017) 557-575.
[170] M.S. Smyth, J.H. Martin, x ray crystallography, Mol Pathol 53(1) (2000) 8-14.
[171] A.A. Yee, A. Savchenko, A. Ignachenko, J. Lukin, X. Xu, T. Skarina, E. Evdokimova, C.S. Liu, A. Semesi, V. Guido, A.M. Edwards, C.H. Arrowsmith, NMR and X-ray Crystallography, Complementary Tools in Structural Proteomics of Small Proteins, Journal of the American Chemical Society 127(47) (2005) 16512-16517.
[172] M. Weik, J.P. Colletier, Temperature-dependent macromolecular X-ray crystallography, Acta Crystallogr D Biol Crystallogr 66(Pt 4) (2010) 437-446.
[173] J.U. Izunobi, C.L. Higginbotham, Polymer Molecular Weight Analysis by 1H NMR Spectroscopy, Journal of Chemical Education 88(8) (2011) 1098-1104.
[174] N.J. Greenfield, Using circular dichroism spectra to estimate protein secondary structure, Nat Protoc 1(6) (2006) 2876-2890.
[175] G.M. Kavanagh, A.H. Clark, S.B. Ross-Murphy, Heat-Induced Gelation of Globular Proteins: 4. Gelation Kinetics of Low pH β-Lactoglobulin Gels, Langmuir 16(24) (2000) 9584-9594.
[176] L. Becker, C.E. Lu, I.A. Montes-Mojarro, S.L. Layland, S. Khalil, A. Nsair, G.P. Duffy, F. Fend, J. Marzi, K. Schenke-Layland, Raman microspectroscopy identifies fibrotic tissues in collagen-related disorders via deconvoluted collagen type I spectra, Acta Biomater (2023).
[177] G. Pezzotti, W. Zhu, H. Chikaguchi, E. Marin, F. Boschetto, T. Masumura, Y.-I. Sato, T. Nakazaki, Raman Molecular Fingerprints of Rice Nutritional Quality and the Concept of Raman Barcode, Front Nutr 8 (2021) 663569-663569.
[178] V. Kocherbitov, J. Latynis, A. Misiunas, J. Barauskas, G. Niaura, Hydration of lysozyme studied by Raman spectroscopy, J Phys Chem B 117(17) (2013) 4981-92.
[179] S. Signorelli, S. Cannistraro, A.R. Bizzarri, Structural Characterization of the Intrinsically Disordered Protein p53 Using Raman Spectroscopy, Appl Spectrosc 71(5) (2017) 823-832.
[180] S. Signorelli, S. Cannistraro, A. Bizzarri, Structural Characterization of the Intrinsically Disordered Protein p53 Using Raman Spectroscopy, Applied Spectroscopy 71 (2016) 823-832.
[181] N.C. Maiti, M.M. Apetri, M.G. Zagorski, P.R. Carey, V.E. Anderson, Raman Spectroscopic Characterization of Secondary Structure in Natively Unfolded Proteins: α-Synuclein, Journal of the American Chemical Society 126(8) (2004) 2399-2408.
[182] T. Lefèvre, M.-E. Rousseau, M. Pézolet, Protein Secondary Structure and Orientation in Silk as Revealed by Raman Spectromicroscopy, Biophysical Journal 92(8) (2007) 2885-2895.
[183] C. Gullekson, L. Lucas, K. Hewitt, L. Kreplak, Surface-sensitive Raman spectroscopy of collagen I fibrils, Biophys J 100(7) (2011) 1837-45.
[184] R. Jyothi Lakshmi, V.B. Kartha, C. Murali Krishna, R.S. JG, G. Ullas, P. Uma Devi, Tissue Raman spectroscopy for the study of radiation damage: brain irradiation of mice, Radiat Res 157(2) (2002) 175-82.

[185] E.T. Abraham, S. Oecal, M. Mörgelin, P.W.N. Schmid, J. Buchner, U. Baumann, J.M. Gebauer, Collagen's primary structure determines collagen:HSP47 complex stoichiometry, J Biol Chem 297(6) (2021) 101169.
[186] P.S. Bellaye, O. Burgy, P. Bonniaud, M. Kolb, HSP47: a potential target for fibrotic diseases and implications for therapy, Expert Opin Ther Targets 25(1) (2021) 49-62.
[187] T. Miyamura, N. Sakamoto, T. Kakugawa, H. Taniguchi, Y. Akiyama, D. Okuno, S. Moriyama, A. Hara, T. Kido, H. Ishimoto, H. Yamaguchi, T. Miyazaki, Y. Obase, Y. Ishimatsu, Y. Tanaka, H. Mukae, Small molecule inhibitor of HSP47 prevents pro-fibrotic mechanisms of fibroblasts in vitro, Biochemical and Biophysical Research Communications 530(3) (2020) 561-565.
[188] M.J.R. Ruigrok, K.E.M. El Amasi, D.J. Leeming, J.M.B. Sand, H.W. Frijlink, W.L.J. Hinrichs, P. Olinga, Silencing Heat Shock Protein 47 (HSP47) in Fibrogenic Precision-Cut Lung Slices: A Surprising Lack of Effects on Fibrogenesis?, Front Med (Lausanne) 8 (2021) 607962.
[189] C. Widmer, J.M. Gebauer, E. Brunstein, S. Rosenbaum, F. Zaucke, C. Drögemüller, T. Leeb, U. Baumann, Molecular basis for the action of the collagen-specific chaperone Hsp47/SERPINH1 and its structure-specific client recognition, Proc Natl Acad Sci U S A 109(33) (2012) 13243-7.
[190] T. Taguchi, A. Nazneen, A.A. Al-Shihri, K.A. Turkistani, M.S. Razzaque, Heat shock protein 47: a novel biomarker of phenotypically altered collagen-producing cells, Acta Histochem Cytochem 44(2) (2011) 35-41.
[191] C. Gullekson, L. Lucas, K. Hewitt, L. Kreplak, Surface-sensitive Raman spectroscopy of collagen I fibrils, Biophysical journal 100(7) (2011) 1837-1845.
[192] M.M. Alvarez, J.C. Liu, G. Trujillo-de Santiago, B.H. Cha, A. Vishwakarma, A.M. Ghaemmaghami, A. Khademhosseini, Delivery strategies to control inflammatory response: Modulating M1-M2 polarization in tissue engineering applications, J Control Release 240 (2016) 349-363.
[193] J.M. Anderson, A. Rodriguez, D.T. Chang, Foreign body reaction to biomaterials, Semin Immunol 20(2) (2008) 86-100.
[194] M. Enayati, M. Eilenberg, C. Grasl, P. Riedl, C. Kaun, B. Messner, I. Walter, R. Liska, H. Schima, J. Wojta, B.K. Podesser, H. Bergmeister, Biocompatibility Assessment of a New Biodegradable Vascular Graft via In Vitro Co-culture Approaches and In Vivo Model, Annals of Biomedical Engineering 44(11) (2016) 3319-3334.
[195] S.D. Jayasingam, M. Citartan, T.H. Thang, A.A. Mat Zin, K.C. Ang, E.S. Ch'ng, Evaluating the Polarization of Tumor-Associated Macrophages Into M1 and M2 Phenotypes in Human Cancer Tissue: Technicalities and Challenges in Routine Clinical Practice, Front Oncol 9 (2019) 1512-1521.
[196] N. Feuerer, J. Marzi, E.M. Brauchle, D.A. Carvajal Berrio, F. Billing, M. Weiss, M. Jakobi, N. Schneiderhan-Marra, C. Shipp, K. Schenke-Layland, Lipidome profiling with Raman microspectroscopy identifies macrophage response to surface topographies of implant materials, Proceedings of the National Academy of Sciences 118(52) (2021) e2113694118.
[197] S. Barr, E.W. Hill, A. Bayat, Functional biocompatibility testing of silicone breast implants and a novel classification system based on surface roughness, J Mech Behav Biomed Mater 75 (2017) 75-81.
[198] L.R. Madden, D.J. Mortisen, E.M. Sussman, S.K. Dupras, J.A. Fugate, J.L. Cuy, K.D. Hauch, M.A. Laflamme, C.E. Murry, B.D. Ratner, Proangiogenic scaffolds as

functional templates for cardiac tissue engineering, Proc Natl Acad Sci U S A 107(34) (2010) 15211-6.
[199] E. Mariani, G. Lisignoli, R.M. Borzì, L. Pulsatelli, Biomaterials: Foreign Bodies or Tuners for the Immune Response?, Int J Mol Sci 20(3) (2019) 636.
[200] R. Sridharan, A.R. Cameron, D.J. Kelly, C.J. Kearney, F.J. O'Brien, Biomaterial based modulation of macrophage polarization: a review and suggested design principles, Materials Today 18(6) (2015) 313-325.
[201] C.D. Calle-Fabregat, O. Morante-Palacios, E. Ballestar, Understanding the Relevance of DNA Methylation Changes in Immune Differentiation and Disease, Genes 11(1) (2020) 110-135.
[202] X. Yang, X. Wang, D. Liu, L. Yu, B. Xue, H. Shi, Epigenetic regulation of macrophage polarization by DNA methyltransferase 3b, Mol Endocrinol 28(4) (2014) 565-574.
[203] N. Wu, M. Yang, U. Gaur, H. Xu, Y. Yao, D. Li, Alpha-Ketoglutarate: Physiological Functions and Applications, Biomol Ther (Seoul) 24(1) (2016) 1-8.
[204] K.A. Tran, C.M. Dillingham, R. Sridharan, The role of α-ketoglutarate-dependent proteins in pluripotency acquisition and maintenance, The Journal of biological chemistry 294(14) (2019) 5408-5419.
[205] C. Morganti, M. Bonora, S. Marchi, L. Ferroni, C. Gardin, M.R. Wieckowski, C. Giorgi, P. Pinton, B. Zavan, Citrate Mediates Crosstalk between Mitochondria and the Nucleus to Promote Human Mesenchymal Stem Cell In Vitro Osteogenesis, Cells 9(4) (2020) 1034.
[206] I. Larionova, E. Kazakova, M. Patysheva, J. Kzhyshkowska, Transcriptional, Epigenetic and Metabolic Programming of Tumor-Associated Macrophages, Cancers, (2020) 1411-1452.
[207] C.R. Drifka, A.G. Loeffler, K. Mathewson, G. Mehta, A. Keikhosravi, Y. Liu, S. Lemancik, W.A. Ricke, S.M. Weber, W.J. Kao, K.W. Eliceiri, Comparison of Picrosirius Red Staining With Second Harmonic Generation Imaging for the Quantification of Clinically Relevant Collagen Fiber Features in Histopathology Samples, Journal of Histochemistry & Cytochemistry 64(9) (2016) 519-529.
[208] J.M. Horowitz, S.K. Venkatesh, R.L. Ehman, K. Jhaveri, P. Kamath, M.A. Ohliger, A.E. Samir, A.C. Silva, B. Taouli, M.S. Torbenson, M.L. Wells, B. Yeh, F.H. Miller, Evaluation of hepatic fibrosis: a review from the society of abdominal radiology disease focus panel, Abdom Radiol (NY) 42(8) (2017) 2037-2053.
[209] R.M.S. Sigrist, J. Liau, A.E. Kaffas, M.C. Chammas, J.K. Willmann, Ultrasound Elastography: Review of Techniques and Clinical Applications, Theranostics 7(5) (2017) 1303-1329.
[210] B. Handzo, J. Peters, R. Kalyanaraman, A Fingerprint in a Fingerprint: A Raman Spectral Analysis of Pharmaceutical Ingredients, Spectroscopy 37(3) (2022) 24–30,45.
[211] F.W. Kotch, I.A. Guzei, R.T. Raines, Stabilization of the collagen triple helix by O-methylation of hydroxyproline residues, Journal of the American Chemical Society 130(10) (2008) 2952-2953.
[212] J.M. Anderson, K.M. Miller, Biomaterial biocompatibility and the macrophage, Biomaterials 5(1) (1984) 5-10.
[213] J. Padmanabhan, Z.N. Maan, S.H. Kwon, R. Kosaraju, C.A. Bonham, G.C. Gurtner, In Vivo Models for the Study of Fibrosis, Advances in Wound Care 8(12) (2019) 645-654.
[214] N. Naldaiz-Gastesi, O.A. Bahri, A. López de Munain, K.J.A. McCullagh, A. Izeta, The panniculus carnosus muscle: an evolutionary enigma at the intersection of distinct research fields, J Anat 233(3) (2018) 275-88.

[215] H. Zomer, A. Trentin, Skin wound healing in humans and mice: Challenges in translational research, Journal of Dermatological Science 90 (2018) 3-12.
[216] A. Gatt, S. Agarwal, P.M. Zito, Anatomy, Fascia Layers, StatPearls, StatPearls Publishing Copyright © 2022, StatPearls Publishing LLC., Treasure Island (FL), 2022 30252294.

[217] C.W. Moore, C.L. Rice, Structural and functional anatomy of the palmaris brevis: grasping for answers, Journal of Anatomy 231(6) (2017) 939-946.
[218] D.E. Eibling, Chapter 78 - Neck Dissection, in: E.N. Myers, R.L. Carrau, D.E. Eibling, B.J. Ferguson, R.L. Ferris, G.S. Gillman, S. Golla, J.R. Grandis, B.E. Hirsch, J.T. Johnson, Y. Raz, C.A. Rosen, B.M. Schaitkin, C.H. Snyderman, E.H. Toh (Eds.), Operative Otolaryngology: Head and Neck Surgery (Second Edition), W.B. Saunders, Philadelphia, 2008, pp. 679-708.
[219] H.D. Zomer, A.G. Trentin, Skin wound healing in humans and mice: Challenges in translational research, J Dermatol Sci 90(1) (2018) 3-12.
[220] P.A. Gerber, B.A. Buhren, H. Schrumpf, B. Homey, A. Zlotnik, P. Hevezi, The top skin-associated genes: a comparative analysis of human and mouse skin transcriptomes, Biol Chem 395(6) (2014) 577-91.
[221] D.C. Doeing, J.L. Borowicz, E.T. Crockett, Gender dimorphism in differential peripheral blood leukocyte counts in mice using cardiac, tail, foot, and saphenous vein puncture methods, BMC Clin Pathol 3(1) (2003) 3-9.
[222] M. Pasparakis, I. Haase, F.O. Nestle, Mechanisms regulating skin immunity and inflammation, Nat Rev Immunol 14(5) (2014) 289-301.
[223] J. Mestas, C.C. Hughes, Of mice and not men: differences between mouse and human immunology, J Immunol 172(5) (2004) 2731-8.
[224] A. Baird, C. Deng, M.H. Eliceiri, F. Haghi, X. Dang, R. Coimbra, T.W. Costantini, B.E. Torbett, B.P. Eliceiri, Mice engrafted with human hematopoietic stem cells support a human myeloid cell inflammatory response in vivo, Wound Repair Regen 24(6) (2016) 1004-1014.
[225] D. Gay, O. Kwon, Z. Zhang, M. Spata, M.V. Plikus, P.D. Holler, M. Ito, Z. Yang, E. Treffeisen, C.D. Kim, A. Nace, X. Zhang, S. Baratono, F. Wang, D.M. Ornitz, S.E. Millar, G. Cotsarelis, Fgf9 from dermal γδ T cells induces hair follicle neogenesis after wounding, Nat Med 19(7) (2013) 916-23.
[226] A. Abdullahi, S. Amini-Nik, M.G. Jeschke, Animal models in burn research, Cell Mol Life Sci 71(17) (2014) 3241-55.
[227] T.S. Olson, K. Ley, Chemokines and chemokine receptors in leukocyte trafficking, Am J Physiol Regul Integr Comp Physiol 283(1) (2002) R7-28.
[228] R.C. Fang, T.A. Mustoe, Animal models of wound healing: utility in transgenic mice, J Biomater Sci Polym Ed 19(8) (2008) 989-1005.
[229] M. King, T. Pearson, A.A. Rossini, L.D. Shultz, D.L. Greiner, Humanized mice for the study of type 1 diabetes and beta cell function, Ann N Y Acad Sci 1150 (2008) 46-53.
[230] D.L. Greiner, M.A. Brehm, V. Hosur, D.M. Harlan, A.C. Powers, L.D. Shultz, Humanized mice for the study of type 1 and type 2 diabetes, Ann N Y Acad Sci 1245 (2011) 55-58.
[231] G. Sergiacomi, L. Pugliese, F. Ricci, R. Floris, A. Fusco, High-resolution computed tomography and magnetic resonance imaging protocols in the diagnosis of fibrotic interstitial lung disease: overview for "non-radiologists", Sarcoidosis Vasc Diffuse Lung Dis 34(4) (2017) 300-306.

[232] A. Huber, L. Ebner, J.T. Heverhagen, A. Christe, State-of-the-art imaging of liver fibrosis and cirrhosis: A comprehensive review of current applications and future perspectives, Eur J Radiol Open 2 (2015) 90-100.
[233] A. Devaraj, Imaging: how to recognise idiopathic pulmonary fibrosis, European Respiratory Review 23(132) (2014) 215-219.
[234] G. Thomas, J. van Voskuilen, H.C. Gerritsen, H.J.C.M. Sterenborg, Advances and challenges in label-free nonlinear optical imaging using two-photon excitation fluorescence and second harmonic generation for cancer research, Journal of Photochemistry and Photobiology B: Biology 141 (2014) 128-138.
[235] Q. Sun, Y. Li, S. He, C. Situ, Z. Wu, J.Y. Qu, Label-free multimodal nonlinear optical microscopy reveals fundamental insights of skeletal muscle development, Biomed Opt Express 5(1) (2013) 158-66.
[236] S. Yue, M.N. Slipchenko, J.X. Cheng, Multimodal Nonlinear Optical Microscopy, Laser Photon Rev 5(4) (2011) 496-512.
[237] L. Yang, J. Park, E.J. Chaney, J.E. Sorrells, M. Marjanovic, H. Phillips, D.R. Spillman, S.A. Boppart, Label-free multimodal nonlinear optical imaging of needle biopsy cores for intraoperative cancer diagnosis, J Biomed Opt 27(5) (2022) 056504.
[238] L. Becker, N. Janssen, S.L. Layland, T.E. Mürdter, A.T. Nies, K. Schenke-Layland, J. Marzi, Raman Imaging and Fluorescence Lifetime Imaging Microscopy for Diagnosis of Cancer State and Metabolic Monitoring, Cancers (Basel) 13(22) (2021) 5682.
[239] T.T. Le, C.W. Rehrer, T.B. Huff, M.B. Nichols, I.G. Camarillo, J.X. Cheng, Nonlinear optical imaging to evaluate the impact of obesity on mammary gland and tumor stroma, Mol Imaging 6(3) (2007) 205-11.
[240] M.R. Tomaszewski, M. Gehrung, J. Joseph, I. Quiros-Gonzalez, J.A. Disselhorst, S.E. Bohndiek, Oxygen-Enhanced and Dynamic Contrast-Enhanced Optoacoustic Tomography Provide Surrogate Biomarkers of Tumor Vascular Function, Hypoxia, and Necrosis, Cancer Research 78(20) (2018) 5980-5991.
[241] A. Huber, L. Ebner, J.T. Heverhagen, A. Christe, State-of-the-art imaging of liver fibrosis and cirrhosis: A comprehensive review of current applications and future perspectives, Eur J Radiol Open 2 (2015) 90-100.
[242] M.G. Ramírez-Elías, E.S. Kolosovas-Machuca, D. Kershenobich, C. Guzmán, G. Escobedo, F.J. González, Evaluation of liver fibrosis using Raman spectroscopy and infrared thermography: A pilot study, Photodiagnosis Photodyn Ther 19 (2017) 278-283.
[243] S.S. Nazeer, A. Saraswathy, S.J. Shenoy, R.S. Jayasree, Fluorescence spectroscopy as an efficient tool for staging the degree of liver fibrosis: an in vivo comparison with MRI, Sci Rep 8(1) (2018) 10967.
[244] O. Nabeel, IR Spectroscopy in Qualitative and Quantitative Analysis, in: E.-A. Dr. Marwa, A.-S. Dr. Khalid, S.E.-S. Dr. Ahmed (Eds.), Infrared Spectroscopy - Perspectives and Applications, IntechOpen, Rijeka, 2022, p. Ch. 3.
[245] D.A. Scott, D.E. Renaud, S. Krishnasamy, P. Meriç, N. Buduneli, S. Cetinkalp, K.-Z. Liu, Diabetes-related molecular signatures in infrared spectra of human saliva, Diabetol Metab Syndr 2 (2010) 48-48.
[246] V. Suryadevara, S.S. Nazeer, H. Sreedhar, O. Adelaja, A. Kajdacsy-Balla, V. Natarajan, M.J. Walsh, Infrared spectral microscopy as a tool to monitor lung fibrosis development in a model system, Biomed. Opt. Express 11(7) (2020) 3996-4007.

Appendices

Appendix 1

Chuan-En Lu, Ruth E Levey, Giulio Ghersi, Nathan Shueller, Simone Liebscher, Shannon L. Layland, Katja Schenke-Layland, Garry P. Duffy, Julia Marzi. Monitoring the macrophage response towards biomaterial implants using label-free imaging. Materials Today Bio Volume 21, August 2023, 100696.

Materials Today Bio 21 (2023) 100696

Contents lists available at ScienceDirect

Materials Today Bio

journal homepage: www.journals.elsevier.com/materials-today-bio

Monitoring the macrophage response towards biomaterial implants using label-free imaging

Chuan-en Lu [a], Ruth E. Levey [b], Giulio Ghersi [c,d], Nathan Schueller [a], Simone Liebscher [a], Shannon L. Layland [a], Katja Schenke-Layland [a,e,f], Garry P. Duffy [b,g], Julia Marzi [a,e,f,*]

[a] Institute of Biomedical Engineering, Department for Medical Technologies and Regenerative Medicine, Eberhard Karls University Tübingen, Tübingen, Germany
[b] Anatomy and Regenerative Medicine Institute (REMEDI), School of Medicine, University of Galway, Ireland
[c] ABIEL Srl, C/o ARCA Incubatore di Imprese, Palermo, Italy
[d] Department of Biological, Chemical and Pharmaceutical Sciences and Technologies, University of Palermo, Italy
[e] NMI Natural and Medical Sciences Institute at the University of Tübingen, Reutlingen, Germany
[f] Cluster of Excellence IFIT (EXC 2180) "Image-Guided and Functionally Instructed Tumor Therapies", Eberhard Karls University Tübingen, Tübingen, Germany
[g] Science Foundation Ireland Centre for Research in Medical Devices (CÚRAM), University of Galway, Ireland

ARTICLE INFO

Keywords:
Foreign body response
Raman imaging
Extracellular matrix
Fibrosis
Diabetes

ABSTRACT

Understanding the immune system's foreign body response (FBR) is essential when developing and validating a biomaterial. Macrophage activation and proliferation are critical events in FBR that can determine the material's biocompatibility and fate in vivo. In this study, two different macro-encapsulation pouches intended for pancreatic islet transplantation were implanted into streptozotocin-induced diabetes rat models for 15 days. Post-explantation, the fibrotic capsules were analyzed by standard immunohistochemistry as well as non-invasive Raman microspectroscopy to determine the degree of FBR induced by both materials. The potential of Raman microspectroscopy to discern different processes of FBR was investigated and it was shown that Raman microspectroscopy is capable of targeting ECM components of the fibrotic capsule as well as pro and anti-inflammatory macrophage activation states, in a molecular-sensitive and marker-independent manner. In combination with multivariate analysis, spectral shifts reflecting conformational differences in Col I were identified and allowed to discriminate fibrotic and native interstitial connective tissue fibers. Moreover, spectral signatures retrieved from nuclei demonstrated changes in methylation states of nucleic acids in M1 and M2 phenotypes, relevant as indicator for fibrosis progression. This study could successfully implement Raman microspectroscopy as complementary tool to study in vivo immune-compatibility providing insightful information of FBR of biomaterials and medical devices, post-implantation.

1. Introduction

Type 1 diabetes (T1D) is an autoimmune disease that induces the destruction of pancreatic islets, resulting in the deficiency of insulin secretion [1]. Current treatments still mainly rely on daily extraneous insulin regimens, which can negatively affect the quality of life for patients suffering from T1D and is difficult to manage proper glycemic control over an entire lifespan [2–5]. Alternative strategies such as continuous subcutaneous insulin infusion (CSII) therapy [6,7], insulin pumps in combination with real-time glucose monitoring systems [8] or partially closed-looped insulin delivery systems [9] have been developed and are in clinical use. Pancreatic islet transplantation provides a potential method to cure T1D; however, the positive therapeutic outcomes of insulin independence typically only lasts 5 years. The foreign body response (FBR) driven by immune cell infiltration can influence the ultimate therapeutic outcome of the implantable devices, including islet encapsulation devices [10–13]. FBR is an end stage process of the wound healing and pathogen removal processes, which can cause damage to a material or facilitate the immunological process to engulf an implant into a fibrotic capsule [14–16]. The fibrotic capsule can physically wall off the device and impede it from oxygen, nutrients and insulin transportation, thereby impairing the functionality and survival rate of the engrafted insulin-producing cells.

FBR drives tissue fibrosis. It is initiated by non-specific serum protein adsorption to the implant surface followed by neutrophil and monocyte recruitment [17]. Once monocytes adhere to the interface, they start

* Corresponding author. Silcherstraße 7/1, 72076, Tübingen, Germany.
E-mail address: julia.marzi@uni-tuebingen.de (J. Marzi).

https://doi.org/10.1016/j.mtbio.2023.100696
Received 2 January 2023; Received in revised form 29 May 2023; Accepted 7 June 2023
Available online xxxx

differentiating into macrophages which play a crucial role in modulation of the inflammatory reaction, ECM remodeling and wound healing [17]. Macrophages can undergo further polarization towards different stages of wound healing processes. Macrophages can differentiate to highly heterogeneous subpopulations among which pro- and anti-inflammatory phenotypes are the most relevant ones: the non-activated macrophages (M0), the classically activated macrophages which are related to proinflammatory reaction (M1) and alternatively activated macrophages which are associated with regenerative and anti-inflammatory cascades (M2) [18]. The balance between M1 and M2 macrophages is essential to tissue remodeling, the imbalance between the phenotypes can result in negative effect of scar tissues formation [19]. Domination of M1 phenotype population has been shown to be detrimental to the implantation [20]; whereas M2 macrophages can secrete factors (e.g. IL-10, RELMα, Arg-1) that support tissue remodeling and inhibit fibrosis [21]. Therefore, the therapeutic strategies for implantable devices aim to reduce the ratio of M1/M2 [20,21]. Over time, macrophages fuse into foreign body giant cells, which induce fibroblasts and myofibroblasts and to migrate to the implantation site where they secrete collagens and other ECM components finally forming a fibrotic capsule surrounding the implant [19].

FBR is typically evaluated using histological staining such as H&E and Masson's trichrome which require invasive procedures and further sectioning protocols. Moreover, most histological stains are only limited to the qualitative observation of tissue and fiber morphologies. Therefore, Raman microspectroscopy (RMS) was employed to investigate FBR at the interface between the tissues and biomaterials. RMS is a non-destructive and marker-independent analytical technique that can identify molecular information based on the interaction between the laser light and the chemical bonds in a sample [22]. Recently, our group published a study using micro-computed tomography (μCT) and RMS to investigate the fibrotic capsule caused by an implantable therapeutic reservoir on a streptozotocin (STZ)-induced diabetic animal model [23]. We demonstrated the capability of RMS to identify the presence of advanced glycation end-products (AGEs) in Collagen I (Col I) in the diabetic animals. In this study, RMS was applied to the resulting capsular areas which were induced and surrounded enveloping two biomaterial candidates for islet encapsulation in vivo, polyvinylidene fluoride (PVDF) and TPU-chronoflex, to further gain a deeper understanding of FBR in a STZ-induced diabetes model. Specifically, RMS was used to discriminate interstitial connective tissues and the fibrotic capsule via Col I spectra in combination with multivariate tools. Numerous studies categorizing tissue types via RMS have been published, especially in the field of tumor biology, cell malignancy and carcinoma identification [24,25]. However, there is little research regarding ECM content differentiation between normal tissues and fibrotic capsules with RMS. Furthermore, RMS was used to detect the differences in methylation states between M1/M2 macrophages. Recent research from our group revealed RMS with multivariate analysis could distinguish different subtypes of macrophages (M0, M1, M2a and M2c) in situ through their lipid spectra [26]. This work was supported by other studies focused on macrophage phenotypes identification via RMS [26–29]. Most of these studies conducted their measurements on in-vitro samples. This study is the first to focus on performing RMS to classify macrophages phenotypes in a more complex, three-dimensional tissue environment following medical device implantation.

2. Materials and methods

2.1. Biomaterials

Briefly, TPU-chronoflex [23] and PVDF sheets were produced by an in-house electrospinning approach with thickness of 50 μm and pore size of 2 μm. The TPU-chronoflex pouches were generated with dual layers of TPU and chronoflex sheets. The PVDF pouches were produced with dual layers of PVDF sheets (Supplementary Fig. S1A). Pouches were manufactured by using in-house laser welding techniques developed by Boston Scientific (Galway, Ireland). Empty pouches were used for implantation in this study.

2.2. Surgical procedure, implantation and explantation

The procedures of biomaterial implantation have been described previously and were shown in Supplementary Fig. S1B) [23]. Animal studies were conducted by Abiel Sr (Palermo, Italy) with the approval of the Italian Ministry of Health (Authorization No. 66/2017-PR). Six female RccHan Wistar rats (150/200 g, 12-week-old, ENVIGO) were utilized for the study. All animals were treated with 65 mg/kg STZ intravenously to induce diabetes 14 days prior to implantation. Every rat underwent anesthetization by isoflurane before and during implantation. PVDF and TPU-chronoflex pouches were implanted subcutaneously. Each rat was implanted with two pouches of the same biomaterial type on the mid-back of the rat. Each type of pouch was implanted in 3 animals. On day 15, the biomaterials with surrounding skin tissues were explanted en bloc. 4% paraformaldehyde was used to fix the tissue blocks overnight at 4 °C before paraffin embedding. The tissues were sectioned to 5 μm thick slices and placed on glass slides. Before histological staining and Raman imaging, sections were deparaffinized in 100% xylene and rehydrated with a descending ethanol row. Skin tissues from regions without implants served as internal controls.

2.3. Histological staining

2.3.1. Modified Movat pentachrome staining

Deparaffinized sections were stained with a histologic pentachrome stain. Briefly, Weigert's resorcin-fuchsin solution (Banishes Fuchsin, Waldeck GmbH, Münster, Germany plus ferric chloride, Carl Roth GmbH, Karlsruhe, Germany in 96% acetified ethanol) was applied for 30 min and washed by running tap water for 2 min. 80% ethanol solution was used for the first color differentiation. Weigert's Iron hematoxylin (Waldeck GmbH) plus ferric chloride was applied for 10 min to stain nuclei and washed by deionized water. The second differentiation was conducted by 0.5% HCl–EtOH, followed by running tap water for 10 min. The sections were treated with 3% acetic acid (Carl Roth GmbH) first and then stained with 1% alcian blue (Waldeck GmbH) followed by Brilliant crocein acid-fuchsin (Brilliant crocein y plus Acid-fuchsin, both Waldeck GmbH).1% Acetic Acid and 5% phosphorus tungstic acid (Aldrich, USA) were employed for the final differentiation. The sections were then drained with 100% ethanol several times, the collagens were stained with a saffron du gâtinais solution (Waldeck GmbH). Finally, the sections were drained in 100% ethanol several times followed by incubation in Roti-Histol (Carl Roth GmbH) before mounting in Roti-Histokitt (Carl Roth GmbH) The stained sections were imaged by utilizing a light microscope (Observer Z1, Carl Zeiss AG, Oberkochen, Germany). The fibrotic capsule thickness was examined via the measurement function in Zen 2 blue edition (Carl Zeiss AG). The measurement of capsular thickness is depicted in Supplementary Fig. S2.

2.3.2. Picrosirius red staining

Deparaffinized sections were washed with distilled water for 5 min. Nuclei were stained with Weigert's hematoxylin (Waldeck GmbH) for 8 min. The stained sections were then rinsed with running tap water for 10 min. Picrosirus red (Sirius red plus picric acid solution, Sigma Aldrich USA) solution was applied for 1 h for collagen staining. Sections were washed with 0.5% acetic acid followed by absolute ethanol. The stained sections were imaged via polarized light microscopy (Axio Observer Z1, Carl Zeiss AG). The resulting colors vary between different thicknesses of collagen fibers, which has been reported to be related to collagen fiber maturity [30,31]. Red to orange colors indicate thicker fibers; yellow to green colors illustrate thin collagen fibers. Hue, saturation, brightness (HSB) color model in the Image J (Fiji version 2.0.0) software was utilized for analysis. Settings were adapted based on parameters previously

reported [30,32]. Red and orange (red: 1–13; orange: 14–25) was determined to represent mature collagens whereas yellow and green colors indicated immature collagens (yellow: 26–52; green: 53–110) [30,31]. The area percentages of red/orange to yellow/green were quantified. Three images were acquired and analyzed for each sample.

2.4. Immunofluorescence staining

Deparaffinized sections were stained for the following proteins: mouse monoclonal *anti*-αSMA (1:500; Sigma-Aldrich, St. Louis, USA), rabbit polyclonal anti-Col I (1:500; Cedarlane, Burlington, Ca) and rabbit polyclonal anti-Col III (1:75; Acris, Herford, Germany) as described previously [23]. In addition, tissue sections were stained for macrophage surface proteins: mouse monoclonal anti-CD68 (1:50; Bio-Rad, Hercules, CA, Cat#: MCA341R), rabbit monoclonal *anti*-CCR7 (1:250; abcam, Cambridge, United Kingdom, Cat#: ab32527), and rabbit polyclonal anti-CD204 (1:200; ThermoFischer, Waltham, MA, Cat#: PA5-102519). All primary antibodies were incubated overnight at 4 °C. AlexaFluor 594 conjugated goat anti-mouse (1:250, Thermo Fisher, Waltham, MA) was applied as secondary antibody for CD68 or αSMA, and AlexaFluor 488 conjugated goat anti-rabbit (1:250; Thermo Fisher, Waltham, MA) for *anti*-CCR7, anti-CD204, anti-Col I or anti-Col III antibodies. Control slides received equivalent volumes of dilution buffer. Fluorescence images were obtained by confocal laser scanning microscopy (LSM 880, Carl Zeiss AG). The cell numbers were counted manually by using the colocalization analysis (Zen 2 Blue, Carl Zeiss AG). Colocalization analysis is conducted on a pixel-by-pixel basis, the threshold of the scattering plot of pixel intensities of each channel was set to cover the frequency of 255. Control tissue sections without primary antibodies were used to validate the IF signals. Triplicate images were selected for each sample. $CD68^+/CCR7^+$ or $CD68^+/CD204^+$ cells were indicated as M1-like or M2-like macrophages, respectively. Mean gray value (MGV) was employed to quantify the expression level of the ECM components by using ImageJ V 1.52p, which is the amount of the gray values of all pixels normalized by the number of pixels.

2.5. Raman microspectroscopy and imaging

Raman microspectroscopy (WITec alpha 300 R, Ulm, Germany) was performed at the interface of the fibrotic capsule as described previously [23]. A 63× objective (W Plan-Apochromat 63×/1.0 M27, Carl Zeiss AG) was used to image deparaffinized and hydrated tissue sections, sequential to sections subjected to IF staining. Spectral preprocessing and analysis were conducted in Project Five 5.2 (WITec GmbH). True component analysis (TCA) was applied to generate false-color coded intensity distribution heatmaps based on reference spectra of αSMA, Col I, Col III and nuclei generated in a previous study [23]. To obtain reference spectra of immune cells, Raman imaging was correlated with CD68/CCR7 or CD68/CD204 positive immunofluorescence images and spectra from co-localized pixel were extracted. Triplicate images were selected for each sample. Similar to ECM signatures, the retrieved spectra were used as reference spectra to identify macrophage polarization states via TCA. MGV was also performed to quantify the signal intensities of the specific proteins. The cell numbers were counted manually by using ImageJ V 1.52p.

2.6. Multivariate data analysis

Biological molecular information was analyzed and interpreted by principal component analysis (PCA) (The Unscrambler X, CAMO Software AS, Oslo, Norway). Col I spectra were extracted from defined regions within the fibrotic capsule and interstitial connective tissue. Spectral data from normal skin tissues were extracted as controls. PCA analysis was used to investigate the molecular fingerprints in Col I spectra based on Raman shifts between different types of tissues. Single spectra information were visualized in 2D scatter plots and averaged per animal for visualization and statistical comparison in box plots. For macrophage identification, nuclei spectra of immunofluorescence stained CCR7 positive ($CCR7^+$) cells or CD204 positive ($CD204^+$) cells were extracted and applied to non-stained fibrotic capsule Raman scans to assess the difference between M1 and M2 phenotypes. The ratio of M1 to M2 macrophages was calculated manually based on the numbers of nuclei positive for $CCR7^+$ or $CD204^+$ derived reference spectra. PCA analysis was performed of the two macrophage subsets for further biological interpretation.

2.7. Statistics

Statistical analyses were performed using Prism 9 (GraphPad, La Jolla, USA) software. Unpaired t-tests were conducted for comparison between two experimental groups. One-way parametric ANOVA tests were applied to compare fibrotic tissues and interstitial connective tissues. Significance was defined as $p < 0.05$ and indicated in the figures as $^*p < 0.05$, $^{**}p < 0.01$, $^{***}p < 0.001$, and $^{****}p < 0.0001$. N numbers were defined as biological replicates which were 3 animals per implant material and 6 (pooled TPU and PVDF data) for macrophage comparison.

3. Results

4.1. PVDF and TPU-chronoflex pouches induce different thickness of fibrotic capsule with similar collagen state

PVDF and TPU-chronoflex pouches were implanted in rats subcutaneously and explanted after 15-days followed by paraformaldehyde fixation, sectioning and paraffin embedding. The overall ECM composition within the skin tissues was visualized via Movat pentachrome staining. Epidermis and dermis were illustrated in light scarlet red. Panniculus carnosus (striated muscle) was shown in dark scarlet red; ground substance of interstitial connective tissue and the dense fibrotic capsule around the implant appeared in greenish, which display the colocalization of collagen (yellow) and proteoglycans (blue). Nuclei were stained in dark purple. Implant-free tissue extracted from back regions in the periphery of the transplants showed natural interstitial connective tissues under the panniculus carnosus (Fig. 1A). Subcutaneous tissues with the implants demonstrated a higher degree of morphological changes due to fibrotic capsule formation. Visualization of subcutaneous tissues with PVDF implantation (Fig. 1B) showed relatively thinner layers of fibrotic capsule compared to the TPU-chronoflex group (Fig. 1C). Picrosirius red stained sections showed the collagen fiber architecture when exposed to polarized light due to birefringent features of collagens (Fig. 1D). The thickness of the capsule around TPU-chronoflex was 265.3 ± 42.06 μm compared to 114.5 ± 14.62 μm in PVDF (Fig. 1E). The quantification of picrosirius colorimetry demonstrated significant difference between fibrotic capsule and interstitial connective tissue (Fig. 1F and G). Within capsule regions, the ratio of red/orange to yellow/green fibers showed no significant difference. Compared to interstitial connective tissue, contribution of red/orange fibers was higher in the capsular areas.

4.2. ECM characterization of fibrotic capsule regions

Expression and deposition of fibrosis-relevant ECM components surrounding the implant were further compared between tissue sections of PVDF and TPU-chronoflex implantation via conventional and marker-independent imaging methods. Raman scans were acquired at the interface between implant and interstitial connective tissue. TCA was first applied on the Raman scans to generate color-coded intensity distribution heat maps of the most relevant structures. (Fig. 2A). According to specific spectral signatures (Fig. 2B), PVDF and TPU-chronoflex, demonstrated distinctive Raman spectra compared to other biomolecules. Col I, Col III and elastin were localized based on reference

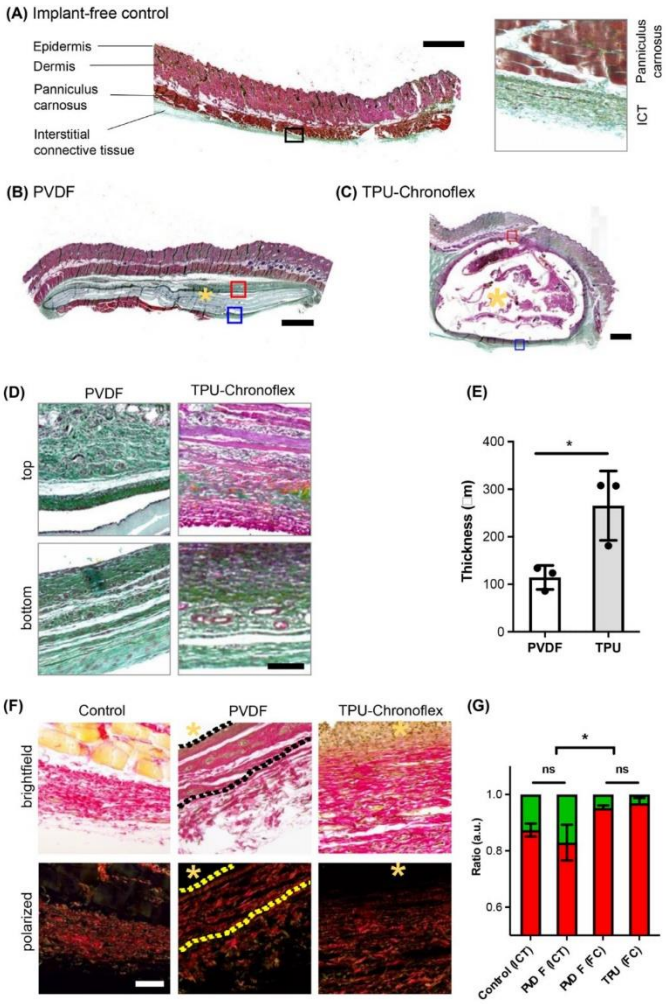

Fig. 1. Modified Movat pentachrome and picrosirius red stains visualize tissue morphology and collagen fibers of fibrotic capsules. Histological overview images of **(A)** implant-free rat skin tissues and after subcutaneous **(B)** PVDF or **(C)** TPU-chronoflex implantation. Modified Movat pentachrome; light scarlet red: Epidermis and dermis; dark scarlet red: panniculus carnosus; yellow: collagen; blue: proteoglycans. Green: colocalization of collagen (yellow) and proteoglycans (blue); yellow asterisk: implant region; scale bars equal 1 mm (left); **(D)** Selected ROIs of top and bottom regions of capsular areas for PVDF and TPU-chronoflex tissues; Scale bar equals 50 μm **(E)** Average thickness of the fibrotic capsule was determined for both implants. N = 3, *t*-test, $p^* \leq 0.05$ **(F)** Picrosirius red staining demonstrated red/orange collagen fibers and randomly distributed yellow/green fibers in the fibrotic tissues. Scale bar equals 50 μm. **(G)** The ratio of red/orange to yellow/green fibers showed significant difference between interstitial connective tissue (ICT) and fibrotic capsule (FC). Yellow asterisk: implant side. (For interpretation of the references to colour in this figure legend, the reader is referred to the Web version of this article.)

spectra obtained in a previous study [33]. The dense fibrillar collagens in the capsular area showed a parallel alignment to the implants, whereas the interstitial connective tissue region contained loosely arranged collagen fibers (Fig. 2C). These morphological observations showed correlation with SHG images (Supplementary Fig. S3). Additionally, Col I and αSMA were identified in the Raman images. Distribution of Col I and αSMA signals was more prominent in the fibrotic capsule regions compared to the interstitial connective tissue (Fig. 2C). IF staining was applied to identify Col I (green), Col III (yellow), αSMA (red), and nuclei (blue) in all tissues to validate corresponding Raman signals. (Fig. 2C). Raman scans were applied on consecutive sections without IF staining. Analogous distribution patterns of Col I and αSMA were shown in both imaging methods and confirmed the observations of histological analyses. Raman imaging was compared to IF imaging in regards of semi-quantitative analysis (Fig. 2D and E). The marker-dependent and marker independent readouts showed similar quantitative results in Col I

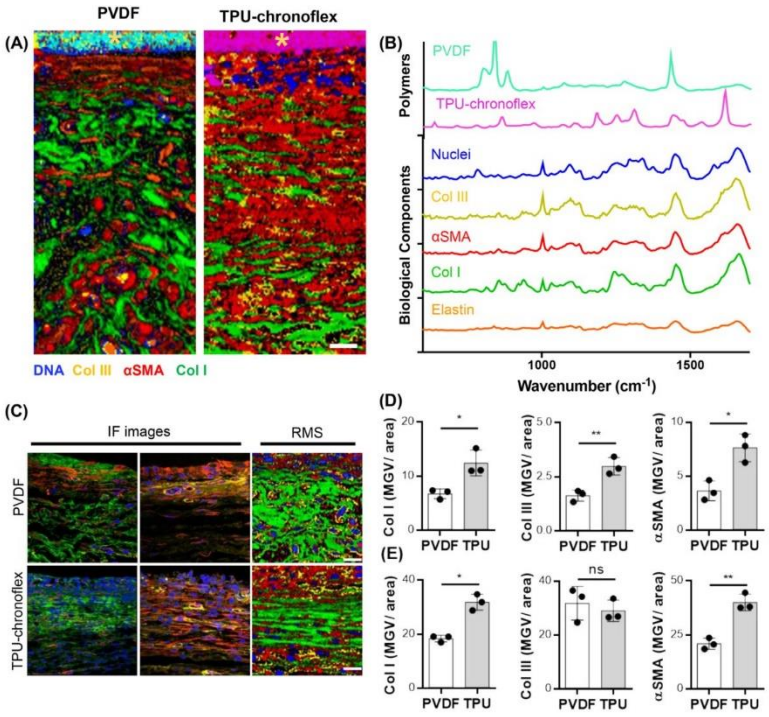

Fig. 2. Comparison of marker-dependent and independent methods for ECM characterization. (A) True component analysis (TCA) was utilized to generate intensity distribution heatmaps of the fibrotic capsule area. Scale bar equals 20 μm. **(B)** Corresponding spectra of specific components were assigned to biomaterial (light blue & pink), nuclei (blue), Col III (yellow), αSMA (red), Col I (green) and elastin (orange). **(C)** Similar trends were obtained between immunofluorescence (IF) and Raman (RMS) images of Col I (green), αSMA (red). Scale bar equals 20 μm. Implant is localized at the upper border of each image. **(D)** Quantification of ECM components and αSMA in the fibrotic capsule showed similar outputs between IF and **(E)** RMS. N = 3, *t*-test. (For interpretation of the references to colour in this figure legend, the reader is referred to the Web version of this article.)

and αSMA expression but no in Col III. In addition, no significant differences were found when comparing the ratio of Col I to Col III areas in both methods (Supplementary Fig. S3).

4.3. Discrimination of fibrotic capsule tissues and interstitial connective tissues via multivariate analysis of col I spectra

Col I morphology from the tissue surrounding the two implant types demonstrated non-identical patterns in fibrotic areas and interstitial connective tissues. In addition to marker-independent structural assignment and visualization, RMS provides molecular information of biological components reflected in spectral variations. Therefore, single Col I spectra were extracted from fibrotic and interstitial connective tissue regions to perform a PCA. Herein, the interstitial connective tissue from implant-free tissue regions of the same animals were used as a control. The PC-1/PC-3 scores plot showed two main clusters separating Col I signatures derived from interstitial connective tissues (implant-free regions and connective tissue layer below PVDF and TPU-chronoflex implants) and fibrotic capsule (the fibrotic interface adjacent to the implants) (Fig. 3A and B). PC-3 scores demonstrated significant differences between Col I extracted from the two areas. Col I spectra from interstitial connective tissues clustered at positive score ranges, whereas negative values were demonstrated for Col I from fibrotic areas (Fig. 3C). The corresponding loadings plot showed biological assignments to peaks at 1651 cm^{-1}, 1611 cm^{-1}, 1321 cm^{-1}, 1004 cm^{-1}, 856 cm^{-1} and 815 cm^{-1} (Fig. 3D), assigned to amide I, tyrosine, amide III, phenylalanine, proline and hydroxyproline. A detailed overview of the most relevant peaks and their molecular assignment is provided in Supplementary Table S1. A PCA on Col I was performed for in-depth comparison only within the fibrotic capsules and enabled to further elaborate alterations of Col I composition between PVDF and TPU-chronoflex indicated by spectral changes at 923, 972 and 1448 cm^{-1} (Supplementary Fig. S5).

4.4. Identification of M1-and M2-like macrophages via nuclei spectra

Polarization of tissue infiltrating macrophages towards a M1 (pro-inflammatory) or M2 (anti-inflammatory) phenotype can indirectly influence fibrosis severity [34]. IF stains were applied on tissue sections to identify different phenotypes of macrophages via fluorescence-guided acquisition of Raman reference spectra. In addition to pan-macrophage

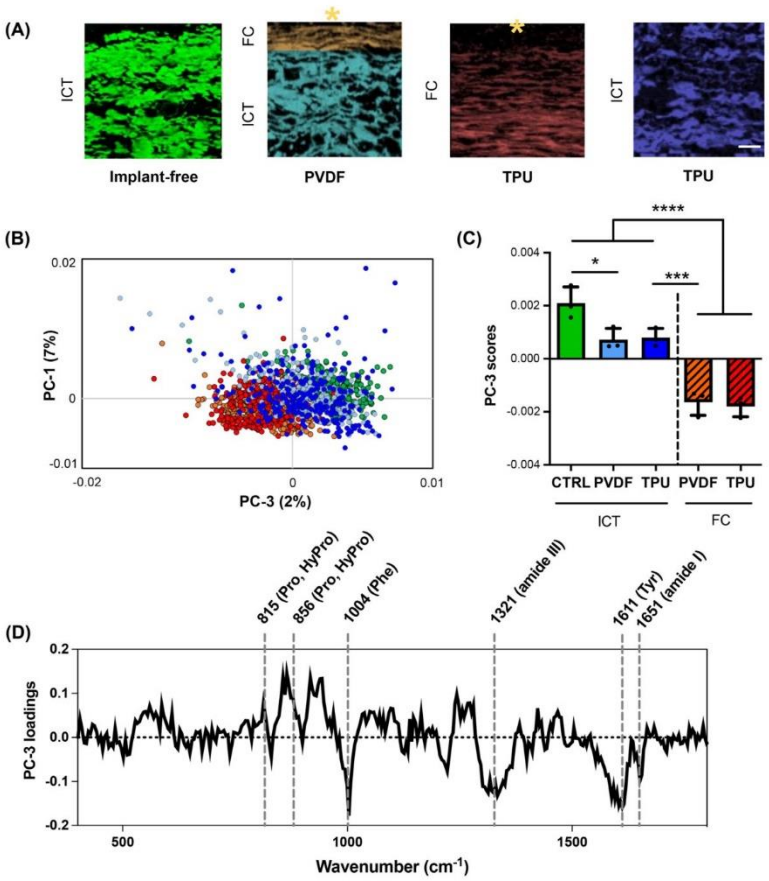

Fig. 3. Multivariate data analysis of Col I spectra differentiates molecular features between the fibrotic capsule and connective tissue. (A) Col I signals were extracted from various tissue types with or without implantation. ICT: Interstitial connective tissue; FC: fibrotic capsule scale bar equals 20 μm. **(B)** PCA scatter plot shows a separation of Col I features between fibrotic capsule and connective. **(C)** PC-3 loading scores of Col I Raman spectra can be used to differentiate fibrotic tissues and connective tissues. N = 3 per group, one-way ANOVA, p value < 0.0001. **(D)** Biological assignments that contributed to spectral differences are indicated in the PC-3 loadings plot. (Hy)Pro: (Hydroxy)Proline, Phe: Phenyl alanine, Tyr: Tyrosine.

marker CD68, tissues were stained for either CCR7 or CD204 to acquire Raman scans of single cells by fluorescence guidance (Fig. 4A). The spectra co-localized with positive surface protein signals were extracted and compared to the spectrum of DNA signals from $CCR7^{-}/CD204^{-}$ cells within the fibrotic tissue. Similar signatures with subtle variations in the peaks at 1579 cm^{-1}, 1488 cm^{-1}, 1379 cm^{-1}, 1330 cm^{-1}, 879 cm^{-1}, 857 cm^{-1} and 725 cm^{-1} could be observed among the three spectra (Fig. 4B). The identified spectra were applied as reference spectra to unstained Raman scans of PVDF and TPU-chronoflex induced fibrotic capsules and enabled the identification and localization of cellular subtypes, which showed high correlation with IF images (Fig. 4C). Based on the Raman and IF images, ratios of $CCR7^{+}$ to $CD204^{+}$ macrophages were determined. Differences in macrophage polarization were observed in fibrotic capsule tissue formed around PVDF and TPU-chronoflex. The ratio between $CCR7^{+}$ to $CD204^{+}$ cell numbers was significantly increased in FBR induced by TPU-chronoflex implantation compared to PVDF (Fig. 4D and E). Quantification based on Raman imaging was performed at similar specificity as conventional IF imaging.

4.5. Molecular-sensitive macrophage phenotyping via PCA analysis on nuclei spectra

To further investigate the biological relevance of the identified alterations in nuclei signatures of M1-like ($CCR7^{+}$) and M2-like ($CD204^{+}$)

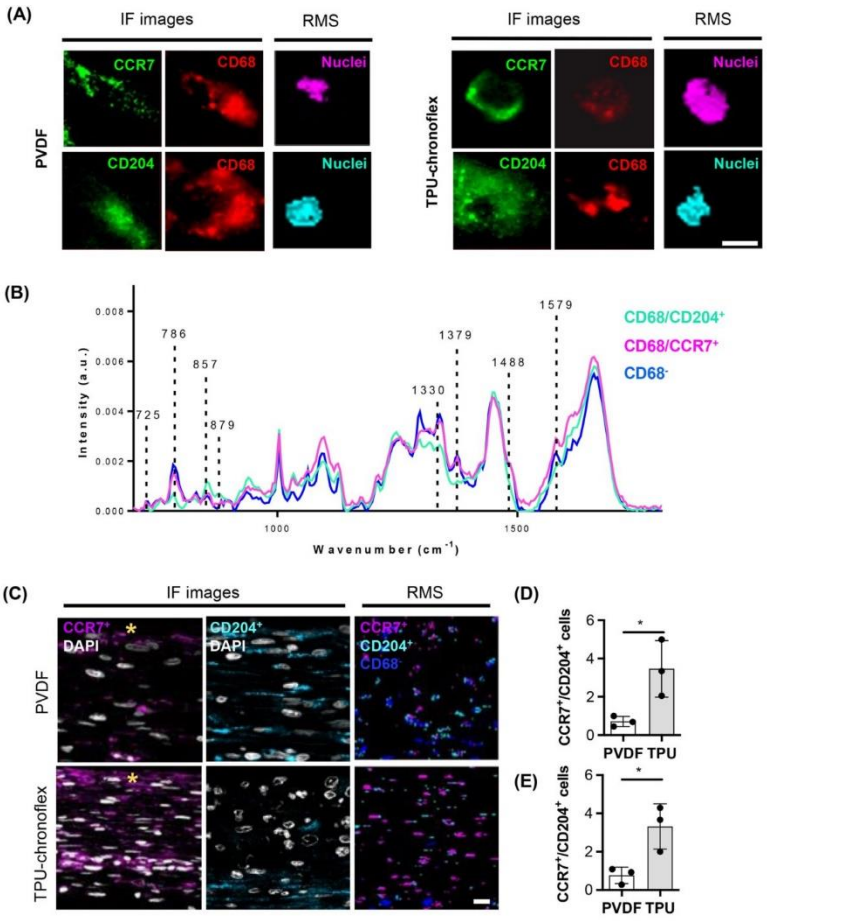

Fig. 4. Macrophage phenotyping via fluorescence-guided generation of reference spectra. (A) IF staining of $CD68^+/CCR7^+$ and $CD68^+/CD204^+$ cells in PVDF and TPU-chronoflex samples was applied to target nuclei of macrophages for correlative Raman imaging (pink & light blue). Scale bar equals 3 μm. **(B)** Average nuclei spectra extracted from $CCR7^+$ (pink) and $CD204^+$ (light blue) macrophages, compared to non-macrophage nuclei spectrum (blue). **(C)** Raman spectra were applied to the previously acquired unstained Raman scans of the fibrotic capsule for a guided TCA on cellular subtypes and compared to IF images. Scale bar equals 20 μm; yellow asterisk indicates interface to implant. The ratio of $CCR7^+$ to $CD204^+$ cell numbers was significantly different between the two implantation groups for both IF **(D)** and Raman **(E)** images. N = 3, *t*-test, $p^* < 0.05$. (For interpretation of the references to colour in this figure legend, the reader is referred to the Web version of this article.)

macrophages, spectral data from the assigned nuclei were extracted and applied for PCA to further elaborate spectral variations among the macrophage phenotypes. Two separated clusters were displayed in the PC-1 vs PC-3 scores plot (Fig. 5A). The $CCR7^+$ cell derived data clustered at negative PC-1 score ranges, whereas $CD204^+$ cell derived spectral data shifted towards positive PC-1 score values. PC-1 scores showed significant difference between nuclei spectra of M1-like and M2-like macrophages (Fig. 5B). In PC-1 loadings, difference in nuclei features were identified at increased Raman shifts for $CCR7^+$ cells at 1651 cm^{-1}, 1579 cm^{-1}, 1488 cm^{-1}, 1379 cm^{-1}, 1342 cm^{-1}, 1309 cm^{-1}, 786 cm^{-1} and 725 cm^{-1} (Fig. 5C), assigned to lipids, pyrimidine, guanine, CH_3 and CH_3/CH_2 twisting, 5-Methylcytosine and adenine (Supplementary Table S1). Nuclei spectra of $CD204^+$ macrophages showed higher intensities at the two peaks at 879 cm^{-1} and 857 cm^{-1}, corresponding hydroxyproline, proline, tryptophan and tyrosine. Statistical analysis of the most relevant loadings-derived Raman bands demonstrated significant differences in respective peak intensities of $CCR7^+$ and $CD204^+$ macrophage subsets (Fig. 5D).

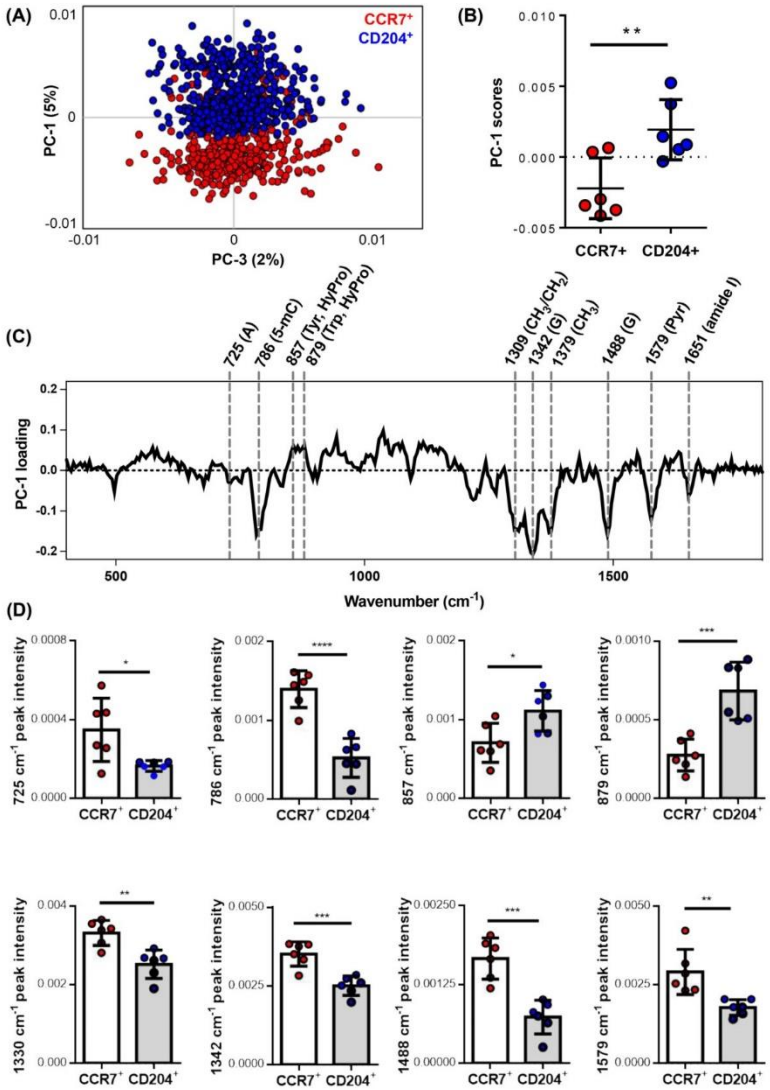

Fig. 5. Spectral peak analysis on nuclei signatures of M1-and M2-like macrophages. (A) PCA comparison demonstrates distinct separation in nuclei signals between $CCR7^+$ and $CD204^+$ macrophages. **(B)** Average PC-1 score values of nuclei spectra differed between $CCR7^+$ and $CD204^+$ cells. **(C)** Biological assignments were shown in PC-1 loading plots. A: Adenine, 5-mC: 5-methylcytosine; Pyr: Tyrosine; HyPro: Hydroxyproline; Trp: Tryptophane; G: Guanine; Pyr: Pyrimidine **(D)** Statistical analysis of relative peak intensities in Raman peaks derived from $CCR7^+$ and $CD204^+$ cells. N = 6, *t*-test, $p^*< 0.05$, $p^{**}< 0.01$, $p^{***}< 0.001$, $p^{****}<0.0001$.

5. Discussion

RMS was evaluated as a novel technique to obtain robust and faster discrimination between interstitial connective and fibrotic tissues when compared to morphological assessment of histological stains. PCA was conducted on Col I spectra and identified different biomolecular signatures for different tissue regions. Significant differences between the fibrotic and non-fibrotic tissue areas indicated secondary conformational difference in Col I. Although investigations via RMS regarding collagen conformational changes have been described in various pathological and disease states [35,36], Col I alterations between fibrotic and interstitial connective tissues have seldom been reported. In this study, Col I in the fibrotic capsule demonstrated higher spectral contributions of proline, hydroxyproline, tyrosine, phenylalanine and amide I, which might affect physical stability in its triple helical structures [37,38]. Collagen production in wound healing process highly relies on proline and hydroxyproline [39,40]. This might explain the differences at 815 cm^{-1} and 856 cm^{-1} (proline and hydroxyproline) in the Col I spectra, which showed decreased intensities in the fibrotic tissues compared to interstitial connective tissues. A recent study utilized a murine model to evaluate wound healing activity by administration of proline and hydroxyproline [41]. The results showed that proline and hydroxyproline might induce muscle regeneration with less fibrotic tissue. Though the mechanism requires more studies to be further elaborated, these differences are of great promise as potential biomarkers to identify fibrotic alterations in collagens as a proxy for immune response to implants. This finding can be expanded to further diagnostic applications. The definition of the thickness or the area of the fibrotic tissue in histological stains might cause bias between different individuals. Notably, our study highlights that fibrotic and interstitial connective tissues can be differentiated based on Raman spectrum of Col I, allowing non-biased/automated interpretation of the fibrotic regions.

Macrophages, are one of the various immune cells involved in innate and adaptive immunity [42], and play a key role in the process of FBR [43]. The interaction of macrophages and the surface of biomaterials at the initial stage of implantation has been extensively described and is highly relevant to define the biocompatibility of novel implant materials [17,43,44]. Currently, the classification of tissue-resident macrophages mainly relies on immunohistochemistry, chromogenic methods, RNA expression or flow cytometry [26,45]. To overcome limitations of these methods in regard to temporal and spatial resolution, our group recently established Raman measurements on an in vitro polarization model for monocyte-derived macrophages (MDM). Four different macrophage subsets (M0, M1 and M2a and M2c) were identified through their lipidome profiles assessed via RMS [26]. Whereas single-cell measurements in suspension provide less background noise, identification of cells in a complex tissue environment remains challenging. Not only due to the sample heterogeneity, but also due to impacts of sample processing (fixation, removal of lipids during deparaffinization) and challenging immunofluorescence-based validation of immune subsets. Multiplexing is feasible in flow cytometry based immune phenotyping of macrophage subsets but limited in conventional IF staining.

In this study, we proposed a potential approach for in situ immunophenotyping by marker-independent Raman imaging, based on fluorescence-guided generation and validation of macrophage subset reference spectra. There is a multitude of rather M1- (CD86, CCR7, CX3CR1, IL-7R, CD80, IL-1β, IL-12 and HLA-DR) or M2-like (CD163, CD204, CD206, CD209, CD369) surface markers [45,46]. In accordance to a previous study on rat tissue [47–49], CCR7 and CD204 were selected as IF markers for pro-inflammatory M1-like and anti-inflammatory M2-like) phenotypes to identify the regions of interest and acquire spectra of colocalized nuclei. These reference spectra allowed for the identification and discrimination of M1-like and M2-like phenotypes on non-processed subcutaneous tissue sections. The analyses demonstrated higher M1-like/M2-like cell number ratios for FBR induced by TPU-chronoflex than for PVDF. Lower M1-like/M2-like cell number ratio has been widely shown to indicate less severe inflammatory and fibrotic reaction to implants [18,50]. Moreover, M1-like macrophages showed higher intensities in Raman bands corresponding to the assignments of guanine, adenine, CH_3/CH_2 twisting and 5-methylcytosine (5-mC). Those peak shifts could indicate relatively higher DNA methylation state in the cells, which is consistent to our previous findings [51]. Our previous work hypothesized that Raman bands at 1257 cm^{-1}, 1331 cm^{-1}, 1342 cm^{-1} and 1579 cm^{-1} might be distinctive markers for DNA methylation. The M1-like vs M2-like loadings in this study demonstrated similar tendencies in the Raman bands corresponding to identical biological assignments, where significant differences in peak intensity were found at 1330 cm^{-1} (Twisting/wagging modes of CH_3 and CH_3CH_2 in nucleic acids), 1342 (Guanine), 1488 (Guanine) and 1579 cm^{-1} (Pyrimidine ring). The significantly increased signal at 786 cm^{-1} has been reported to represent 5-mC [51,52], which is the methylated cytosine in the DNA backbone that is mainly involved in gene transcription regulation. In fact, it has been shown that epigenetic modifications, especially DNA methylation play a role in macrophage polarization. Inhibition of DNA methyltransferase 1 (DNMT1) can promote activation of M2 macrophages, resulting in anti-inflammatory function [53,54]. The increased intensities in the peaks at 857 cm^{-1} and 879 cm^{-1} in the nuclei signature of M2 macrophages were assigned to proline, hydroxyproline, tryptophan and tyrosine (Supplementary Table S1). Proline, as one of the epigenetic modifiers, is the precursor of α-ketoglutarate [55,56]. α-Ketoglutarate is capable of entering the nucleus [57], which can be utilized as a substrate of ten-eleven translocation (TET) proteins and Jumonji C domain demethylases for DNA demethylation and histone demethylation, respectively [55,58]. The high-level of proline signals in M2-like macrophages compared to M1-like macrophages explained that the M2 phenotypes had lower methylation levels than M1 macrophages. This biological phenomenon has also been shown by other groups that α-ketoglutarate can induce anti-inflammatory response by promoting macrophage polarization into M2 macrophages and suppressing M1 macrophages activation [59,60]. Apart from using the difference in the degree of DNA methylation to discriminate M1-like/M2-like phenotypes, the peak intensity at 725 cm^{-1} has been noted to decrease in M2-like macrophages [61]. These results were consistent to the histological and Raman images, demonstrating that compared to PVDF, tissues with TPU-chronoflex implantation induced more severe FBR.

While PVDF has been widely used in the clinic as surgical meshes [62], TPUs have been applied to cardio- or vascular implants or catheters [63]. It has been reported that the inflammatory and fibrotic effects of PVDF are less severe compared to other materials [64]. This attenuated immune response might be due to the high similarity of the carbon backbone in the molecular structure of PVDF to human tissues [62,65]. TPU also has been reported to induce relatively mild FBR [66]. Nonetheless, in our study, a modified TPU-chronoflex dual-layer pouch was applied as a candidate delivery system for islet encapsulation, which has not been characterized before. The overview of the brightfield images of Movat pentachrome staining showed the fibrotic tissue caused by TPU-chronoflex was significantly thicker than by the PVDF pouch. Picrosirius red staining has been reported for the use of examination of the scar collagen states such as fiber thickness or maturation [30,67,68]. Picrosirius red staining demonstrated difference in the organization of collagen fibers between the fibrotic capsule and interstitial connective tissues. Nevertheless, the definite indication of the colorimetry in PSR staining with polarized light remains controversial and requires complementary validations. The morphological characterization of the fibrotic capsules was followed by IF staining and Raman imaging of implant-adjacent tissue regions. ECM remodeling in FBR involves immune cell recruitment, cytokine and chemokine release as well as collagen deposition [69]. Previous work by our group has shown the great potential of RMS to investigate ECM structures and biomolecules in tissue engineering [23,70,71]. Based on established reference signatures, αSMA, Col I and Col III were identified and localized in the fibrotic capsule. Quantitative evaluation of Raman imaging demonstrated the

TPU-chronoflex group had significantly higher Col I production level. The latter value might indicate an increased Col I secretion by myofibroblasts in the TPU-chronoflex group. Furthermore, the enhanced level of Col I in TPU-chronoflex group could indicate an advanced stage of fibrillogenesis compared to the PVDF group [72].

This proof-of-principle study demonstrated a potential way to evaluate the foreign body response by using RMS in combination with large database and machine learning. Current approaches for fibrotic tissues assessment in preclinical research as well as clinical diagnosis still highly rely on conventional histopathological analysis and IF staining for ECM characterization [73–75]. These examinations demand invasive tissue biopsy procedures and represent endpoint readouts. MRI, CT, SHG and ultrasound elastography provide optical examination on architectural characteristics of fibrosis [76,77]; however, these investigations are confined to morphological differences, geometrical and quantitative evaluation of collagen fibers, that mainly indicate late-stage fibrotic tissues. These advanced techniques are inadequate to monitor the progression of the fibrotic tissue formation in a molecular manner [78]. Here, RMS can be installed on an intraoperative scope to assist clinical evaluation of pathologies [79,80]. Our results and the identified spectral biomarkers for fibrotic alterations and cellular polarization encourage follow-up studies to implement label-free, non-invasive and real-time monitoring of capsular progression after implantation.

6. Conclusion

Raman imaging and microspectroscopy were shown to specifically identify and characterize FBR towards two biomaterial pouches, validated by conventional histological standards. Herein, we showed that RMS combined with multivariate analysis can provide marker-independent and molecular-sensitive methods to characterize and visualize ECM proteins in tissue samples and distinguish a fibrotic capsule from normal tissue according to compositional differences in Col I spectra. This is the first study applying RMS for M1 and M2 macrophage phenotyping in ex vivo tissues and holds great potential for the future use of clinical, non-destructive investigation of FBR.

Credit author statement

C.-E.L.: Conceptualization, Writing – original draft, Methodology, Validation, Formal analysis, Investigation, Visualization. R.E.L.: Methodology. G.G.: Methodology. N.S.: Investigation, Methodology. S.L.: Methodology. S.L.L.: Writing – review & editing. K. S.-L.: Conceptualization, Funding acquisition, Supervision, Project administration. G.P.D.: Conceptualization, Funding acquisition, Supervision, Project administration. J.M.: Conceptualization, Methodology, Supervision, Writing – review & editing.

Declaration of competing interest

The authors declare the following financial interests/personal relationships which may be considered as potential competing interests: Katja Schenke-Layland reports financial support was provided by German Research Foundation. Katja Schenke-Layland & Garry Duffy reports financial support was provided by European Union. Chuan-En Lu reports equipment, drugs, or supplies was provided by Boston Scientific Ireland Ltd. Katja Schenke-Layland reports financial support was provided by State of Baden-Wurttemberg Ministry for Science Research and Art. Giulio Ghersi reports a relationship with Abiel Sr that includes: employment.

Data availability

Data will be made available on request.

Acknowledgements

The authors want to thank Dr. Aiden Flanagan and Martin Fawdry from Boston Scientific (Galway, Ireland) for providing biomaterial pouches and Abiel Sr (Palermo, Italy) for providing rodent samples.

This study was funded by European Union's Horizon 2020, DELIVER project (grant numbers: 812865) as well as DRIVE project (grant numbers: 645991) to K.S.-L. and G.P.D., the Deutsche Forschungsgemeinschaft (INST 2388/64–1 and Germany's Excellence Strategy, EXC 2180–390900677), the Ministry of Science, Research, and the Arts of Baden-Wuerttemberg (grant numbers: 33-729.55-3/214 and SI-BW 01222–91) to K.S.-L. and the State Ministry of Baden-Wuerttemberg for Economic Affairs, Labour and Housing Construction. We acknowledge support by Open Access Publishing Fund of the University of Tübingen.

Appendix A. Supplementary data

Supplementary data to this article can be found online at https://doi.org/10.1016/j.mtbio.2023.100696.

References

[1] J.E. Campbell, C.B. Newgard, Mechanisms controlling pancreatic islet cell function in insulin secretion, Nat. Rev. Mol. Cell Biol. 22 (2) (2021) 142–158.
[2] F. Boscari, A. Avogaro, Current treatment options and challenges in patients with Type 1 diabetes: pharmacological, technical advances and future perspectives, Rev. Endocr. Metab. Disord. 22 (2) (2021) 217–240.
[3] M. Joshi, P. Choudhary, Multiple daily injections OR insulin pump therapy: choosing the best option for your patient-an evidence-based approach, Curr. Diabetes Rep. 15 (10) (2015) 81.
[4] P. Home, B. Itzhak, Is insulin therapy safe? Am. J. Therapeut. 27 (1) (2020) e106–e114.
[5] T. Takaki, M. Shimoda, Pancreatic islet transplantation: toward definitive treatment for diabetes mellitus, Glob Health Med 2 (4) (2020) 200–211.
[6] D.J. Holmes-Walker, J.E. Gunton, W. Hawthorne, M. Payk, P. Anderson, S. Donath, T. Loudovaris, G.M. Ward, T.W.H. Kay, P.J. O'Connell, Islet transplantation provides superior glycemic control with less hypoglycemia compared with continuous subcutaneous insulin infusion or multiple daily insulin injections, Transplantation 101 (6) (2017).
[7] S.A. Little, L. Leelarathna, E. Walkinshaw, H.K. Tan, O. Chapple, A. Lubina-Solomon, T.J. Chadwick, S. Barendse, D.D. Stocken, C. Brennand, S.M. Marshall, R. Wood, J. Speight, D. Kerr, D. Flanagan, S.R. Heller, M.L. Evans, J.A. Shaw, Recovery of hypoglycemia awareness in long-standing type 1 diabetes: a multicenter 2 × 2 factorial randomized controlled trial comparing insulin pump with multiple daily injections and continuous with conventional glucose self-monitoring (HypoCOMPaSS), Diabetes Care 37 (8) (2014) 2114–2122.
[8] M. Vettoretti, A. Facchinetti, Combining continuous glucose monitoring and insulin pumps to automatically tune the basal insulin infusion in diabetes therapy: a review, Biomed. Eng. Online 18 (1) (2019) 37.
[9] C.K. Boughton, A. Tripyla, S. Hartnell, A. Daly, D. Herzig, M.E. Wilinska, C. Czerlau, A. Fry, L. Bally, R. Hovorka, Fully automated closed-loop glucose control compared with standard insulin therapy in adults with type 2 diabetes requiring dialysis: an open-label, randomized crossover trial, Nat. Med. 27 (8) (2021) 1471–1476.
[10] P.O. Carlsson, D. Espes, A. Sedigh, A. Rotem, B. Zimerman, H. Grinberg, T. Goldman, U. Barkai, Y. Avni, G.T. Westermark, L. Carlbom, H. Ahlström, O. Eriksson, J. Olerud, O. Korsgren, Transplantation of macroencapsulated human islets within the bioartificial pancreas βAir to patients with type 1 diabetes mellitus, Am. J. Transplant. 18 (7) (2018) 1735–1744.
[11] A.M.J. Shapiro, D. Thompson, T.W. Donner, M.D. Bellin, W. Hsueh, J. Pettus, J. Wilensky, M. Daniels, R.M. Wang, E.P. Brandon, M.S. Jaiman, E.J. Kroon, K.A. D'Amour, H.L. Foyt, Insulin expression and C-peptide in type 1 diabetes subjects implanted with stem cell-derived pancreatic endoderm cells in an encapsulation device, Cell Reports Medicine 2 (12) (2021), 100466.
[12] R.R. Henry, J.H. Pettus, J. Wilensky, A.M.J. Shapiro, P.A. Senior, B.O. Roep, R.S. Wang, E.J. Kroon, M.J. Scott, K.A. d Amour, H.L. Foyt, Initial clinical evaluation of VC-01TM combination produc" A stem CelŒ derived islet replacement for type 1 diabetes (T1D), Diabetes 67 (Supplement_1) (2018) 138-OR.
[13] A.R. Pepper, R. Pawlick, B. Gala-Lopez, A. MacGillivary, D.M. Mazzuca, D.J. White, P.M. Toleikis, A.M. Shapiro, Diabetes is reversed in a murine model by marginal mass syngeneic islet transplantation using a subcutaneous cell pouch device, Transplantation 99 (11) (2015) 2294–2300.
[14] A. Carnicer-Lombarte, S.-T. Chen, G.G. Malliaras, D.G. Barone, Foreign body reaction to implanted biomaterials and its impact in nerve neuroprosthetics, Front. Bioeng. Biotechnol. 9 (2021) 622524, 622524.
[15] B.N. Brown, B.D. Ratner, S.B. Goodman, S. Amar, S.F. Badylak, Macrophage polarization: an opportunity for improved outcomes in biomaterials and regenerative medicine, Biomaterials 33 (15) (2012) 3792–3802.

[16] M. Hesketh, K.B. Sahin, Z.E. West, R.Z. Murray, Macrophage phenotypes regulate scar formation and chronic wound healing, Int. J. Mol. Sci. 18 (7) (2017).
[17] A. Carnicer-Lombarte, S.-T. Chen, G.G. Malliaras, D.G. Barone, Foreign body reaction to implanted biomaterials and its impact in nerve neuroprosthetics, Front. Bioeng. Biotechnol. 9 (2021).
[18] S. Barr, E.W. Hill, A. Bayat, Functional biocompatibility testing of silicone breast implants and a novel classification system based on surface roughness, J. Mech. Behav. Biomed. Mater. 75 (2017) 75–81.
[19] Y. Kim, E. Chen, W. Liu, Biomolecular strategies to modulate the macrophage response to implanted materials, J. Mater. Chem. B 4 (2015).
[20] M.T. Wolf, C.L. Dearth, C.A. Ranallo, S.T. LoPresti, L.E. Carey, K.A. Daly, B.N. Brown, S.F. Badylak, Macrophage polarization in response to ECM coated polypropylene mesh, Biomaterials 35 (25) (2014) 6838–6849.
[21] B.N. Brown, B.D. Ratner, S.B. Goodman, S. Amar, S.F. Badylak, Macrophage polarization: an opportunity for improved outcomes in biomaterials and regenerative medicine, Biomaterials 33 (15) (2012) 3792–3802.
[22] K. Sugiyama, J. Marzi, J. Alber, E.M. Brauchle, M. Ando, Y. Yamashiro, B. Ramkhelawon, K. Schenke-Layland, H. Yanagisawa, Raman microspectroscopy and Raman imaging reveal biomarkers specific for thoracic aortic aneurysms, Cell Rep Med 2 (5) (2021) 100261, 100261.
[23] R. Beatty, C.E. Lu, J. Marzi, R.E. Levey, D. Carvajal Berrio, G. Lattanzi, R. Wylie, R. O'Connor, E. Wallace, G. Ghersi, M. Salamone, E.B. Dolan, S.L. Layland, K. Schenke-Layland, G.P. Duffy, The foreign body response to an implantable therapeutic reservoir in a diabetic rodent model, Tissue Eng. C Methods 27 (10) (2021) 515–528.
[24] A. Pavićević, S. Glumac, J. Sopta, A. Popović-Bijelić, M. Mojović, G. Bačić, Raman microspectroscopy as a biomarking tool for in vitro diagnosis of cancer: a feasibility study, Croat. Med. J. 53 (6) (2012) 551–557.
[25] L. Becker, N. Janssen, S.L. Layland, T.E. Mürdter, A.T. Nies, K. Schenke-Layland, J. Marzi, Raman imaging and fluorescence lifetime imaging microscopy for diagnosis of cancer state and metabolic monitoring, Cancers 13 (22) (2021).
[26] N. Feuerer, J. Marzi, E.M. Brauchle, D.A. Carvajal Berrio, F. Billing, M. Weiss, M. Jakobi, N. Schneiderhan-Marra, C. Shipp, K. Schenke-Layland, Lipidome profiling with Raman microspectroscopy identifies macrophage response to surface topographies of implant materials, Proc. Natl. Acad. Sci. USA 118 (52) (2021), e2113694118.
[27] N. Pavillon, A.J. Hobro, S. Akira, N.I. Smith, Noninvasive detection of macrophage activation with single-cell resolution through machine learning, Proc. Natl. Acad. Sci. USA 115 (12) (2018) E2676.
[28] F.R. Bertani, P. Mozetic, M. Fioramonti, M. Iuliani, G. Ribelli, F. Pantano, D. Santini, G. Tonini, M. Trombetta, L. Businaro, S. Selci, A. Rainer, Classification of M1/M2-polarized human macrophages by label-free hyperspectral reflectance confocal microscopy and multivariate analysis, Sci. Rep. 7 (1) (2017) 8965.
[29] C. Stiebing, L. Schmölz, M. Wallert, C. Matthäus, S. Lorkowski, J. Popp, Raman imaging of macrophages incubated with triglyceride-enriched oxLDL visualizes translocation of lipids between endocytic vesicles and lipid droplets, J. Lipid Res. 58 (5) (2017) 876–883.
[30] L. Rich, P. Whittaker, Collagen and Picrosirius Red Staining: a polarized light assessment of fibrillar hue and spatial distribution, J. morphol. Sci 22 (2005) 97–104.
[31] J. Liu, M.-y. Xu, J. Wu, H. Zhang, L. Yang, D.-x. Lun, Y.-c. Hu, B. Liu, Picrosirius-polarization method for collagen fiber detection in tendons: a mini-review, Orthop. Surg. 13 (3) (2021) 701–707.
[32] D.A. MacKenna, J.H. Omens, A.D. McCulloch, J.W. Covell, Contribution of collagen matrix to passive left ventricular mechanics in isolated rat hearts, Am. J. Physiol. Heart Circ. Physiol. 266 (3) (1994) H1007–H1018.
[33] K. Sugiyama, J. Marzi, J. Alber, E.M. Brauchle, M. Ando, Y. Yamashiro, B. Ramkhelawon, K. Schenke-Layland, H. Yanagisawa, Raman microspectroscopy and Raman imaging reveal biomarkers specific for thoracic aortic aneurysms, Cell Rep Med 2 (5) (2021), 100261.
[34] T.T. Braga, J.S.H. Agudelo, N.O.S. Camara, Macrophages during the fibrotic process: M2 as friend and foe, Front. Immunol. 6 (2015) 602, 602.
[35] H. Ye, Rahul, U. Kruger, T. Wang, S. Shi, J. Norfleet, S. De, Burn-related collagen conformational changes in ex vivo porcine skin using Raman spectroscopy, Sci. Rep. 9 (1) (2019), 19138.
[36] S. Sigurdsson, P.A. Philipsen, L.K. Hansen, J. Larsen, M. Gniadecka, H.C. Wulf, Detection of skin cancer by classification of Raman spectra, IEEE Trans. Biomed. Eng. 51 (10) (2004) 1784–1793.
[37] A. Terzi, E. Storelli, S. Bettini, T. Sibillano, D. Altamura, L. Salvatore, M. Madaghiele, A. Romano, D. Siliqi, M. Ladisa, L. De Caro, A. Quattrini, L. Valli, A. Sannino, C. Giannini, Effects of processing on structural, mechanical and biological properties of collagen-based substrates for regenerative medicine, Sci. Rep. 8 (1) (2018) 1429.
[38] M.D. Shoulders, R.T. Raines, Collagen structure and stability, Annu. Rev. Biochem. 78 (2009) 929–958.
[39] S.M. Morris Jr., Arginine metabolism: boundaries of our knowledge, J. Nutr. 137 (6 Suppl 2) (2007) 1602s–1609s.
[40] A. Sica, A. Mantovani, Macrophage plasticity and polarization: in vivo veritas, J. Clin. Investig. 122 (3) (2012) 787–795.
[41] S. Jimi, S. Koizumi, K. Sato, M. Miyazaki, A. Saparov, Collagen-derived dipeptide Pro-Hyp administration accelerates muscle regenerative healing accompanied by less scarring after wounding on the abdominal wall in mice, Sci. Rep. 11 (1) (2021), 18750.
[42] K.C. Navegantes, R. de Souza Gomes, P.A.T. Pereira, P.G. Czaikoski, C.H.M. Azevedo, M.C. Monteiro, Immune modulation of some autoimmune diseases: the critical role of macrophages and neutrophils in the innate and adaptive immunity, J. Transl. Med. 15 (1) (2017) 36.
[43] Z. Sheikh, P.J. Brooks, O. Barzilay, N. Fine, M. Glogauer, Macrophages, foreign body giant cells and their response to implantable biomaterials, Materials 8 (9) (2015) 5671–5701.
[44] J.M. Anderson, A. Rodriguez, D.T. Chang, Foreign body reaction to biomaterials, Semin. Immunol. 20 (2) (2008) 86–100.
[45] S.D. Jayasingam, M. Citartan, T.H. Thang, A.A. Mat Zin, K.C. Ang, E.S. Ch'ng, Evaluating the polarization of tumor-associated macrophages into M1 and M2 phenotypes in human cancer tissue: technicalities and challenges in routine clinical practice, Front. Oncol. 9 (2019) 1512.
[46] M. Soraya, M. Jean-Louis, New tools for studying macrophage polarization: application to bacterial infections, in: P. Hridayesh (Ed.), Macrophages, IntechOpen, Rijeka, 2020. Ch. 4.
[47] R. Beatty, C.-E. Lu, J. Marzi, R.E. Levey, D. Carvajal Berrio, G. Lattanzi, R. Wylie, R. O'Connor, E. Wallace, G. Ghersi, The foreign body response to an implantable therapeutic reservoir in a diabetic rodent model, Tissue Eng. C Methods 27 (10) (2021) 515–528.
[48] F.B. Coulter, R.E. Levey, S.T. Robinson, E.B. Dolan, S. Deotti, M. Monaghan, P. Dockery, B.S. Coulter, L.P. Burke, A.J. Lowery, R. Beatty, R. Paetzold, J.J. Prendergast, G. Bellavia, S. Straino, F. Cianfarani, M. Salamone, C.M. Bruno, K.M. Moerman, G. Ghersi, G.P. Duffy, E.D. O'Cearbhaill, Additive manufacturing of multi-scale porous soft tissue implants that encourage vascularization and tissue ingrowth, Advanced Healthcare Materials 10 (14) (2021), 2100229.
[49] R.E. Levey, F.B. Coulter, K.C. Scheiner, S. Deotti, S.T. Robinson, L. McDonough, T.T. Nguyen, R. Steendam, M. Canney, R. Wylie, L.P. Burke, E.B. Dolan, P. Dockery, H.M. Kelly, G. Ghersi, W.E. Hennink, R.J. Kok, E. O'Cearbhaill, G.P. Duffy, Assessing the effects of VEGF releasing microspheres on the angiogenic and foreign body response to a 3D printed silicone-based macroencapsulation device, Pharmaceutics 13 (12) (2021) 2077.
[50] L.R. Madden, D.J. Mortisen, E.M. Sussman, S.K. Dupras, J.A. Fugate, J.L. Cuy, K.D. Hauch, M.A. Laflamme, C.E. Murry, B.D. Ratner, Proangiogenic scaffolds as functional templates for cardiac tissue engineering, Proc. Natl. Acad. Sci. U. S. A. 107 (34) (2010) 15211–15216.
[51] R. Daum, E.M. Brauchle, D.A.C. Berrio, T.P. Jurkowski, K. Schenke-Layland, Non-invasive detection of DNA methylation states in carcinoma and pluripotent stem cells using Raman microspectroscopy and imaging, Sci. Rep. 9 (1) (2019) 7014.
[52] A. Barhoumi, N.J. Halas, Detecting chemically modified DNA bases using surface-enhanced Raman spectroscopy, J. Phys. Chem. Lett. 2 (24) (2011) 3118–3123.
[53] X. Wang, Q. Cao, L. Yu, H. Shi, B. Xue, H. Shi, Epigenetic regulation of macrophage polarization and inflammation by DNA methylation in obesity, JCI insight 1 (19) (2016), e87748-e87748.
[54] D. Zhou, K. Yang, L. Chen, W. Zhang, Z. Xu, J. Zuo, H. Jiang, J. Luan, Promising landscape for regulating macrophage polarization: epigenetic viewpoint, Oncotarget 8 (34) (2017) 57693–57706.
[55] E.J. Patriarca, F. Cermola, C. D'Aniello, A. Fico, O. Guardiola, D. De Cesare, G. Minchiotti, The multifaceted roles of proline in cell behavior, Front. Cell Dev. Biol. 9 (2021).
[56] J.R. Chao, K. Knight, A.L. Engel, C. Jankowski, Y. Wang, M.A. Manson, H. Gu, D. Djukovic, D. Raftery, J.B. Hurley, J. Du, Human retinal pigment epithelial cells prefer proline as a nutrient and transport metabolic intermediates to the retinal side, J. Biol. Chem. 292 (31) (2017) 12895–12905.
[57] C. Morganti, M. Bonora, S. Marchi, L. Ferroni, C. Gardin, M.R. Wieckowski, C. Giorgi, P. Pinton, B. Zavan, Citrate mediates crosstalk between mitochondria and the nucleus to promote human mesenchymal stem cell in vitro osteogenesis, Cells 9 (4) (2020) 1034.
[58] C. D'Aniello, E.J. Patriarca, J.M. Phang, G. Minchiotti, Proline metabolism in tumor growth and metastatic progression, Front. Oncol. 10 (2020).
[59] S. Liu, J. Yang, Z. Wu, The regulatory role of α-Ketoglutarate metabolism in macrophages, Mediat. Inflamm. 2021 (2021), 5577577.
[60] P.S. Liu, H. Wang, X. Li, T. Chao, T. Teav, S. Christen, G. Di Conza, W.C. Cheng, C.H. Chou, M. Vavakova, C. Muret, K. Debackere, M. Mazzone, H.D. Huang, S.M. Fendt, J. Ivanisevic, P.C. Ho, α-ketoglutarate orchestrates macrophage activation through metabolic and epigenetic reprogramming, Nat. Immunol. 18 (9) (2017) 985–994.
[61] A.R.B. Ribeiro, E.C.O. Silva, P.M.C. Araújo, S.T. Souza, E.J.d.S. Fonseca, E. Barreto, Application of Raman spectroscopy for characterization of the functional polarization of macrophages into M1 and M2 cells, Spectrochim. Acta Mol. Biomol. Spectrosc. 265 (2022), 120328.
[62] M.F. Maitz, Applications of synthetic polymers in clinical medicine, Biosurface and Biotribology 1 (3) (2015) 161–176.
[63] D. Bezuidenhout, D.F. Williams, P. Zilla, Polymeric heart valves for surgical implantation, catheter-based technologies and heart assist devices, Biomaterials 36 (2015) 6–25.
[64] H.G. Kim, S.H. Kim, T.-S. Kim, T.W. Park, R. Won, H.-D. Park, S.A. Choi, Y.W. Jung, Polyvinylidene fluoride alters inflammatory responses by activation-induced cell death in macrophages, Immune Netw 17 (6) (2017) 402–409.
[65] L.N. Dumitrescu, M. Icriverzi, A. Bonciu, A. Roşeanu, A. Moldovan, V. Dinca, In vitro effect of replicated porous polymeric nano-MicroStructured biointerfaces characteristics on macrophages behavior, Nanomaterials 11 (8) (2021).
[66] R.R. Vogels, A. Lambertz, P. Schuster, S. Jockenhoevel, N.D. Bouvy, C. Disselhorst-Klug, U.P. Neumann, U. Klinge, C.D. Klink, Biocompatibility and biomechanical analysis of elastic TPU threads as new suture material, J. Biomed. Mater. Res. B Appl. Biomater. 105 (1) (2017) 99–106.

[67] T. Wong, A. Mead, P. Khaw, Matrix metalloproteinase inhibition modulates postoperative scarring after experimental glaucoma filtration surgery, Invest. Ophthalmol. Vis. Sci. 44 (2003) 1097–1103.
[68] M.G. Monaghan, M. Holeiter, E. Brauchle, S.L. Layland, Y. Lu, A. Deb, A. Pandit, A. Nsair, K. Schenke-Layland, Exogenous miR-29B delivery through a hyaluronan-based injectable system yields functional maintenance of the infarcted myocardium, Tissue Eng. 24 (1–2) (2018) 57–67.
[69] B.N. Kharbikar, G.S. Chendke, T.A. Desai, Modulating the foreign body response of implants for diabetes treatment, Adv. Drug Deliv. Rev. 174 (2021) 87–113.
[70] E. Brauchle, J. Kasper, R. Daum, N. Schierbaum, C. Falch, A. Kirschniak, T.E. Schäffer, K. Schenke-Layland, Biomechanical and biomolecular characterization of extracellular matrix structures in human colon carcinomas, Matrix Biol. 68–69 (2018) 180–193.
[71] A.C. Biermann, J. Marzi, E. Brauchle, J.L. Wichmann, C.T. Arendt, V. Puntmann, E. Nagel, S. Abdelaziz, A.G. Winter, K.G.M. Brockbank, S. Layland, K. Schenke-Layland, U.A. Stock, Improved long-term durability of allogeneic heart valves in the orthotopic sheep model, Eur. J. Cardio. Thorac. Surg. 55 (3) (2019) 484–493.
[72] X. Liu, H. Wu, M. Byrne, S. Krane, R. Jaenisch, Type III collagen is crucial for collagen I fibrillogenesis and for normal cardiovascular development, Proc. Natl. Acad. Sci. U. S. A. 94 (5) (1997) 1852–1856.
[73] S.A. Taqi, S.A. Sami, L.B. Sami, S.A. Zaki, A review of artifacts in histopathology, J. Oral Maxillofac. Pathol. 22 (2) (2018) 279.
[74] J.E. Scott, R.A. Stockwell, On the use and abuse of the critical electrolyte concentration approach to the localization of tissue polyanions, J. Histochem. Cytochem. 15 (2) (1967) 111–113.
[75] C.R. Drifka, A.G. Loeffler, K. Mathewson, G. Mehta, A. Keikhosravi, Y. Liu, S. Lemancik, W.A. Ricke, S.M. Weber, W.J. Kao, K.W. Eliceiri, Comparison of picrosirius red staining with second harmonic generation imaging for the quantification of clinically relevant collagen fiber features in histopathology samples, J. Histochem. Cytochem. 64 (9) (2016) 519–529.
[76] J.M. Horowitz, S.K. Venkatesh, R.L. Ehman, K. Jhaveri, P. Kamath, M.A. Ohliger, A.E. Samir, A.C. Silva, B. Taouli, M.S. Torbenson, M.L. Wells, B. Yeh, F.H. Miller, Evaluation of hepatic fibrosis: a review from the society of abdominal radiology disease focus panel, Abdom Radiol (NY) 42 (8) (2017) 2037–2053.
[77] R.M.S. Sigrist, J. Liau, A.E. Kaffas, M.C. Chammas, J.K. Willmann, Ultrasound elastography: review of techniques and clinical applications, Theranostics 7 (5) (2017) 1303–1329.
[78] S.B. Montesi, P. Désogère, B.C. Fuchs, P. Caravan, Molecular imaging of fibrosis: recent advances and future directions, J. Clin. Invest. 129 (1) (2019) 24–33.
[79] G. Thomas, J. van Voskuilen, H.C. Gerritsen, H.J.C.M. Sterenborg, Advances and challenges in label-free nonlinear optical imaging using two-photon excitation fluorescence and second harmonic generation for cancer research, J. Photochem. Photobiol. B Biol. 141 (2014) 128–138.
[80] Q. Sun, Y. Li, S. He, C. Situ, Z. Wu, J.Y. Qu, Label-free multimodal nonlinear optical microscopy reveals fundamental insights of skeletal muscle development, Biomed. Opt Express 5 (1) (2013) 158–166.

Appendix 2

Lucas Becker[§], **Chuan-En Lu[§]**, Ivonne Aidee Montes-Mojarro, Suzan Khalil, Ali Nsair, Falko Fend, Julia Marzi, Katja Schenke-Layland. Raman Microspectroscopy Identifies Fibrotic Tissues in Collagen-related Disorders via Deconvoluted Collagen Type I Spectra. Acta Biomater. 2023 Mar 15; S1742-7061(23)00150-2.

ARTICLE IN PRESS
JID: ACTBIO [m5G;March 22, 2023;16:15]
Acta Biomaterialia xxx (xxxx) xxx
Contents lists available at ScienceDirect
Acta Biomaterialia
journal homepage: www.elsevier.com/locate/actbio

Full length article

Raman microspectroscopy identifies fibrotic tissues in collagen-related disorders via deconvoluted collagen type I spectra

Lucas Becker[a,b,1], Chuan-En Lu[a,1], Ivonne A. Montes-Mojarro[c], Shannon L. Layland[a], Suzan Khalil[d], Ali Nsair[d], Garry P. Duffy[e], Falko Fend[c], Julia Marzi[a,b,f], Katja Schenke-Layland[a,b,f,*]

[a] Institute of Biomedical Engineering, Department for Medical Technologies and Regenerative Medicine, Silcherstr. 7/1, Eberhard Karls University, 72076 Tübingen, Germany
[b] Cluster of Excellence iFIT (EXC 2180) "Image-Guided and Functionally Instructed Tumor Therapies", Eberhard Karls University, Tübingen, Germany
[c] Institute of Pathology and Neuropathology, University Hospital Tübingen, Tübingen, Germany
[d] Department of Medicine/Cardiology, Cardiovascular Research Laboratories, David Geffen School of Medicine at UCLA, 675 Charles E. Young Drive South, MRL 3645 Los Angeles, CA, USA
[e] Anatomy & Regenerative Medicine Institute, School of Medicine, College of Medicine, Nursing and Health Sciences, National University of Ireland Galway, H91 TK33, Galway, Ireland
[f] NMI Natural and Medical Sciences Institute at the University of Tübingen, Markwiesenstr. 55, 72770 Reutlingen, Germany

ARTICLE INFO

Article history:
Received 23 November 2022
Revised 28 February 2023
Accepted 9 March 2023
Available online xxx

Keywords:
Pathological tissue remodeling
Non-destructive imaging
Extracellular matrix
Collagen
Spectral deconvolution
Raman microspectroscopy

ABSTRACT

Fibrosis is a consequence of the pathological remodeling of extracellular matrix (ECM) structures in the connective tissue of an organ. It is often caused by chronic inflammation, which over time, progressively leads to an excess deposition of collagen type I (COL I) that replaces healthy tissue structures, in many cases leaving a stiff scar. Increasing fibrosis can lead to organ failure and death; therefore, developing methods that potentially allow real-time monitoring of early onset or progression of fibrosis are highly valuable. In this study, the ECM structures of diseased and healthy human tissue from multiple organs were investigated for the presence of fibrosis using routine histology and marker-independent Raman microspectroscopy and Raman imaging. Spectral deconvolution of COL I Raman spectra allowed the discrimination of fibrotic and non-fibrotic COL I fibers. Statistically significant differences were identified in the amide I region of the spectral subpeak at 1608 cm^{-1}, which was deemed to be representative for structural changes in COL I fibers in all examined fibrotic tissues. Raman spectroscopy-based methods in combination with this newly discovered spectroscopic biomarker potentially offer a diagnostic approach to non-invasively track and monitor the progression of fibrosis.

Statement of Significance

Current diagnosis of fibrosis still relies on histopathological examination with invasive biopsy procedures. Although, several non-invasive imaging techniques such as positron emission tomography, single-photon emission computed tomography and second harmonic generation are gradually employed in pre-clinical or clinical studies, these techniques are limited in spatial resolution and the morphological interpretation highly relies on individual experience and knowledge. In this study, we propose a non-destructive technique, Raman microspectroscopy, to discriminate fibrotic changes of collagen type I based on a molecular biomarker. The changes of the secondary structure of collagen type I can be identified by spectral deconvolution, which potentially can provide an automatic diagnosis for fibrotic tissues in the clinical applicaion.

* Correspondence author at: Institute of Biomedical Engineering, Department for Medical Technologies and Regenerative Medicine, Eberhard Karls University Tübingen, Silcherstraße 7/1, 72076 Tübingen, Germany.
E-mail address: katja.schenke-layland@uni-tuebingen.de (K. Schenke-Layland).
[1] Authors contributed equally.

1. Introduction

Fibrosis is the pathological deposition of connective tissue in an organ as a result of extracellular matrix (ECM) remodeling and the excess secretion of collagen type I (COL I). Fibrosis is often caused by chronic inflammation, which over time, progressively remodels and replaces the normal tissue, leaving a biomechanically stiff scar. Stimuli from processes like aging, cancer, autoimmune responses, infections, foreign body response due to implantation, and repetitive tissue damage can lead to chronic inflammation, which is a main driver of fibrosis [1,2]. During fibrosis progression, healthy tissue is replaced by malfunctioning, stiffening scar tissue resulting in organ dysfunction and failure. Almost every organ and tissue in the body can undergo fibrosis [1,3]. In the US, nearly 45% of deaths are highly related to fibrotic diseases [4,5].

Currently, the clinical evaluation of fibrosis mainly relies on the evaluation of tissue biopsies by gold-standard histological analyses (H&E or Masson's trichrome staining), or clinical imaging techniques such as computed tomography, magnetic resonance imaging and ultrasound elastography [6–9]. Potential serum biomarkers were identified as indicators for fibrotic diseases such as the ratio of alanine aminotransferases and aspartate aminotransferases for liver cirrhosis as well as metalloproteases for idiopathic pulmonary fibrosis [10,11]. Nevertheless, these methods mainly allow the diagnosis of late stage, established fibrotic tissues or they assess the malfunctioning organ that is affected by fibrosis, but they cannot detect the early onset or progression of fibrosis [12]. Due to this limitation, proper treatment at an early stage to reduce or slow down the progress of fibrosis is currently not possible.

The primary ECM protein in fibrotic tissues is COL I, which makes it a favorable target for diagnosis [13]. Methods to detect changes in the collagen fiber architecture have been under development for decades; however, the results are difficult to correlate due to data disparity [14,15]. Picrosirius red staining (PSR) was developed for the purpose of characterizing collagen bundles [16]. In combination with polarized microscopy, qualitative and quantitative investigation of histological sections can be conducted, providing information on the thickness and orientation of collagen fibers [17]. However, the morphological interpretation especially from routine histology or histochemistry samples relies on the clinical experience or knowledge of individual pathologists and can generate various diagnostic outcomes [18–20]. Another optical technique, second harmonic generation (SHG), has been employed for characterizing the architecture of fibrillar collagen [19–21]. SHG can offer highly specific optical signals for collagens without any contrast agents or labeling, potentially providing a promising way to conduct non-invasive fibrosis examination [21]. Nevertheless, collagen state examination by PSR and SHG is limited to fiber geometry and morphological changes in the three-dimensional fiber structure.

Over the years, non-invasive spectroscopic techniques have gained attention in diagnostic applications [22–25]. They are suitable for studying molecules based on the interplay between laser light and the dynamic state of chemical bonds [26]. Raman spectral analysis of COL I alteration has been studied for several years. Recently, our group used Raman microspectroscopy (RMS) in combination with multivariate data analysis to identify changes in the sequence of amino acids in COL I of aortic aneurysms [27]. Moreover, RMS has also been used to investigate fibrotic capsules caused by an implantable therapeutic reservoir on streptozotocin-induced rats, demonstrating the capability of RMS to discriminate the existence of advanced glycation end-products in COL I in diabetic animals [28]. RMS has further been successfully implemented for detecting changes in collagen deposition during pathological transformation. Quantification of collagen content was employed to monitor the effectiveness of chemotherapy [25,29,30], diagnosis and characterization of various types of cancer including breast [31], prostate [32], and ovarian [33] cancer, and to monitor cancer progression [22,34]. RMS holds great potential for molecularly differentiating between collagens, particularly in tissues where connective tissue is dominant and the differentiation between fibrotic and native collagen fibers is difficult using traditional diagnostic methods. Its non-invasive nature makes it a valuable alternative to invasive biopsies or other imaging modalities, offering a more accessible and convenient option for patients. In combination with multivariate analysis and classification algorithms, RMS has the potential to provide an automated diagnosis and support pathologists in challenging cases.

In this study, RMS was employed to screen pathological collagen-rich regions ex vivo including liver, colon, breast tissue, lymph nodes and myocardium. ECM compositional differences were identified. COL I spectra were extracted and underwent spectral deconvolution as well as peak-filter and image-based ratio analysis. This study highlights the potential of RMS to be an perioperative tool to decipher the molecular alterations of COL I for fibrosis detection.

2. Materials and methods

2.1. Collection of human tissues samples

Formalin-fixed paraffin-embedded (FFPE) tissues were collected from patients undergoing medically needed surgery at the University Department of General, Visceral and Transplant Surgery, University Hospital Tübingen, and the University of California, Los Angeles (UCLA). Samples were collected after informed consent was obtained. The study was approved by the local ethical committees at UCLA and the University Hospital Tübingen (IRB 177/2014B04). Various fibrotic pathologies of different anatomical regions were analyzed, including liver lobules and portal triads, colon, breast, lymph node and myocardium. Non-fibrotic tissues from respective organs served as controls. A detailed overview of selected tissue samples and how samples were obtained is provided in Table 1. Serial 10 µm cross-sections of the tissues were prepared using a microtome (MICROM HM560, Thermo Scientific, Waltham, MA, USA).

2.2. Deparaffinization

FFPE tissue sections were deparaffinized using a modified protocol where samples were subjected to a thermal treatment at 60°C for 10 minutes, followed by three sequential incubations in xylol for 10 minutes each. The samples were then incubated in a series of ethanol solutions with progressively lower concentrations.

2.3. Masson's trichrome staining

Pathologists evaluated all tissues and confirmed the positions of fibrotic areas based on routine Masson's trichrome staining. Tissue sections were stained using an automated slide stainer Tissue Tek Prisma (Sakura, Finetek, USA) following the manufacturer's protocol.

2.4. Movat's pentachrome staining

FFPE sections were deparaffinized. A modified Movat's pentachrome staining was performed as previously described [35,36].

2.5. Picrosirius red staining

Collagen maturity and directionality analyses were performed via polarized imaging of PSR. First, Weigert's hematoxylin

Table 1
Disease origin of included samples.

Tissue type	Sample 1	Sample 2	Sample 3
Liver lobules & portal triads	Control; liver segmentation Hepatocellular carcinoma and liver cirrhosis (Ishak score 6/6); liver segmentation	Control; liver segmentation Hepatocellular carcinoma and liver cirrhosis (Ishak score 6/6); hepatectomy	Control; liver segmentation Liver cirrhosis associated to biliary atresia (Ishak score 5/6); liver biopsy
Colon submucosa	Control; hemicolectomy Crohn's disease; ileocecal resection	Control; intestine resection Crohn's disease; hemicolon resection	Control; intestine resection Crohn's disease; ileocecal resection
Breast connective tissue	Control; breast reduction surgery Marked fibrocystic changes and duct ectasia of the breast; surgical breast biopsy	Control; mastectomy Sclerosing adenosis; surgical breast biopsy	Control; breast reduction surgery Extensive ductal carcinoma in situ; mastectomy
Lymph nodes	Control; tonsillectomy Nodular sclerosis classical Hodgkin lymphoma; lymph node biopsy	Control; tonsillectomy Nodular sclerosis classical Hodgkin lymphoma; lymph node biopsy	Control; tonsillectomy Nodular sclerosis classical Hodgkin lymphoma; lymphadenectomy
Myocardium	Control; orthotopic heart transplantation Dilated cardiomyopathy; orthotopic heart transplantation	Control; orthotopic heart transplantation Dilated cardiomyopathy; orthotopic heart transplantation	Control; orthotopic heart transplantation Dilated cardiomyopathy; orthotopic heart transplantation

(Waldeck) was utilized to stain the nuclei of deparaffinized sections for 8 mins and washed with tap water for 10 mins. The sections were then treated with 0.1% picrosirius red solution (Morphisto, Frankfurt/Main, Germany) for 60 min. After treatment, the tissues were washed with 0.5% acetic acid and 100% ethanol. The picrosirius red-stained sections were imaged by polarized light microscopy (Axio Observer, Carl Zeiss Microscopy GmbH, Oberkochen, Germany) at 40x magnification followed by ImageJ (Fiji version 2.0.0) processing. The images were transferred to RGB colors. To acquire the area percentages of red and orange (mature collagens), as well as yellow and green (immature collagens) signals, the thresholds were adjusted as follows: red (1-13, 230-256), orange (14-25), yellow (26-52) and green (53-110). The directionality analysis was conducted via Image J by using the plugin "Directionality". In brief, the method of Fourier components with histogram angles from -90 to 90 degrees were applied to every 32-bit images. Non-parallel fibers were expected to show a flat histogram with various direction; while fibers with similar orientation provide peaks with similar values, representing specific angles on the direction in the histogram [37]. The plugin "OrientationJ" was used to define fiber coherency. OrientationJ evaluates the local orientation of every pixel of an image by a structure-tensor approach. Coherency is calculated as the ratio between the difference and the sum of tensor eigenvalues [38]. Entire images were analyzed and similar settings were used from other literature [15].

2.6 Immunofluorescence staining

The tissue sections underwent antigen retrieval with Tris-EDTA buffer (pH 9, 0.05%) and citrate buffer (pH 6) followed by treatment of goat serum block solution (2%). Afterwards, the tissue sections were incubated overnight with the following primary antibodies: mouse IgG2a monoclonal anti-α smooth muscle actin (αSMA) ($2*10^{-3}$ g/L; Sigma-Aldrich), rabbit polyclonal anti-collagen type I (6.6*10−3 g/L; Acris, Herford, Germany). Secondary antibodies were AlexaFluor 594-conjugated goat anti-mouse (4*10−3 g/L, Thermo Fisher Scientific Life Technologies) and AlexaFluor 488-conjugated goat anti-rabbit (4*10−3 g/L; Thermo Fisher Scientific Life Technologies). Lastly, Drag5 (5 μM; BioLegend, San Diego, USA) was applied on the sections for 15 mins to stain the nuclei. The immunofluorescence (IF)-stained sections were imaged via confocal laser scanning microscopy (LSM 880, Carl Zeiss Microscopy GmbH) with a QUASAR detector. To gain the emission spectrum of the signals, an excitation wavelength of 800 nm was utilized to excite fluorochromes. Several channels representing specific wavelengths of the emission spectra with the range from 406 - 670 nm were created via Lambda stacks (9 nm intervals). Every spectral image was coupled with linear unmixing. Regions of interest were indicated by a pathologist based on pathological examination of the Masson's trichrome staining.

2.7. Raman microspectroscopy and Raman imaging

RMS measurements of tissues were performed on a customized confocal Raman microspectrometer (WITec alpha 300 R, Ulm, Germany), equipped with a 532 nm laser and a CCD camera as described before [39]. For all scans a spectrograph with a grating of 600 g/mm was chosen for spectral detection. The human tissues were deparaffinized and kept humid with PBS during the entire measurement procedure to prevent sample dehydration and burning. Raman maps were measured utilizing a 63x Apochromat water dipping objective (N.A. 1.0; Carl Zeiss Microscopy GmbH). For each tissue section, Raman maps ($n = 3$) were acquired for an area of 100 × 100 µm and at a spatial resolution of 1 µm/pixel. The laser power was set to 50 mW at an integration time of 0.05 s per spectrum for all measurements. Reference spectra of αSMA, COL I, COL III were acquired based on IF images of colon.

2.8 Spectral analysis

With the software WITec project 5 (WITec GmbH, Ulm, Germany), all Raman maps were subjected to cosmic ray removal, polynomial baseline correction, cropping to 400-3000 cm^{-1} and area intensity normalization. With True Component Analysis (TCA), Raman scans were decomposed into spectral components as described previously [40,41]. TCA is a statistical technique that involves the use of a linear combination of spectra or components to describe each pixel in an image. This allows for the separation of different spectra that may be present in the image, and the identification of the materials or substances present based on the unique spectral patterns of the components [42]. Different types of collagens (COL I, COL III, COL IV), nuclei, αSMA, and paraffin were identified as major spectral components and localized in their corresponding intensity distribution in heatmaps resulting in false color-coded Raman images. TCA was employed to eliminate localized paraffin signals from the Raman images, thereby precluding any interferences in the subsequent analyses. Based on TCA heatmaps, spectral information (600 spectra/sample) representing COL I was extracted for further in-depth analysis of the molecular composition by PCA using Unscrambler X10.5 (Camo, Norway).

2.9 Spectral deconvolution

To gain information of peak width and peak area of the substructural bands of the amide I region (1550-1720 cm^{-1}), spectral deconvolution was performed with the software WITec project 5 (WITec). Prior to deconvolution, collagen maps were extracted from

the Raman data. Collagen maps were then cropped to the amide region before normalization of the peak at 1667 cm^{-1} to 1. The fitting region was set between 1508 and 1780 cm^{-1}. The initial position of peak calculations was set to 5 wavenumbers based on the shape of the amide I region located at 1565, 1588, 1608, 1637 and 1667 cm^{-1} and information obtained from literature [43]. For spectral deconvolution, the Lorentz fitting algorithm was chosen, with a maximum number of iterations of 1000, while fitting five functions with the shape

$$y = y_0 + \frac{2A}{\pi}\frac{w}{(x - x_0)^2 + w^2} \quad (1)$$

where w describes the width and A the area of the peak. The accuracy of each fit is evaluated with adjusted R^2 values, which is calculated as,

$$R^2_{adj} = 1 - \frac{(1 - R^2)(n - 1)}{(n - k - 1)} \quad (2)$$

where n is the number of points in the data sample and k is the number of variables in the model [43,44]. Information about peak width and peak area was extracted for further analysis. Additionally, peak intensity ratios of mean collagen spectra were calculated by division of the maximum amide I peak at 1667 cm^{-1} by the intensity at 1608 cm^{-1}.

2.10 Raman image ratio analysis

To obtain information about the peak ratios of all the individual collagen spectra within one Raman map, maximum intensity filter images of collagen maps were generated with the software WITec project 5. Sum filter images were acquired at 1667±25 $cm^{-1}$and at 1608±10 cm^{-1}. Next, image ratios of both filter images were calculated before exporting them to MatLab 2019b. The resulting images contained the value of the peak ratio for each specific pixel position. Filter images were subjected to histogram analysis, in which the distribution of all ratios is represented. Ratios were then rounded to integers before mode analysis.

2.11. Data Classification

Raman spectra were classified using linear discriminant analysis from the open-source Python scikit library [45] and a simple neural network from the open-source Keras and TensorFlow API (Google Brain). The neural network used the whole spectral fingerprints of the Raman spectra for classification. Raman spectra were classified into one of the two classes: *control* and *fibrosis*. The fully connected neural network model consists of seven layers. The input layer is a dense layer with 250 hidden units and ReLU (Rectified Linear Unit) activation. The second layer is another dense layer with 1000 hidden units, while the third layer is a dropout layer with a rate of 0.75 used to prevent overfitting. The fourth layer is a dense layer with 500 hidden units, while the fifth layer is another dropout layer with a rate of 0.25. The sixth layer is a dense layer with 62 hidden units. Finally, the seventh layer is a dense layer with 2 units and softmax activation for binary classification. The activation functions used are mainly ReLU and one sigmoid function in the last layer for probabilistic output values. The optimizer used is Adam [46] with a learning rate of 0.001. With a batch size of 128, the model trained for 100 epochs and a train validation test split of 0.6, 0.2, 0.2 is applied.

2.12. Statistical analysis

Statistical comparisons were performed from a minimum of three independent controls and fibrotic patient samples per organ. Statistical analysis was performed using GraphPad Prism version 9.00 (GraphPad Software). Results are shown throughout the entire manuscript as mean ± standard deviation. All n-numbers, applied tests, and corresponding significance for each result are listed in the figure legends.

3. Results

3.1 Histological staining indicates the presence of fibrotic lesions

Fibrosis is characterized by excessive formation of connective tissue. As collagen is the main component of connective tissue, increased collagen (mainly COL I) accumulation is an indicator of fibrotic lesions. Thus, both Masson's trichrome staining and Movat's pentachrome staining are gold standards for histopathological identification of fibrosis in patient biopsies by visualization of collagen fibers. In this study, control tissues of liver hepatocytes, liver portal triads, colon, breast connective tissue, lymph nodes and myocardium were compared to fibrotic pathologies of their respective organ to identify structural and molecular fibrosis patterns in collagen fibers (Fig. 1). Details on investigated tissue samples are provided in Table S1.

Masson's trichrome staining identified major differences in collagens between control and diseased samples. Liver tissues showed hepatic lobules (Liver lob) with small amounts of collagens depicted in blue. In the vertices of the lobes (Liver pt), collagen formations surrounding the proper hepatic artery, hepatic portal vein, bile ducts, lymphatic vessels and branches of the vagus nerve were found. In contrast, cases with liver hepatocellular carcinoma (Ishak score 6) demonstrated an increased amount of collagen that formed collagen bridges between two or more portal triads. The layer of the colon submucosa located between the mucosa (tunica mucosa) and smooth muscle (tunica muscularis) was the focus of the colon sample comparison. Control tissues were compared to samples from patients suffering from Crohn's disease. The diseased sample showed a significant amount of fibrosis and swollen colon tissue when compared to controls. The control breast tissues consisted of varying amounts of fibrous and adipose tissue, and a ductal-lobular secretory system. Masson's trichrome stain identified a large amount of collagen fibers in the control and diseased tissue. Ductal carcinoma, a precancerous invasive breast lesion, were stained showing a similar extent of collagen when compared to the control. Reactive lymph nodes showed reactive follicles and connective tissue septa. Nodular sclerosis classical Hodgkin lymphoma samples were used as the diseased tissue which showed a partial effacement of the nodal architecture with presence of dense collagen bands highlighted by Masson's trichrome staining. Dilated cardiomyopathy samples were compared to control myocardium, which showed significant interstitial collagen infiltrations in the diseased samples. Movat's pentachrome staining provided further information on the composition of the tissues. In consecutive Movat's pentachrome images (Fig. 1b) nuclei and elastic fibers were stained in black, while fibrin and muscles were stained in red. Collagens and reticular fibers were stained in yellow and mucins in blue to green. Like shown with Masson's trichrome staining, Movat's pentachrome-stained samples allowed for the identification of fibrosis based on the amount of collagen. Nevertheless, both stains were unable to discriminate between the different types of collagens and were difficult to quantify due to color overlays.

3.2. Collagen fiber density and orientation differs across tissue types

To determine if collagen fiber orientation is a robust readout when differentiating between control and fibrotic tissues, polarized light images of PSR-stained tissue sections were obtained according to their birefringent characteristics. PSR images of control and fibrotic conditions of all examined tissue types were analyzed

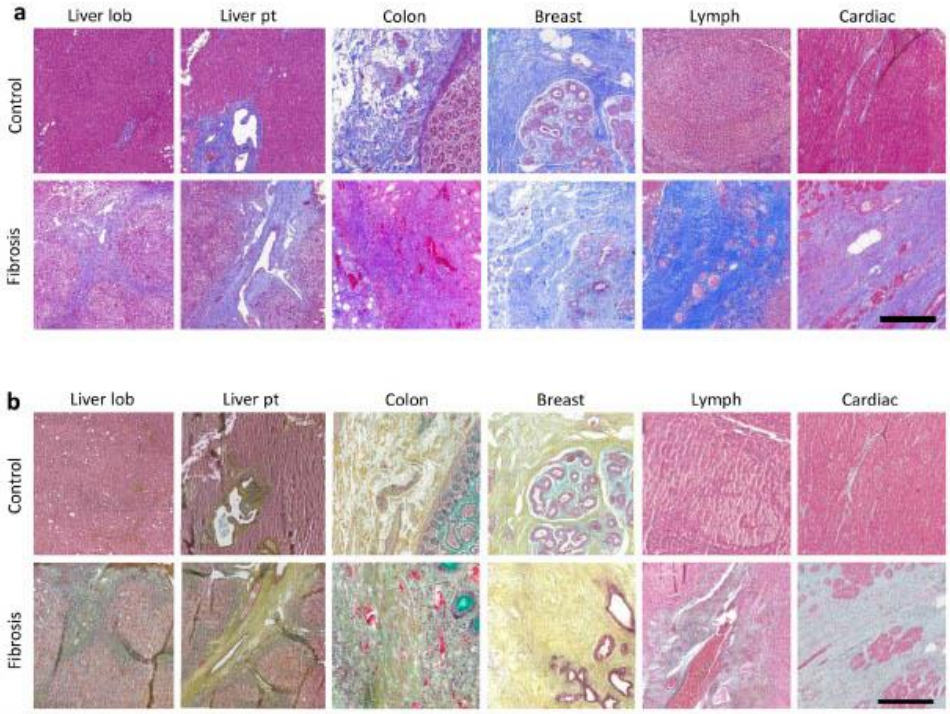

Fig. 1. Histopathology of fibrotic tissue lesions. Masson's trichrome and Movat's pentachrome staining visualize the morphology of control and fibrotic tissues. (a) Masson's trichrome staining of control and fibrotic hepatic lobules (liver lob), liver portal triads (pt), colon, as well as connective tissue of the breast, lymph nodes and myocardium. In Masson's trichrome staining, collagens are stained blue and nuclei are stained brown-black, while cytoplasm is presented in red/pink. (b) In Movat's pentachrome staining, collagens are stained in yellow, nuclei and elastic fibers in black, glycosaminoglycans in blue/green and muscles in red. Scale bars equal 500 µm. (For interpretation of the references to colour in this figure legend, the reader is referred to the web version of this article.)

(Fig. 2a). Quantification of red and green collagens revealed differences between control and fibrotic tissues; however, there was no fibrosis-specific trend observed throughout the different tissue origins (Fig. 2b). According to the calculated ratios, liver hepatocytes and liver portal triads, green collagen fibers prevailed the controls with a shift to red fibers in a fibrotic state (control liver lob: 0.72 arb. u. ± 0.03 arb. u.; fibrotic liver lob: 0.46 arb. u. ± 0.05 arb. u.; $p < 0.0001$; control liver pt: 0.21 arb. u. ± 0.18 arb. u.; fibrotic liver pt: 0.11 arb. u. ± 0.1 arb. u.; $p = 0.0471$). In breast tissue (control: 0.01 arb. u. ± 0.01 arb. u.; fibrosis: 0.07 arb. u. ± 0.10 arb. u.; $p = 0.0112$) and lymph nodes (control: 0.45 arb. u. ± 0.28 arb. u.; fibrosis: 0.81 arb. u. ± 0.06 arb. u.; $p < 0.0001$), more green collagen fibers were observed in the fibrotic state compared with the controls. In colon (control: 0.09 arb. u. ± 0.05 arb. u.; fibrosis: 0.08 arb. u. ± 0.05 arb. u.; $p = 0.4982$) and myocardium (control: 0.26 arb. u. ± 0.14 arb. u.; fibrosis: 0.29 arb. u. ± 0.03 arb. u.: $p = 0.6117$), no significant differences were found when comparing the contribution of red to green collagen fibers.

Collagen fiber alignment was assessed by histograms of fiber orientation. Histograms of collagen fiber direction in control tissues displayed an even distribution on different angles in liver hepatocytes, breast, lymph node and heart, indicating a non-aligned collagen network (Fig. 2c). In liver portal triads and colon, the histogram shifted to a parallel alignment due to naturally structured collagen fibers. In fibrotic collagens, a shift from randomly distributed orientations in controls to a more parallel alignment was found in all tissues except for breast, where most of the fibers were at a similar angle in the histograms (Fig. 2d). The quantification of fiber alignment was performed by coherency analysis indicating the overall percentage of collagens that were parallel aligned (Fig. 2e). The only statistically significant changes in coherency were found in the collagens of lymph nodes (control: 3.2% ± 0.3%; fibrosis: 11.3% ± 3.9%; $p = 0.0406$), while a similar tendency was observed in liver portal triads (control: 36.5% ± 0.2%; fibrosis: 27.8% ± 5.9%; $p = 0.4951$) and myocardium (control: 9.2% ± 3.5%; fibrosis: 17.2% ± 7.0%; $p = 0.2201$). All other tissues did not show statistically significant alterations in the degree of parallelism.

3.3. *Raman imaging enables marker-independent visualization of tissue structure states*

PSR and histological analyses were not robust enough to determine fibrotic collagen fiber alterations throughout the different tissue types and were not specific for collagen subtypes. Therefore, IF staining and marker-independent RMS were performed to identify and localize COL I and other proteins. IF staining was performed to compare and evaluate the performance of Raman imaging for the identification of distinct tissue structures as well as for the distribution of ECM components in the liver, colon, breast, lymph node and myocardium tissues. IF staining was applied to identify COL I (yellow), αSMA (red), and nuclei (blue) in all tissues (Fig. 3a).

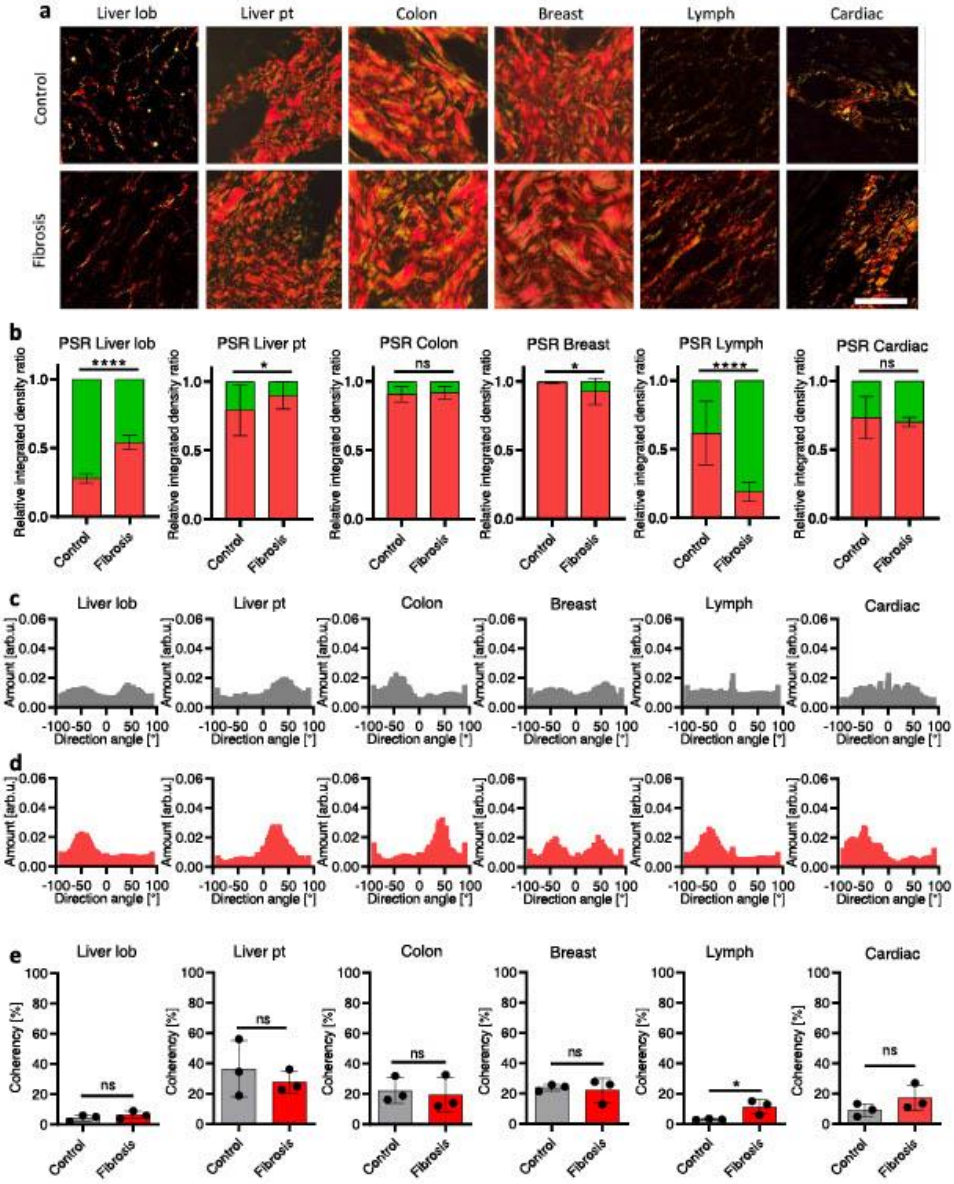

Fig. 2. Analysis of fibrillar collagens via picrosirius red staining (PSR) shows inconsistency throughout fibrotic tissue origin, (a) PSR images of control and fibrotic tissue of different organs, Scale bar equals 100 µm, (b) Quantification of mature/thick collagen (red) and immature/young collagen show inconsistency throughout all tissue origins, Directionality analysis of control collagen fibers (c) shows random distribution in the orientation of collagen fibers, In fibrotic tissues (d), the collagen fibers are more parallel aligned, Overall, the consistency is higher in the fibrosis group, (e) Coherency analysis shows statistically significant differences only in lymph node tissues, Statistical analysis: t-test, $n = 3$, $^{*}p < 0{,}05$, $^{****}p < 0{,}0005$, (For interpretation of the references to colour in this figure legend, the reader is referred to the web version of this article.)

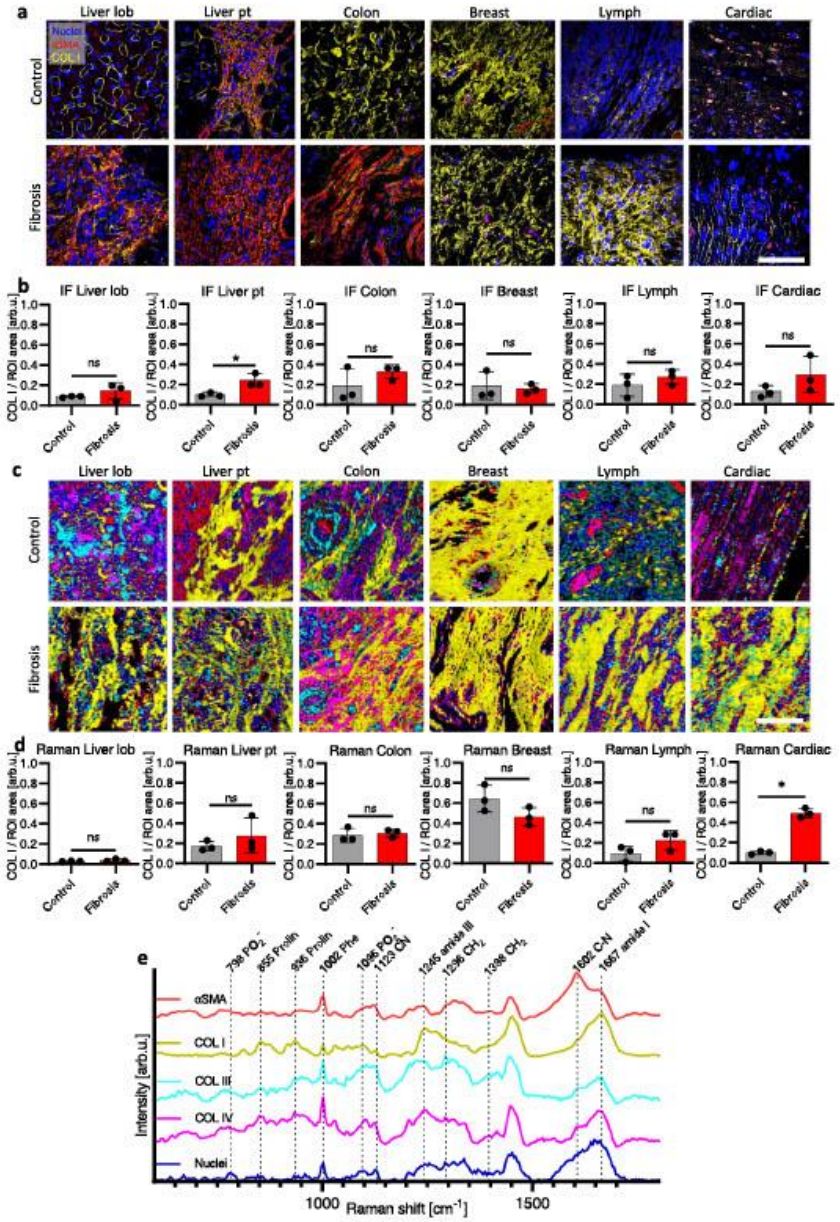

Fig. 3. Comparison of immunofluorescence (IF) staining and marker-independent true component analysis (TCA) of Raman images of control and fibrotic tissue. (a) IF staining and (c) TCA both show the complexity of the different tissue types. Colors in IF staining: nuclei (blue), COL I (yellow), αSMA (red). Scale bar equals 100 μm in IF and 50 μm in TCA images. (b) Quantification of the amount of COL I based on IF images normalized by the whole tissue area. (d) Quantification of the amount of COL I based on Raman maps normalized by the whole tissue area. (e) Spectra identified by TCA: nuclei (blue), COL IV (pink), COL III (turquoise), COL I (yellow) & αSMA (red). Statistical analysis: t-test, $n = 3$, $^*p < 0.05$. (For interpretation of the references to colour in this figure legend, the reader is referred to the web version of this article.)

Throughout tissue origins and disease stages, different COL I morphologies were observed. IF staining of control liver hepatocytes demonstrated evenly distributed COL I-composed fibers in circular shape, while in fibrosis, the amount of COL I-composed fibers was slightly increased (Fig. 3b). Apart from COL I, αSMA which is an indicator of mature myofibroblasts, also plays a vital role in ECM remodeling and fibrosis [47]. In hepatocytes, αSMA was randomly distributed in the control tissues, while being colocalized with COL I in tissues affected by fibrosis (Fig. 3a). In the portal triads of the liver, a dense network of COL I was visible in the controls, which increased significantly in fibrosis (Fig. 3b) (control: 0.10 arb. u. ± 0.01 arb. u.; fibrosis: 0.24 arb. u. ± 0.05 arb. u.; $p = 0.0246$). Both control and fibrosis samples of portal triads showed a colocalization of αSMA with COL I (Fig. 3a). In healthy colon, COL I was distributed throughout the connective tissue, while in the fibrosis samples, although still being distributed throughout the connective tissue, COL I appeared to be embedded particularly between αSMA-positive myofibroblasts. A dense network of COL I-expressing fibers was present in both control and fibrotic breast tissue with no change in the amount (Fig. 3b), whereas αSMA-expressing cells were not detected. No visible differences were identified in control breast tissue compared to fibrosis. In IF images of control lymph nodes, COL I was distributed throughout the tissue (Fig. 3a), slightly increasing in lymph nodes with classical Hodgkin Lymphoma (Fig. 3b) (control: 0.18 arb. u. ± 0.09 arb. u.; fibrosis: 0.27 arb. u. ± 0.06 arb. u.; $p = 0.2284$). Neither group showed αSMA. In control myocardium, as expected, very little COL I expression was visible, while in fibrotic myocardium an increased amount of parallel aligned COL I fibers was detected (Fig. 3a,b) (control: 0.12 arb. u. ± 0.05 arb. u.; fibrosis: 0.29 arb. u. ± 0.15 arb. u.; $p = 0.2003$). Interestingly, no αSMA staining was identified in control or fibrotic myocardium.

To characterize the tissue composition of the control and fibrotic samples non-invasively and marker-independently, Raman imaging was performed (Fig. 3c). Large area scans of the regions of interest were analyzed by TCA. The mathematical model identified five major cellular components identified in all tissue types. TCA allowed the visualization of the tissue substructures as false color-coded intensity heatmaps in which each color represented the best fit to one of the identified molecular signatures.

Evaluation of the individual peaks of the fingerprint regions of the Raman spectra (Fig. 3e) in combination with the morphology of the structures allowed the identification of correlating molecular assignments and biological origin. Nuclei (blue) were identified by pronounced peaks at 798 and 1096 cm^{-1}, indicators for PO2− occurring in DNA [48]. COL I (yellow) was assigned to the characteristic peak pair at 855 and 936 cm^{-1} indicatives for proline [49,50]. The collagen type IV (COL IV, pink) Raman spectra shared many spectral features with COL I; however, it showed an increased signal intensity at 1312 cm^{-1}, 1335 cm^{-1}, and 1398 cm^{-1}, which are representatives for CH3/CH2 twisting or wagging modes as well as changes in CH2 deformation [49–51]. Additionally, the band at 1002 cm^{-1}, which is a representative for phenylalanine (Phe), was increased in COL IV as reported before by Nguyen et al [52]. Collagen type III (COL III, turquoise) shares many spectral features with COL I; however, it differed in the amide III region by slightly shifted peaks from 1245 to 1248 cm^{-1} as previously reported [53]. Furthermore, changes in CH2 and CN were found by a band occurring at 1296 cm^{-1} and increased intensities at 1123 cm^{-1} [49,54]. Compared to COL I, the peak pair at 855 and 936 cm^{-1} dropped in intensity in all other collagen types. The spectral assignments to αSMA (red) were based on in-house Raman measurements, which had been acquired and validated by co-localization of the IF signal (Supplementary Fig. S1a). The Raman spectrum of αSMA is mainly distinguished from the Raman spectra of the different collagen types by the shape of the amide I region. In the αSMA Raman spectrum, the maximum of the amide I peak is relocated from 1667 cm^{-1} to 1602 cm^{-1}, wavenumbers which represent C-N bonds [55]. In general, TCA images showed similar morphological features as IF images, indicating the potential of Raman spectroscopy being utilized to image tissues non-invasively. Quantification of the amounts of COL I (Fig. 3d) based on Raman maps solely containing COL I information showed similar results as IF quantification. While there were no observable differences between the control and fibrotic tissues in regard to the amount of COL I in hepatocytes (control liver lob: 0.03 arb. u. ± 0.01 arb. u.; fibrotic liver lob: 0.04 arb. u. ± 0.01 arb. u.; $p = 0.3203$) or colon (control: 0.10 ± 0.06 arb. u.; fibrosis: 0.23 arb. u. ± 0.08 arb. u.: $p = 0.6993$), the portal triads of the liver showed a slight increase in fibrotic COL I (control liver pt: 0.17 arb. u. ± 0.04 arb. u.; fibrotic liver pt: 0.28 arb. u. ± 0.14 arb. u.; $p = 0.3073$). Further, and similar to the IF imaging, in fibrotic lymph nodes the amount of COL I was increased in comparison to the controls (control: 0.10 arb. u. ± 0.06 arb. u.; fibrosis: 0.23 arb. u. ± 0.08 arb. u.; $p = 0.1335$). A statistically significant increase was identified in fibrotic myocardium (control: 0.10 arb. u. ± 0.01 arb. u.; fibrosis: 0.49 arb. u. ± 0.04 arb. u.; $p = 0.0002$).

3.4. Fibrotic COL I alterations are identified by Raman analyses at wavenumber 1608 cm^{-1}

In addition to the image-based characterization of tissue patterns, in-depth analysis of the underlaying Raman spectra allowed a molecular-sensitive analysis of tissue structures. For further analysis of collagen fibers from several human tissues, COL I spectra were extracted from large area scans and processed as single or averaged spectra. These Raman spectra were cropped to the fingerprint region (600-1800 cm^{-1}) and peak normalized to 1 for better comparability (Fig. 4a). To determine the sensitivity of Raman spectroscopy to distinguish between control and fibrotic COL I, 200 single spectra per sample were analyzed by principal component analysis (PCA). Comparison of PC score values (Supplementary Fig. S1b) demonstrated trends of separation in PC-2 and PC-3, both mainly explained by shifts in loadings plots (Supplementary Fig. S1c) at the amide I region (1550-1720 cm^{-1}), containing information about the secondary structure of proteins. The secondary structures of collagens were mainly α-like helices, β-sheets, β-turns and random coils (disordered) [56,57].

In addition, LDA and neural network-based classification were utilized to classify the Raman data into one of the two groups control or fibrosis. Supplementary Table S1 shows the classification results with the performance parameters accuracy, sensitivity, and specificity for the LDA, and neural network trained with the entire RMS data. We observed that compared to LDA, the utilization of neural networks resulted in an improvement in classification performance. Specifically, LDA yielded an accuracy of 62%, a sensitivity of 60%, and a specificity of 64%, while the utilization of neural networks resulted in an accuracy of 71%, a sensitivity of 64%, and a specificity of 72%.

For a detailed analysis of the secondary structure of COL I, spectral deconvolution of the amide I peak of averaged control and fibrotic COL I Raman spectra was utilized to separate the broad band into five underlying peaks. The sub-band number and locations were chosen based on the shape of the amide I peak in averaged COL I Raman spectra (Fig. 4b) and according to literature [43]. Fig. 4c and d display the amide I region of control and fibrotic liver portal triads with underlying sub-bands calculated by spectral deconvolution. Spectral deconvolution allowed the analysis of the width and area of sub-peaks occurring at 1562 cm^{-1}, 1588 cm^{-1}, 1608 cm^{-1}, 1637 cm^{-1} and 1667 cm^{-1} which are assigned to tryptophan, phenylalanine, and tyrosine, β-sheets as well as β-turns. The adjusted R2 values were above 0.995 for all the deconvolu-

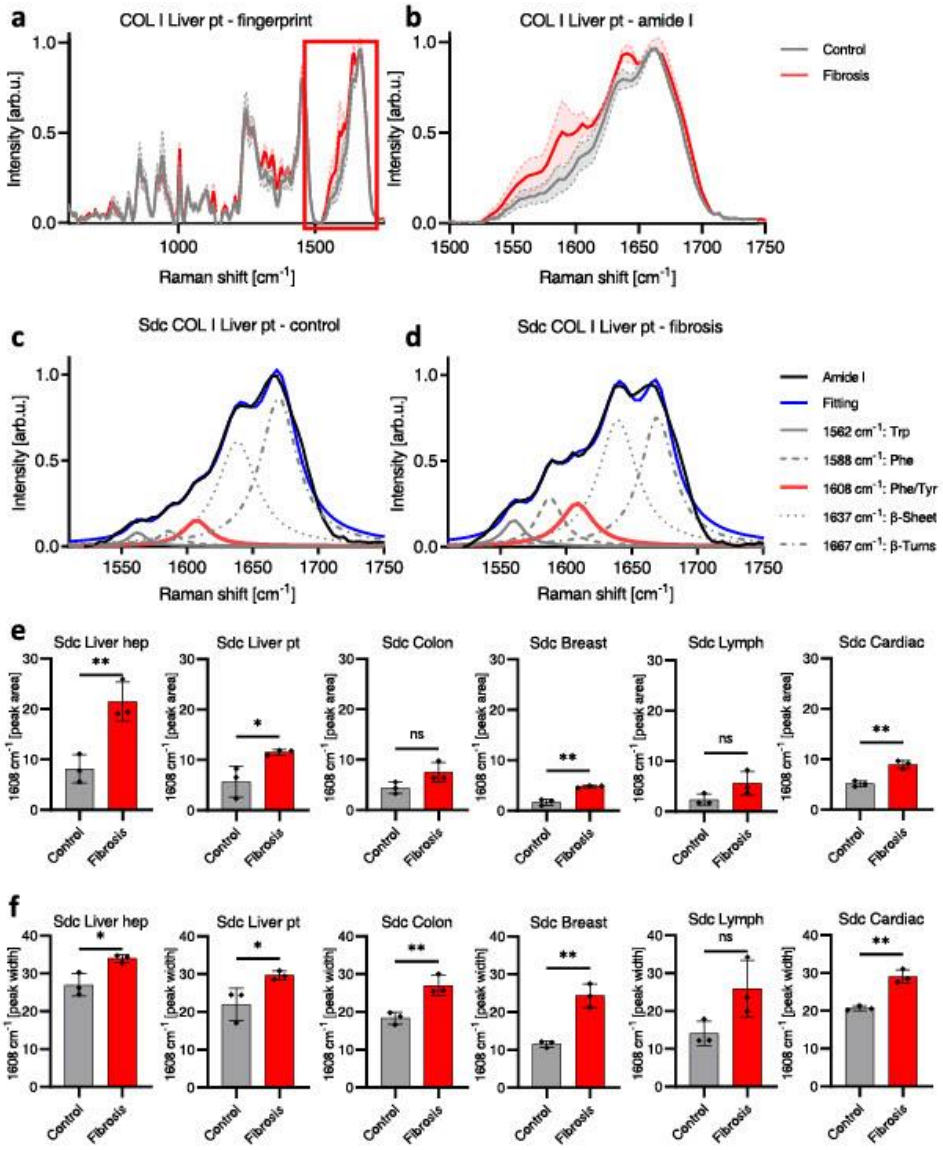

Fig. 4. Spectral deconvolution (Sdc) of the amide I region from averaged COL I Raman spectra display a similar separation between control and fibrosis through all tissue types. (a) Raman fingerprint of control and fibrotic COL I of liver portal triad, (b) Amide I region of control and fibrotic COL I of liver portal triad, The shaded error lines represent the standard deviation, Spectral deconvolution of the amide I band from (c) control and (d) fibrotic liver portal triad, The averaged amide I band is shown by a black solid line and sub-bands at 1562, 1584, 1639 as well as 1667 cm^{-1} are labeled in grey (solid line, dashed, dotted, dash-dot), while the sub-band at 1608 cm^{-1} is marked in red, The fitted amide I band is visualized by a blue solid line, (e) Peak area at 1608 cm^{-1} calculated based on spectral deconvolution of amide I area of averaged COL I spectra from control and fibrotic tissue show similar separation through all tissue types, (f) Peak width at 1608 cm^{-1} calculated based on spectral deconvolution of amide I area of averaged COL I spectra from control and fibrotic tissue show similar separation through all tissue types, Statistical analysis; t-test, $n = 3$, $^{*}p < 0{,}05$, $^{**}p < 0{,}01$, (For interpretation of the references to colour in this figure legend, the reader is referred to the web version of this article.)

tions, indicating sufficient fitting accuracy. Area and width of the subpeaks at 1588 cm^{-1}, 1608 cm^{-1} and 1637 cm^{-1} were subjected to statistical analysis. While in peak areas at 1588 cm^{-1} there was a statistically significant increase in fibrotic liver hepatocytes, this increase was inversed in breast tissue samples (Supplementary Fig. S2a). All other tissue types did not show any statistical separation between the control and fibrosis samples. Similar statistical differences were found in the peak width at 1588 cm^{-1} (Supplementary Fig. 2b). Peak analysis of the subpeak at 1637 cm^{-1} did not show any statistically significant difference in all examined tissues in both peak area (Supplementary Fig. S2c) and peak width (Supplementary Fig. S2d). However, analysis of the calculated peak area of the subpeak at 1608 cm^{-1} (Fig. 4e) showed a statistically significant increase in the liver tissues (control liver lob: 8.2 arb. u. ± 2.3 arb. u.; fibrotic liver lob: 21.5 arb. u. ± 3.2 arb. u.; $p = 0.0085$; control liver pt: 5.7 arb. u. ± 2.5 arb. u.; fibrotic liver pt: 11.5 arb. u. ± 0.4 arb. u.; $p = 0.0313$). In colon, the clear tendency of an increased peak area was identified between control and fibrotic tissues (control: 8.2 arb. u. ± 2.3 arb. u.; fibrosis: 21.5 arb. u. ± 3.2 arb. u.; $p = 0.0774$). For COL I in the connective tissue from human breast tissues, spectral deconvolution showed a statistically significant increase in intensity in fibrotic cases for the band at 1608 cm^{-1} (control: 1.7 arb. u. ± 0.5 arb. u.; fibrosis: 4.8 arb. u. ± 0.2 arb. u.; $p = 0.0012$). An increased peak area at 1608 cm^{-1} was also seen when comparing COL I in control and fibrotic lymph nodes (control: 2.4 arb. u. ± 0.9 arb. u.; fibrosis: 5.6 arb. u. ± 1.9 arb. u.; $p = 0.0977$). We further observed a statistically significant increased peak area at 1608 cm^{-1} in the fibrotic myocardium (control: 5.1 arb. u. ± 0.5 arb. u.; fibrosis: 9.0 arb. u. ± 0.7 arb. u.; $p = 0.05$).

In addition to peak areas, spectral deconvolution also enables the calculation of the width of the underlying peaks (Fig. 4f). In all analyzed tissues, statistically significant increases in peak widths were observed in fibrotic COL I compared to control tissue.

As a third parameter of the subpeak at 1608 cm^{-1}, we calculated the peak intensity ratio to the maximum of the highest amide I subpeak located at 1667 cm^{-1} (Fig. 5a). A statistically significant decrease in the peak ratio was identified in fibrotic liver hepatocytes and breast tissues (control liver lob: 2.2 arb. u. ± 0.3 arb. u.; fibrotic liver lob: 1.3 arb. u. ± 0.3 arb. u.; $p = 0.0252$; control breast tissue: 3.5 arb. u. ± 0.9 arb. u.; fibrotic breast tissue: 2.9 arb. u. ± 0.2 arb. u.; $p = 0.0136$). Similar tendencies were demonstrated for the fibrotic tissues of liver portal triad (control: 2.5 arb. u. ± 0.5 arb. u.; fibrosis: 1.7 arb. u. ± 0.3 arb. u.; $p = 0.1543$), colon (control: 2.330 arb. u. ± 0.1 arb. u.; fibrosis: 2.7 arb. u. ± 0.3 arb. u.; $p = 0.1194$), lymph nodes (control: 3.6 arb. u. ± 0.6 arb. u.; fibrosis: 2.2 arb. u. ± 0.8 arb. u.; $p = 0.0699$) and myocardium (control: 2.8 arb. u. ± 0.1 arb. u.; fibrosis: 2.5 arb. u. ± 0.1 arb. u.; $p = 0.0767$). In addition to spectral deconvolution, which evaluated the amide I band of the averaged COL I spectra from Raman maps, a sum filter-based image analysis was employed, evaluating the entity of all COL I spectra of one scan. Here, filter images from COL I maps were created at 1608±10 cm^{-1} and 1667±25 cm^{-1} and divided by each other to assess the peak ratio per pixel in each image. The histograms calculated by filter image-based ratios are displayed in Fig. 5b. Throughout all tissue sections, modes and percentiles showed shifts to lower values in the fibrotic case compared to control. Analysis of the mode (Fig. 5c) revealed the value appearing the most frequent in each image, where a high value was describing ratios with less intense peaks at 1608 cm^{-1}. The analysis of the modes representing the whole COL I maps indicated statistically significant differences for liver hepatocytes (control: 7.8 arb. u. ± 0.3 arb. u.; fibrosis: 4.9 arb. u. ± 0.8 arb. u.; $p = 0.0099$), liver portal triad (control: 9.3 arb. u. ± 0.8 arb. u.; fibrosis: 6.2 arb. u. ± 1.00 arb. u.; $p = 0.0243$) and breast tissues (control: 9.7 arb. u. ± 0.8 arb. u.; fibrosis: 6.3 arb. u. ± 0.9 arb. u.; $p = 0.0162$). Tendencies of separations in modes were found in all other tissue types such as colon (control: 9.4 arb. u. ± 0.8 arb. u.; fibrosis: 8.3 arb. u. ± 0.9 arb. u.; $p = 0.2885$), lymph nodes (control: 16.9 arb. u. ± 2.0 arb. u.; fibrosis: 11.0 arb. u. ± 2.9 arb. u.; $p = 0.0766$) and myocardium (control: 11.3 arb. u. ± 1.6 arb. u.; fibrosis: 8.5 arb. u. ± 1.8 arb. u.; $p = 0.1789$).

4. Discussion

Fibrosis is one consequence of most chronic inflammatory disorders, and COL I-composed fibers are the main component of a fibrotic capsule or scar. Early identification of tissue fibrosis followed by timely treatment could potentially allow the prevention or reversal of organ damage [58]; however, besides indirect diagnosis due to organ malfunction or failure, the current gold standard in fibrosis diagnosis is histopathological assessment of collagen fibers in tissue biopsies [59,60]. This invasive biopsy procedure involves not only time-consuming laboratory work and a potential observer bias [61,62], it is also only possible at a late-stage of the disease. Furthermore, especially in collagen-rich tissues, e.g. the breast tissue, histology-based identification of fibrotic lesions is limited. Here, trained pathologists need to take morphometric observations of histologically-stained tissue sections and perform visual scoring to identify the existence of fibrosis [63]. Clinical diagnosis of fibrotic disease might occasionally be determined differently due to individual experience and knowledge, causing variations of diagnosis results. Also, there exists a limitation of deep collagen fiber characterization, classification, and quantification by classical stains [64,65].

In this study, we demonstrated that non-destructive and marker-independent Raman microspectroscopy and Raman imaging have the potential to detect fibrotic COL I alterations throughout different tissue origins. Tissues from different human organs were investigated, including liver, colon, breast, lymph nodes and myocardium in their respective control stage as well as after the development of fibrotic morphologies. Conventional histological methods were compared to RMS-based approaches. PSR staining was utilized to distinguish between the alignment of collagen fibers in the different tissue types [66,67]. Recently, digital-imaging analysis was used in combination with PSR to evaluate topological alternations in collagen fibers and their compactness in order to gain more understating of fibrosis dynamics [68]. Our results demonstrated that collagen fibers in fibrosis were more frequently aligned in parallel than non-pathological collagen fibers, in which the alignment was randomly distributed. However, the extent to which PSR can be relied upon to assess fibrotic collagen fibers is still controversial. It has been broadly reported that the color of the fibers demonstrates a certain state of collagens [69]. Although it is still under debate whether the colors of the PSR are capable of discerning maturity and thickness of the collagen fibers [70,71], it is believed that in thick/mature collagen fibers, the interaction with polarized light results in a stronger red birefringence and for thinner fibers in a weaker green birefringence [72–74]. The strong positive birefringence of collagen fibers is the result of the superposition of the right-handed superhelix with the left-handed helix, which comprises the three polypeptide chains, leading to an alignment of the amino acid chains approximately parallel to the molecular axis [72]. Moreover, it is also reported that green-yellow collagen fibers may represent procollagen, intermediate collagen, or Col III fibers [66,75,76]. Nevertheless, to date, the exact indication of the colors in PSR staining with polarized light remains debatable and requires complementary validations such as IF staining. In our study, quantification of the presence of red and green fibers revealed statistically significant differences between the control and fibrosis samples in most tissue types except colon and heart. However, shifts in the ratio of red

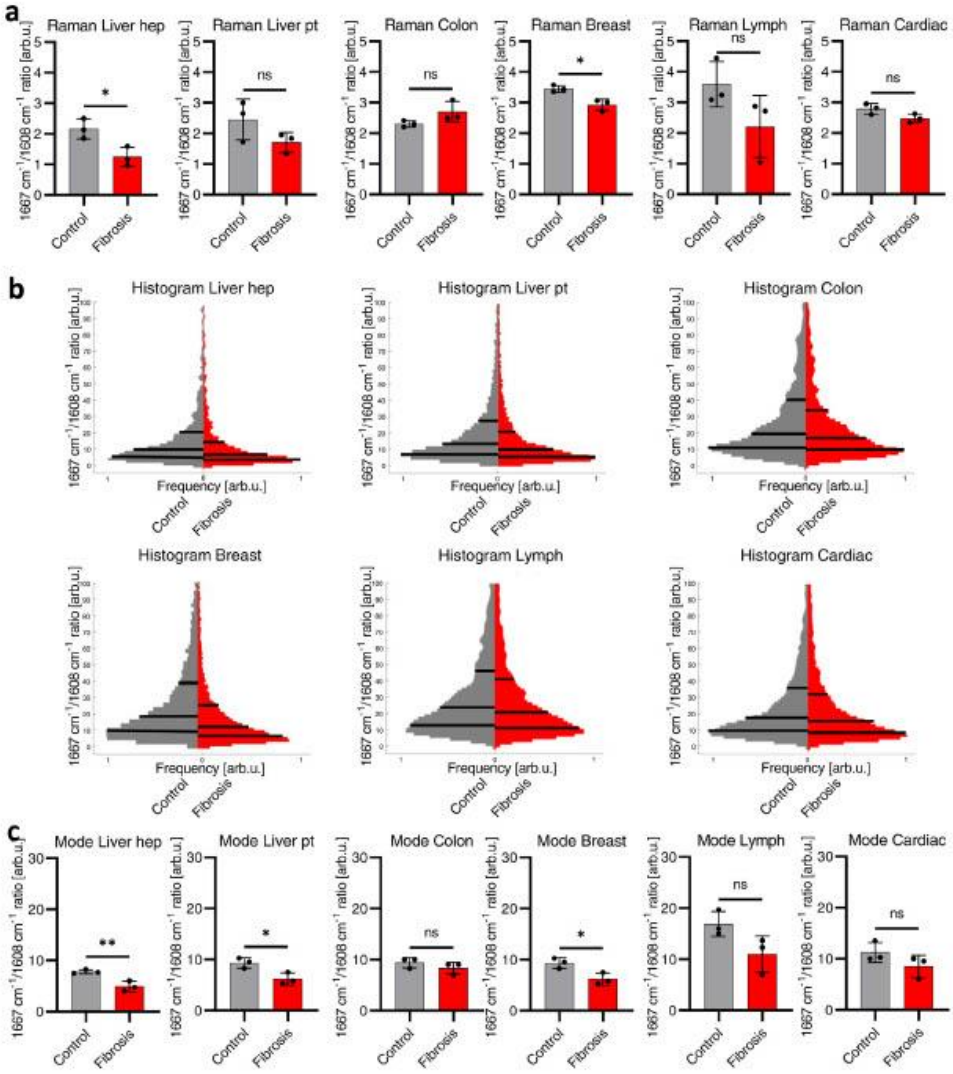

Fig. 5. Peak ratio of amide I region from averaged COL I Raman spectra and Raman image analyses display similar separation between control and fibrosis through all tissue types. (a) Peak ratio of averaged COL I spectra at 1608 cm^{-1} normalized by amide I maximum. (b) Histograms of filter image ratio at 1608 cm^{-1}, normalized by amide I maximum (1667 cm^{-1}). Lines in the histogram represent the 25, 50 and 75 percentiles while the widest position of the histograms is displaying the mode. (c) Frequency of modes from filter image ratio at 1608 cm^{-1} normalized by amide I maximum. Statistical analysis: t-test, $n = 3$, $^*p < 0.05$.

and green collagen fibers did not show consistency throughout fibrotic tissues, showing that even though PSR is widely used in pathology and histology labs, several abovementioned uncertainties still exist [77]. Furthermore, some studies also revealed the changes in rotation of the microscope stage can result in color reverse, which lacks robustness for both qualitative and quantitative results [71,78].

IF staining is a powerful tool to detect distinctive signals of specific proteins, which has been widely used to specify collagen subtypes in fibrotic tissue assessment [79]. Nevertheless, limited availability and specificity of primary antibodies, their high costs, and the need for complex staining procedures (especially when using archived FFPE material) favors traditional histological staining as the conventional method for fibrosis diagnosis. Limited possibility of quantitative analysis is another issue with IF staining. Autofluorescence from either the tissue itself or the secondary fluorescence-labelled antibodies can cause variations in image quantification [80]. A main drawback, which is highly relevant to this study, is that the COL I antibodies are unable to differentiate pathological fibrotic COL I from native/healthy COL I. This limi-

tation also applies to SHG imaging since this method, although being non-invasive and marker-independent, does also not allow the discrimination of the different collagen types [81].

To circumvent the obstacles of routine histological and IF staining methods, RMS was used to distinguish diseased COL I from control COL I fibers. Multivariate data analysis tools such as PCA are a common way to provide detailed information about fibrotic COL I alteration contributed by minute shifts in Raman spectra [82]. Nonetheless, in this study, PCA was insufficient to robustly discriminate fibrotic pathologies throughout tissue origins (Supplementary Fig. S1). Moreover, the utilization of both LDA and neural networks for the classification of Raman data failed to yield desirable accuracy levels. Despite LDA yielding an accuracy rate of only 62% when classifying the Raman data of native and fibrotic COL I fibers, an improvement to 71% accuracy was observed when utilizing neural networks (as stated in Supplementary Table 1). The discrepancy in performance could be attributed to the limited sample size utilized during classification as well as the potential impact of variations specific to the organ on the accuracy of classification.

By implementing spectral deconvolution of the amide I signature, information regarding amino acid sequence and secondary structure of specific protein components can be obtained [83,84]. Through spectral deconvolution on averaged COL I Raman spectra, we were able to demonstrate the correlation of the subpeak at 1608 cm^{-1} in the amide I region to fibrotic COL I fibers regardless of the origin of the tissue and disease. Compared with the controls, a larger peak width and peak area were found in most of the examined fibrotic tissues. While these values were statistically significant for liver, breast tissue, and myocardium, a distinct trend was seen in the colon and in lymph nodes. We also found statistically significant differences between controls and fibrotic COL I when comparing histograms and modes of peak ratio images representing single spectra of COL I in whole Raman scans. Whereas other subpeaks at 1588 cm^{-1} and 1638 cm^{-1}, which represent hydroxyproline and β-sheet [85], showed no statistical significance between the control and fibrotic groups. The increase at the Raman shift of 1608 cm^{-1} in fibrotic COL I can be assigned to the amino acid tyrosine and its precursor phenylalanine [86,87]. Recent work from Baumann and Gebauer demonstrated that the primary structure of procollagens has an impact on the binding affinity of heat shock protein 47 (HSP47) at the site of the COLI I triple helix [80]. HSP47 has been widely discussed to be a specific chaperon to procollagen, which might play an important role in COL I folding related to fibrotic diseases [88], making it a potential therapeutic target for anti-fibrotic drugs. The composition of collagens is mainly the repeated triplets Glycine-Xaa-Yaa, where Xaa and Yaa can be any amino acid. Glycine preserves the certain position to maintain the triple helix structure of collagen [89]. For Xaa and Yaa, proline and hydroxyproline are common representatives at the sites [90,91]. Nevertheless, Xaa and Yaa can be also replaced by alternative amino acids such as leucine, arginine, tyrosine or phenylalanine, which has been reported to induce different dissociation constants of the binding of procollagen and HSP47 [91]. Baumann and Gebauer utilized a COL II peptide library to modify new binding sequence motifs with phenylalanine, tyrosine, and leucine, showing a significant decrease in the value of dissociation constant or binding affinity [80]. Increased binding affinity of HSP47 might contribute to the production and formation of excessive amounts of collagen ultimately leading to fibrosis [88,92]. The increased intensity in the fibrotic collagen fibers at the Raman shift of 1608 cm^{-1} might indicate the presence of higher amounts of amino acids with an aromatic ring (phenylalanine and tyrosine) [87,93]. It is hypothesized that procollagens which contain relatively high amounts of aromatic amino acids can bind easier to HSP47 than those without these specific amino acids. Nevertheless, the sequence of fibrotic COL I requires further investigation to provide proper evidence for our findings. An important future direction is to conduct the presented experiments on more fibrosis-related diseases of further tissue origins and collect more tissues from patients. Additionally, the proposed workflow of accessing fibrosis via spectral deconvolution needs to be tested on non-FFPE samples. Successful identification of fibrosis on fresh tissue would allow direct evaluation of pathologic tissue in the surgical room. The identified Raman biomarker could further enable to identify a fibrotic related origin of diseases with unknown pathology.

5. Conclusion

This study demonstrates the potential of RMS as a diagnostic approach to evaluate and identify fibrotic pathologies. We showed the capability of RMS to discern fibrotic COL I in human fibrotic tissues via deconvolution of the amide I band, identifying one specific spectral biomarker robust enough to target fibrotic alterations throughout various tissue origins. This molecular-sensitive approach enables fibrosis monitoring beyond tissue-specific morphological, quantitative, and qualitative differences in collagen patterns. Although only a selection of fibrosis-related diseases was evaluated in this study, this procedure could evolve to a future tool offering pathologists a non-destructive, marker-independent, and potentially automatable way to conduct fibrosis investigation without the need of conventional staining procedures.

Data Availability Statement

The data that support the findings of this study are available from the corresponding author upon reasonable request.

Declaration of Competing Interest

The authors declare no competing financial interests or personal relationships that could have appeared to influence the work reported in this paper.

Acknowledgements

The authors thank the University Department of General, Visceral and Transplant Surgery, University Hospital Tübingen and UCLA for providing the human tissue samples. The work was conducted in the framework of the Graduate School 2543/1 "Intraoperative Multi-Sensory Tissue-Differentiation in Oncology" funded by the German Research Foundation (DFG). Further funding was received by the European Union (H2020-EU, 812865, DELIVER), DFG (INST 2388/64-1, INST 2388/33-1 and Germany's Excellence Strategy, EXC 2180-390900677), the Ministry of Science, Research, and the Arts of Baden-Wuerttemberg (33-729.55-3/214 and SI-BW 01222-91) and the State Ministry of Baden-Wuerttemberg for Economic Affairs, Labor and Tourism (3-4332.62-NMI/65).

Supplementary materials

Supplementary material associated with this article can be found, in the online version, at doi:10.1016/j.actbio.2023.03.016.

References

[1] T.A. Wynn, Cellular and molecular mechanisms of fibrosis, J. Pathol. 214 (2) (2008) 199–210.
[2] C. Chandler, T. Liu, R. Buckanovich, L.G. Coffman, The double edge sword of fibrosis in cancer, Transl. Res. 209 (2019) 55–67.
[3] D.M. Dolivo, Anti-fibrotic effects of pharmacologic FGF-2: a review of recent literature, J. Mol. Med. 100 (6) (2022) 847–860.
[4] T.A. Wynn, Fibrotic disease and the T(H)1/T(H)2 paradigm, Nat. Rev. Immunol. 4 (8) (2004) 583–594.

[5] L.A. Murtha, M.J. Schuliga, N.S. Mabotuwana, S.A. Hardy, D.W. Waters, J.K. Burgess, D.A. Knight, A.J. Boyle, The processes and mechanisms of cardiac and pulmonary fibrosis, Front. Physiol. 8 (2017) 777.
[6] R. Rasotto, D. Berlato, M.H. Goldschmidt, V. Zappulli, Prognostic significance of canine mammary tumor histologic subtypes; an observational cohort study of 229 cases, Vet. Pathol. 54 (4) (2017) 571–578.
[7] C.C. Choong, S.K. Venkatesh, E.P. Siew, Accuracy of routine clinical ultrasound for staging of liver fibrosis, J. Clin. Imaging Sci. 2 (2012) 58.
[8] L. Petitclerc, G. Gilbert, B.N. Nguyen, A. Tang, Liver fibrosis quantification by magnetic resonance imaging, Top. Magn. Reson. Imaging. 26 (6) (2017) 229–241.
[9] S.M. Humphries, J.J. Swigris, K.K. Brown, M. Strand, Q. Gong, J.S. Sundy, G. Raghu, M.I. Schwarz, K.R. Flaherty, R. Sood, T.G. O'Riordan, D.A. Lynch, Quantitative high-resolution computed tomography fibrosis score: performance characteristics in idiopathic pulmonary fibrosis, Eur. Respir. J. 52 (3) (2018).
[10] T. Liu, X. Wang, M.A. Karsdal, D.J. Leeming, F. Genovese, Molecular serum markers of liver fibrosis, Biomark. Insights 7 (2012) 105–117.
[11] A. Stainer, P. Faverio, S. Busnelli, M. Catalano, M.Della Zoppa, A. Marruchella, A. Pesci, F. Luppi, Molecular biomarkers in idiopathic pulmonary fibrosis: state of the art and future directions, Int. J. Mol. Sci. 22 (12) (2021).
[12] S.B. Montesi, P. Désogère, B.C. Fuchs, P. Caravan, Molecular imaging of fibrosis: recent advances and future directions, J. Clin. Invest. 129 (1) (2019) 24–33.
[13] R. Urtasun, N. Nieto, Hepatic stellate cells and oxidative stress, Rev. Esp. Enferm. Dig. 99 (4) (2007) 223–230.
[14] L.B. Mostaço-Guidolin, A.C. Ko, F. Wang, B. Xiang, M. Hewko, G. Tian, A. Major, M. Shiomi, M.G. Sowa, Collagen morphology and texture analysis: from statistics to classification, Sci. Rep. 3 (2013) 2190.
[15] T.D. Clemons, M. Bradshaw, P. Toshniwal, N. Chaudhari, A.W. Stevenson, J. Lynch, M.W. Fear, F.M. Wood, K.S. Iyer, Coherency image analysis to quantify collagen architecture: implications in scar assessment, RSC Adv. 8 (18) (2018) 9661–9669.
[16] P. Whittaker, R.A. Kloner, D.R. Boughner, J.G. Pickering, Quantitative assessment of myocardial collagen with picrosirius red staining and circularly polarized light, Basic Res. Cardiol. 89 (5) (1994) 397–410.
[17] A.E. Woessner, J.D. McGee, J.D. Jones, K.P. Quinn, Characterizing differences in the collagen fiber organization of skin wounds using quantitative polarized light imaging, Wound Repair Regen. 27 (6) (2019) 711–714.
[18] M. Brereton, B. De La Salle, J. Ardern, K. Hyde, J. Burthem, Do we know why we make errors in morphological diagnosis? An analysis of approach and decision-making in haematological morphology, EBioMedicine 2 (9) (2015) 1224–1234.
[19] K.G.M. Brockbank, R.W. J. Xie, S.F. Hamm-Alvarez, Z.Z. Chen, K. Schenke-Layland, Quantitative second harmonic generation imaging of cartilage damage, Cell Tissue Bank. 9 (4) (2008) 299–307.
[20] K. Schenke-Layland, J. Xie, E. Angelis, B. Starcher, K. Wu, I. Riemann, W.R. Maclellan, S.F. Hamm-Alvarez, Increased degradation of extracellular matrix structures of lacrimal glands implicated in the pathogenesis of Sjögren's syndrome, Matrix Biol. 27 (1) (2008) 53–66.
[21] K. Schenke-Layland, I. Riemann, U.A. Stock, K. König, Imaging of cardiovascular structures using near-infrared femtosecond multiphoton laser scanning microscopy, J. Biomed. Opt. 10 (2) (2005) 024017.
[22] L. Becker, N. Janssen, S.L. Layland, T.E. Mürdter, A.T. Nies, K. Schenke-Layland, J. Marzi, Raman imaging and fluorescence lifetime imaging microscopy for diagnosis of cancer state and metabolic monitoring, Cancers 13 (22) (2021) 5682.
[23] K. Eberhardt, C. Stiebing, C. Matthäus, M. Schmitt, J. Popp, Advantages and limitations of Raman spectroscopy for molecular diagnostics; an update, Expert Rev. Mol. Diagn. 15 (6) (2015) 773–787.
[24] M.G. Martinez, A.J. Bullock, S. Macneil, I.U. Rehman, Characterisation of structural changes in collagen with Raman spectroscopy, Appl. Spectrosc. Rev. 54 (6) (2019) 509–542.
[25] G.W. Auner, S.K. Koya, C. Huang, B. Broadbent, M. Trexler, Z. Auner, A. Elias, K.C. Mehne, M.A. Brusatori, Applications of Raman spectroscopy in cancer diagnosis, Cancer Metast. Rev. 37 (4) (2018) 691–717.
[26] G. Pezzotti, Raman spectroscopy in cell biology and microbiology, J. Raman Spectrosc. 52 (12) (2021) 2348–2443.
[27] K. Sugiyama, J. Marzi, J. Alber, E.M. Brauchle, M. Ando, Y. Yamashiro, B. Ramkhelawon, K. Schenke-Layland, H. Yanagisawa, Raman microspectroscopy and Raman imaging reveal biomarkers specific for thoracic aortic aneurysms, Cell Rep. Med. 2 (5) (2021) 100261.
[28] R. Beatty, C.E. Lu, J. Marzi, R.E. Levey, D. Carvajal Berrio, G. Lattanzi, R. Wylie, R. O'Connor, E. Wallace, G. Ghersi, M. Salamone, E.B. Dolan, S.L. Layland, K. Schenke-Layland, G.P. Duffy, The foreign body response to an implantable therapeutic reservoir in a diabetic rodent model, Tissue Eng. Part C 27 (10) (2021) 515–528.
[29] S.K. Paidi, J.R. Troncoso, M.G. Harper, Z. Liu, K.G. Nguyen, S. Ravindranathan, L. Rebello, D.E. Lee, J.D. Ivers, D.A. Zaharoff, N. Rajaram, I. Barman, Raman spectroscopy reveals phenotype switches in breast cancer metastasis, Theranostics 12 (12) (2022) 5351–5363.
[30] J. Depciuch, A. Stanek-Widera, M. Warchulska, D. Lange, K. Sarwa, A. Kaziorowska, M. Kula, J. Cebulski, Identification of chemical changes in healthy breast tissue caused by chemotherapy using Raman and FTIR spectroscopy; a preliminary study, Infrared Phys. Technol. 102 (2019).
[31] D. Lazaro-Pacheco, M.A. Shaaban, N.A. Titiloye, S. Rehman, I.U. Rehman, Elucidating the chemical and structural composition of breast cancer using Raman micro-spectroscopy, EXCLI J. 20 (2021) 1118–1132.
[32] F. Gaba, W.J. Tipping, M. Salji, K. Faulds, D. Graham, H.Y. Leung, Raman spectroscopy in prostate cancer: techniques, applications and advancements, Cancers 14 (6) (2022) 1535.
[33] K. Viswanathan, K. Soumya, K. Gurusankar, S. Jeyavijayan, Raman spectroscopic analysis of ovarian cancer tissues and normal ovarian tissues, Laser Phys. 29 (2019).
[34] L. Becker, F. Fischer, J.L. Fleck, N. Harland, A. Herkommer, A. Stenzl, W.K. Aicher, K. Schenke-Layland, J. Marzi, Data-driven identification of biomarkers for in situ monitoring of drug treatment in bladder cancer organoids, Int. J. Mol. Sci. 23 (13) (2022) 6956.
[35] H. Russell Jr, A modification of Movat's pentachrome stain, Arch. Pathol. 94 (2) (1972) 187–191.
[36] K. Schenke-Layland, I. Riemann, U.A. Stock, K. König, Imaging of cardiovascular structures using near-infrared femtosecond multiphoton laser scanning microscopy, J. Biomedic. Opt. 10 (2) (2005) 024017.
[37] W. Liu, E. Ralston, A new directionality tool for assessing microtubule pattern alterations, Cytoskeleton 71 (4) (2014) 230–240.
[38] R. Rezakhaniha, A. Agianniotis, J.T. Schrauwen, A. Griffa, D. Sage, C.V. Bouten, F.N. van de Vosse, M. Unser, N. Stergiopulos, Experimental investigation of collagen waviness and orientation in the arterial adventitia using confocal laser scanning microscopy, Biomech. Model. Mechanobiol. 11 (3-4) (2012) 461–473.
[39] A. Zbinden, S.L. Layland, M. Urbanczyk, D.A. Carvajal Berrio, J. Marzi, M. Zauner, A. Hammerschmidt, E.M. Brauchle, K. Sudrow, S. Fink, M. Templin, S. Liebscher, G. Klein, A. Deb, G.P. Duffy, G.M. Crooks, J.A. Eble, H.K.A. Mikkola, A. Nsair, M. Seifert, K. Schenke-Layland, Nidogen-1 mitigates ischemia and promotes tissue survival and regeneration, Adv. Sci. 8 (4) (2021) 2002500.
[40] M. Holl, M.L. Rasch, L. Becker, A.L. Keller, L. Schultze-Rhonhof, F. Ruoff, M. Templin, S. Keller, F. Neis, F. Keßler, J. Andress, C. Bachmann, B. Krämer, K. Schenke-Layland, S.Y. Brucker, J. Marzi, M. Weiss, Cell type-specific anti-adhesion properties of peritoneal cell treatment with plasma-activated media (PAM), Biomedicines 10 (4) (2022).
[41] A. Zbinden, J. Marzi, K. Schlünder, C. Probst, M. Urbanczyk, S. Black, E. Brauchle, S.L. Layland, U. Kraushaar, G.P. Duffy, K. Schenke-Layland, P. Loskill, Non-invasive marker-independent high content analysis of a microphysiological human pancreas-on-a-chip model, Matrix Biol. 85-86 (2020) 205–220.
[42] J. Marzi, E. Brauchle, K. Schenke-Layland, M.W. Rolle, Non-invasive functional molecular phenotyping of human smooth muscle cells utilized in cardiovascular tissue engineering, Acta Biomater. 89 (2019) 193–205.
[43] H. Ye, U.Kruger Rahul, T. Wang, S. Shi, J. Norfleet, S. De, Burn-related collagen conformational changes in ex vivo porcine skin using raman spectroscopy, Sci. Rep. 9 (1) (2019) 19138.
[44] X. Li, Y. Zhang, P. Yu, Association of bio-energy processing-induced protein molecular structure changes with CNCPS-based protein degradation and digestion of co-products in dairy cows, J. Agric. Food Chem. 64 (20) (2016) 4086–4094.
[45] F. Pedregosa, G. Varoquaux, A. Gramfort, V. Michel, B. Thirion, O. Grisel, M. Blondel, P. Prettenhofer, R. Weiss, V. Dubourg, J. Vanderplas, A. Passos, D. Cournapeau, M. Brucher, M. Perrot, E. Duchesnay, Scikit-learn: Machine Learning in {P}ython}, J. Mach. Learn. Res. 12 (2011) 2825–2830.
[46] D.B. Kingma, Adam: A method for stochastic optimization, CoRR (2014) abs/1412.6980.
[47] A.V. Shinde, C. Humeres, N.G. Frangogiannis, The role of α-smooth muscle actin in fibroblast-mediated matrix contraction and remodeling, Biochim. Biophys. Acta Mol. Basis Dis. 1863 (1) (2017) 298–309.
[48] I. Notingher, C. Green, C. Dyer, E. Perkins, N. Hopkins, C. Lindsay, L.L. Hench, Discrimination between ricin and sulphur mustard toxicity in vitro using Raman spectroscopy, J. R. Soc. Interface 1 (1) (2004) 79–90.
[49] Z. Huang, A. McWilliams, H. Lui, D.I. McLean, S. Lam, H. Zeng, Near-infrared Raman spectroscopy for optical diagnosis of lung cancer, Int. J. Cancer 107 (6) (2003) 1047–1052.
[50] W.T. Cheng, M.T. Liu, H.N. Liu, S.Y. Lin, Micro-Raman spectroscopy used to identify and grade human skin pilomatrixoma, Microsc. Res. Tech. 68 (2) (2005) 75–79.
[51] D.P. Lau, Z. Huang, H. Lui, C.S. Man, K. Berean, M.D. Morrison, H. Zeng, Raman spectroscopy for optical diagnosis in normal and cancerous tissue of the nasopharynx-preliminary findings, Lasers Surg. Med. 32 (3) (2003) 210–214.
[52] T.T. Nguyen, C. Gobinet, J. Feru, S.B. Pasco, M. Manfait, O. Piot, Characterization of type I and IV collagens by raman microspectroscopy: identification of spectral markers of the dermo-epidermal junction, Spectroscopy 27 (2012) 686183.
[53] J. Cárcamo-Vega, A. Aliaga, R. Clavijo, B. Manuel, M. Vallette, Raman study of the shockwave effect on collagens, Spectrochim. Acta Part A 86 (2011) 360–365.
[54] E. Ó Faoláin, M.B. Hunter, J.M. Byrne, P. Kelehan, M. McNamara, H.J. Byrne, F.M. Lyng, A study examining the effects of tissue processing on human tissue sections using vibrational spectroscopy, Vibr. Spectrosc. 38 (1) (2005) 121–127.
[55] N. Nakamura, P. Moënne-Loccoz, K. Tanizawa, M. Mure, S. Suzuki, J.P. Klinman, J. Sanders-Loehr, Topaquinone-Dependent amine oxidases: identification of reaction intermediates by Raman spectroscopy, Biochemistry 36 (38) (1997) 11479–11486.
[56] Z.Q. Wen, Raman spectroscopy of protein pharmaceuticals, J. Pharm. Sci. 96 (11) (2007) 2861–2878.
[57] K. Belbachir, R. Noreen, G. Gouspillou, C. Petibois, Collagen types analysis and differentiation by FTIR spectroscopy, Anal. Bioanal. Chem. 395 (3) (2009) 829–837.
[58] M. Sisto, D. Ribatti, S. Lisi, Organ fibrosis and autoimmunity: the role of inflammation in TGFβ-dependent EMT, Biomolecules 11 (2) (2021).

[59] S. Seger, M. Stritt, E. Vezzali, O. Nayler, P. Hess, P.M.A. Groenen, A.K. Stalder, A fully automated image analysis method to quantify lung fibrosis in the bleomycin-induced rat model, PLoS One 13 (3) (2018) e0193057,
[60] L.C. Testa, Y. Jule, L. Lundh, K. Bertotti, M.A. Merideth, K.J. O'Brien, S.D. Nathan, D.C. Venuto, S. El-Chemaly, M.C.V. Malicdan, B.R. Gochuico, Automated digital quantification of pulmonary fibrosis in human histopathology specimens, Front. Med. 8 (2021) 607720,
[61] S.A. Taqi, S.A. Sami, L.B. Sami, S.A. Zaki, A review of artifacts in histopathology, J. Oral. Maxillofac. Pathol. 22 (2) (2018) 279,
[62] R.H. Hübner, W. Gitter, N.E. El Mokhtari, M. Mathiak, M. Both, H. Bolte, S. Freitag-Wolf, B. Bewig, Standardized quantification of pulmonary fibrosis in histological samples, BioTechniques 44 (4) (2008) 514–517 507-11,
[63] A.B. Fogo, C.E. Alpers, Navigating the challenges of fibrosis assessment; land in sight? J. Am. Soc. Nephrol. 22 (1) (2011) 11–13,
[64] R. Farhoodi, B.J. Lansdell, K.P. Kording, Quantifying how staining methods bias measurements of neuron morphologies, Front. Neuroinform. 13 (2019) 36,
[65] E.C. Jensen, Quantitative analysis of histological staining and fluorescence using ImageJ, Anatom. Rec. 296 (3) (2013) 378–381,
[66] J. Liu, M.Y. Xu, J. Wu, H. Zhang, L. Yang, D.X. Lun, Y.C. Hu, B. Liu, Picrosirius-polarization method for collagen fiber detection in tendons; a mini-review, Orthop. Surg. 13 (3) (2021) 701–707,
[67] F.E.-Z. Yassin, R. El-Dawela, M. Kerim, Picrosirius red staining assessment of collagen after dermal roller application; A minimally invasive percutaneous collagen induction therapy, Indian J. Dermatopathol. Diagn. Dermatol. 1 (2) (2014) 68–74,
[68] G.E. Courtoy, I. Leclercq, A. Froidure, G. Schiano, J. Morelle, O. Devuyst, F. Huaux, C. Bouzin, Digital image analysis of picrosirius red staining; a robust method for multi-organ fibrosis quantification and characterization, Biomolecules 10 (11) (2020),
[69] M.G. Monaghan, M. Holeiter, E. Brauchle, S.L. Layland, Y. Lu, A. Deb, A. Pandit, A. Nsair, K. Schenke-Layland, Exogenous miR-29B delivery through a hyaluronan-based injectable system yields functional maintenance of the infarcted myocardium, Tissue Eng.g Part A 24 (1-2) (2018) 57–67,
[70] C.M. López De Padilla, M.J. Coenen, A. Tovar, R.E. De la Vega, C.H. Evans, S.A. Müller, Picrosirius red staining; revisiting its application to the qualitative and quantitative assessment of collagen type I and type III in tendon, J. Histochem. Cytochem. 69 (10) (2021) 633–643,
[71] R. Lattouf, R. Younes, D. Lutomski, N. Naaman, G. Godeau, K. Senni, S. Changotade, Picrosirius red staining; a useful tool to appraise collagen networks in normal and pathological tissues, J. Histochem. Cytochem. 62 (10) (2014) 751–758,
[72] M. Wolman, F.H. Kasten, Polarized light microscopy in the study of the molecular structure of collagen and reticulin, Histochemistry 85 (1) (1986) 41–49,
[73] S.Y. Yu, C.A. Tozzi, J. Babiarz, P.C. Leppert, Collagen changes in rat cervix in pregnancy–polarized light microscopic and electron microscopic studies, Proc. Soc. Exp. Biol. Med. 209 (4) (1995) 360–368,
[74] B. Patel, Z. Xu, C.B. Pinnock, L.S. Kabbani, M.T. Lam, Self-assembled collagen–fibrin hydrogel reinforces tissue engineered adventitia vessels seeded with human fibroblasts, Sci. Rep. 8 (1) (2018) 3294,
[75] P.B. Jahagirdar, A.D. Kale, S. Hallikerimath, Stromal characterization and comparison of odontogenic cysts and odontogenic tumors using picrosirius red stain and polarizing microscopy; a retrospective and histochemical study, Indian J. Cancer 52 (3) (2015) 408–412,
[76] L.C. Junqueira, G. Bignolas, R.R. Brentani, Picrosirius staining plus polarization microscopy, a specific method for collagen detection in tissue sections, Histochem. J. 11 (4) (1979) 447–455,
[77] C.R. Drifka, A.G. Loeffler, K. Mathewson, G. Mehta, A. Keikhosravi, Y. Liu, S. Lemancik, W.A. Ricke, S.M. Weber, W.J. Kao, K.W. Eliceiri, Comparison of picrosirius red staining with second harmonic generation imaging for the quantification of clinically relevant collagen fiber features in histopathology samples, J. Histochem. Cytochem. 64 (9) (2016) 519–529,
[78] P.G.B. Coelho, M.V. Souza, L.G. Conceição, M.I.V. Viloria, S.A.O. Bedoya, Evaluation of dermal collagen stained with picrosirius red and examined under polarized light microscopy, An. Bras. Dermatol. 93 (3) (2018) 415–418,
[79] X. Lin, M. Barravecchia, R. Matthew Kottmann, P. Sime, D.A. Dean, Caveolin-1 gene therapy inhibits inflammasome activation to protect from bleomycin-induced pulmonary fibrosis, Sci. Rep. 9 (1) (2019) 19643,
[80] E.T. Abraham, S. Oecal, M. Mörgelin, P.W.N. Schmid, J. Buchner, U. Baumann, J.M. Gebauer, Collagen's primary structure determines collagen:HSP47 complex stoichiometry, J. Biol. Chem. 297 (6) (2021) 101169,
[81] Y. Padrez, L. Golubewa, T. Kulahava, T. Vladimirskaja, G. Semenkova, I. Adzerikho, O. Yatsevich, N. Amaegberi, R. Karpicz, Y. Svirko, P. Kuzhir, D. Rutkauskas, Quantitative and qualitative analysis of pulmonary arterial hypertension fibrosis using wide-field second harmonic generation microscopy, Sci. Rep. 12 (1) (2022) 7330,
[82] K. Sugiyama, J. Marzi, J. Alber, E.M. Brauchle, M. Ando, Y. Yamashiro, B. Ramkhelawon, K. Schenke-Layland, H. Yanagisawa, Raman microspectroscopy and Raman imaging reveal biomarkers specific for thoracic aortic aneurysms, Cell Rep. Med. 2 (5) (2021) 100261,
[83] N.C. Maiti, M.M. Apetri, M.G. Zagorski, P.R. Carey, V.E. Anderson, Raman spectroscopic characterization of secondary structure in natively unfolded proteins; α-Synuclein, J. Am. Chem. Soc. 126 (8) (2004) 2399–2408,
[84] G. Pezzotti, W. Zhu, Y. Hashimoto, E. Marin, T. Masumura, Y.-I. Sato, T. Nakazaki, Raman fingerprints of rice nutritional quality; a comparison between japanese koshihikari and internationally renowned cultivars, Foods 10 (12) (2021) 2936,
[85] H. Ye, F. Rahul, U. Kruger, T. Wang, S. Shi, J. Norfleet, S. De, Burn-related collagen conformational changes in ex vivo porcine skin using Raman spectroscopy, Sci. Rep. 9 (2019) 19138,
[86] C. Gullekson, L. Lucas, K. Hewitt, L. Kreplak, Surface-sensitive Raman spectroscopy of collagen I fibrils, Biophys. J. 100 (7) (2011) 1837–1845,
[87] R. Jyothi Lakshmi, V.B. Kartha, C. Murali Krishna, R.S. JG, G. Ullas, P. Uma Devi, Tissue Raman spectroscopy for the study of radiation damage; brain irradiation of mice, Radiat. Res. 157 (2) (2002) 175–182,
[88] P.S. Bellaye, O. Burgy, P. Bonniaud, M. Kolb, HSP47; a potential target for fibrotic diseases and implications for therapy, Expert Opin. Ther. Targets 25 (1) (2021) 49–62,
[89] A.V. Persikov, R.J. Pillitteri, P. Amin, U. Schwarze, P.H. Byers, B. Brodsky, Stability related bias in residues replacing glycines within the collagen triple helix (Gly-Xaa-Yaa) in inherited connective tissue disorders, Hum. Mutat. 24 (4) (2004) 330–337,
[90] J. Bella, M. Eaton, B. Brodsky, H.M. Berman, Crystal and molecular structure of a collagen-like peptide at 1.9 A resolution, Science 266 (5182) (1994) 75–81,
[91] R.Z. Kramer, J. Bella, P. Mayville, B. Brodsky, H.M. Berman, Sequence dependent conformational variations of collagen triple-helical structure, Nat. Struct. Biol. 6 (5) (1999) 454–457,
[92] T. Taguchi, A. Nazneen, A.A. Al-Shihri, K.A. Turkistani, M.S. Razzaque, Heat shock protein 47; a novel biomarker of phenotypically altered collagen-producing cells, Acta Histochem. Cytochem. 44 (2) (2011) 35–41,
[93] C. Gullekson, L. Lucas, K. Hewitt, L. Kreplak, Surface-sensitive Raman spectroscopy of collagen I fibrils, Biophys. J. 100 (7) (2011) 1837–1845,

Appendix 3

Rachel Beatty[§], **Chuan-En Lu[§]**, Julia Marzi, Ruth E Levey, Daniel A. Carvajal Berrio, Giulia Lattanzi, Robert Wylie, Raymond O'Connor, Eimear Wallace, Eimear B Dolan, Shannon L. Layland, Katja Schenke-Layland, Garry P Duffy. The Foreign Body Response to an Implantable Therapeutic Reservoir in a Diabetic Rodent Model. Tissue Eng Part C Methods. 2021 Oct; 27(10):515-528.

TISSUE ENGINEERING: Part C
Volume 27, Number 10, 2021

DOI: 10.1089/ten.tec.2021.0163

termis
Tissue Engineering
& Regenerative Medicine
International Society

METHODS ARTICLE

The Foreign Body Response to an Implantable Therapeutic Reservoir in a Diabetic Rodent Model

Rachel Beatty, BSc,[1,2,*,i] Chuan-En Lu, MS,[3,4,*] Julia Marzi, PhD,[3–6] Ruth E. Levey, PhD,[1] Daniel Carvajal Berrio, PhD,[3–5] Giulia Lattanzi, MEng,[1] Robert Wylie, MS,[1] Raymond O'Connor, MS,[1] Eimear Wallace, MS,[1] Giulio Ghersi, PhD,[6,7,ii] Monica Salamone, PhD,[6,7] Eimear B. Dolan, PhD,[8] Shannon L. Layland, PhD,[3,4] Katja Schenke-Layland, PhD,[3–6,iii] and Garry P. Duffy, PhD[1,2,9,iv]

Advancements in type 1 diabetes mellitus treatments have vastly improved in recent years. The move toward a bioartificial pancreas and other fully implantable systems could help restore patient's glycemic control. However, the long-term success of implantable medical devices is often hindered by the foreign body response. Fibrous encapsulation ''walls off'' the implant to the surrounding tissue, impairing its functionality. In this study we aim to examine how streptozotocin-induced diabetes affects fibrous capsule formation and composition surrounding implantable drug delivery devices following subcutaneous implantation in a rodent model. After 2 weeks of implantation, the fibrous capsule surrounding the devices were examined by means of Raman spectroscopy, micro-computed tomography (μCT), and histological analysis. Results revealed no change in mean fibrotic capsule thickness between diabetic and healthy animals as measured by μCT. Macrophage numbers (CCR7 and CD163 positive) remained similar across all groups. True component analysis also showed no quantitative difference in the alpha-smooth muscle actin and extracellular matrix proteins. Although principal component analysis revealed significant secondary structural difference in collagen I in the diabetic group, no evidence indicates an influence on fibrous capsule composition surrounding the device. This study confirms that diabetes did not have an effect on the fibrous capsule thickness or composition surrounding our implantable drug delivery device.

Keywords: diabetes mellitus, foreign body response, Raman spectroscopy, micro-computed tomography

Impact Statement

Understanding the impact diabetes has on the foreign body response (FBR) to our implanted material is essential for developing an effective drug delivery device. We used several approaches (Raman spectroscopy and micro-computed tomography imaging) to demonstrate a well-rounded understanding of the diabetic impact on the FBR to our devices, which is imperative for its clinical translation.

[1]Anatomy and Regenerative Medicine Institute (REMEDI), School of Medicine, National University of Ireland Galway, Galway, Ireland.
[2]SFI Research Centre for Advanced Materials and Bioengineering Research Centre (AMBER), Trinity College Dublin, Dublin, Ireland.
[3]Department of Biomedical Engineering, Eberhard Karls University, Tübingen, Germany.
[4]Department of Women's Health, Research Institute for Women's Health, Eberhard Karls University, Tübingen, Germany.
[5]Cluster of Excellence iFIT (EXC 2180) ''Image-Guided and Functionally Instructed Tumor Therapies,'' Eberhard Karls University, Tübingen, Germany.
[6]NMI Natural and Medical Sciences Institute at the University of Tübingen, Reutlingen, Germany.
[7]ABIEL srl, c/o ARCA Incubatore di Imprese, Palermo, Italia.
[8]Department of Biomedical Engineering, College of Science and Engineering, National University of Ireland Galway, Galway, Ireland.
[9]SFI Centre for Research in Medical Devices (CURAM), National University of Ireland Galway, Galway, Ireland.
*These authors contributed equally to this work.
[i]ORCID ID (https://orcid.org/0000-0003-2991-1783).
[ii]ORCID ID (https://orcid.org/0000-0001-7250-9808).
[iii]ORCID ID (https://orcid.org/0000-0001-8066-5157).
[iv]ORCID ID (https://orcid.org/0000-0002-4994-9511).

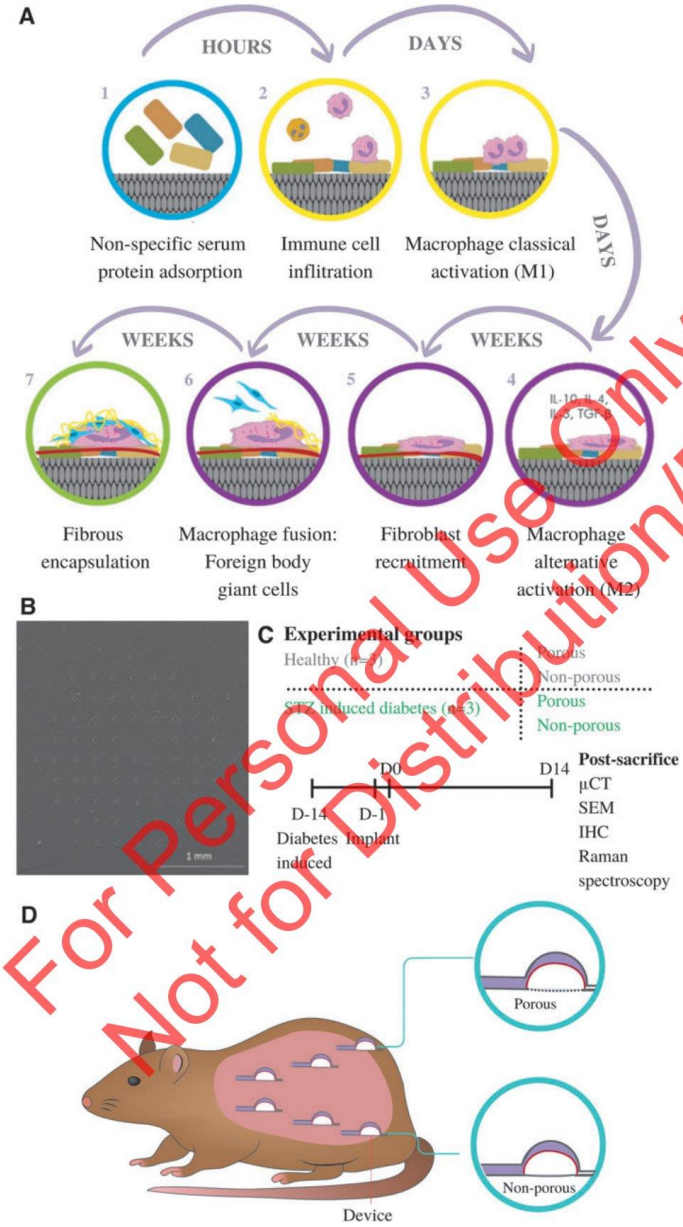

FIG. 1. Fibrous encapsulation and study design. **(A)** Schematic of the FBR to a medical device. **(B)** About 100 µm pores were laser cut into the membrane before device assemble. **(C)** Diabetes was induced using STZ in three animals 14 days before implantation. Fourteen days after implantation, post-sacrifice analysis was carried out on the explanted devices and surrounding tissue. **(D)** Three porous and three nonporous devices were subcutaneously implanted in all animals. FBR, foreign body response; IHC, immunohistochemistry; SEM, scanning electron microscope; STZ, streptozotocin. Color images are available online.

(Fig. 1D). Devices were secured to underlying muscle using a suture. The incision was closed with braided sutures. On day 14, devices were explanted *en bloc* with surrounding tissue. Tissue blocks were fixed in 4% paraformaldehyde overnight at 4°C and stored in 1×phosphate-buffered solution (PBS).

Micro-computed tomography

One porous and nonporous device per animal were selected for μCT analysis. Fixed samples were transferred into 2.5% phosphomolybdic acid (PMA) (673400; Hopkin & Williams) in 70% ethanol to enable visualization of collagen dense tissues.[33] Rat skin was scored before emulsion in the PMA solution to ensure sufficient uptake of the contrast agent (7 days). High-resolution scanning was performed on a Scanco Medical μCT 100 and subsequent dicom files were analyzed using Mimics research 18.0.525 software (Materialise). Thresholding of the fibrous capsule was performed by creating a green mask over the entire sample. Once the entire length of the device was mapped, a second yellow mask was created (background mask). A Boolean operation was performed to create a cyan mask (green minus yellow), to remove any background from the mask. The mask was calculated in 3D and a 2.4–2.6 mm circle was cropped from the center of the fibrous capsule. An .STL file of this cropped disk was exported for analysis on 3-Matic software 10× (Materialise). The fix wizard, a smoothing factor (0.8), autoremesh, wall thickness analysis, and segmentation was performed, as previously described.[7] The wall thickness analysis function creates a color map of the 3D reconstructed capsule between 0 and 200 μm (green, thin; red, thick). This information is exported as raw thickness measurements, which are subsequently presented as average values.

Scanning electron microscopy

Post-μCT imaging, samples were bisected longitudinally to create a cross-section of the device and surrounding tissue and further dehydrated through a series of graded alcohols (90% and 100%). Following dehydration, samples were critical point dried (EMITECH K850) to remove all liquid from the sample. Samples were mounted onto aluminum stubs using carbon adhesive tabs and gold sputter coated (Emscope SC500). Specimens were imaged using a Hitachi S-2600N Scanning Electron Microscope using a secondary electron detector (Vacuum 15 kV, electron Beam 50). Scanning electron microscope images were stitched together pseudo-colored using Mountains 8 software.

Histological analysis

Tissue processing. One porous and nonporous device per animal was selected at random. Samples were cut in half and processed for histological analysis. Tissues were orientated, embedded (Leica wax embedder) and sectioned (7 μm thick) onto positively charged slides. Slides were deparaffinized in xylene and brought to buffer through a series of graded alcohols.

Analysis of macrophage content. Sodium citrate antigen retrieval was performed for 30 min at 60°C (10 mM trisodium citrate, 0.05% Tween-20). Primary antibody CD68 (1:50; MCA341R; BioRad) was double stained with either CCR7 (1:100; ab32527; Abcam) or CD163 (1:250; ab32527; Abcam) and incubated for 60 min at 37°C. Secondary antibodies were then applied (Alexa Fluor 594 goat anti-mouse immunoglobulin G, 1:200; Alexa Fluor 488 goat anti-rabbit IgG, 1:200) and incubated for 60 min at 37°C. Nuclei were stained using Hoechst (1:1000). Slides were mounted using fluormount mounting media and stored at 4°C. Slides were imaged using a spinning disk confocal microscope (CSU22; Yokagawa) combined with Andor iQ 2.3 software. Analysis was performed as previously described by Coulter *et al.*[34]

Polarized light microscopy. The collagen content of the samples was analysis using picrosirus red staining. After rehydration the samples were stained in 0.1% fast green (pH 7, Fast Green FCF; Sigma-Aldrich) (30 min) followed by 0.1% Sirus red in picric acid (picrosirius red stain) (60 min) as previously established.[33] Samples were dehydrated, cleared in xylene, and mounted using DPX mounting medium. Images were captured using an Olympus BX4 polarized light microscope (Mason Technology Ltd., Dublin, Ireland) at 20× magnification. The polarizing lenses were positioned on the light path before the sample and the second polarizer (analyzer) after the sample. Images were taken at 0° and 90° to maximum polarization. The two captured images were merged in ImageJ (Fiji version 2.0.0) software. Mature and immature collagen was calculated by color thresholding by excluding the dark background, as previously described.[34] Dominant direction was determined using the Orientation J plugin on ImageJ.[35]

Immunofluorescence staining. Antigen retrieval was performed with pH 9 Tris-EDTA buffer (containing 10 mM Tris-base, 1 mM EDTA, and 0.05% Tween-20) followed by pH 6 citrate buffer (10 mM citric acid and 0.05% Tween-20). To minimize the unspecific binding of secondary antibodies, 2% goat serum block solution was used. Sections were incubated with one of the following primary antibodies: Rabbit polyclonal anti-collagen I (Col I; 1:500; Cedarlane, Burlington, CA), rabbit IgG1 polyclonal anti-Col III (1:75; Acris, Herford, Germany) and mouse IgG2a monoclonal anti-alpha-smooth muscle actin (α-SMA) (1:500; Sigma-Aldrich, St. Louis, MO) overnight at 4°C. Secondary antibodies were added: AlexaFluor 488-conjugated goat anti-rabbit (1:250; Thermo Fisher Scientific Life Technologies) was applied to the anti-Col I and III antibodies and AlexaFluor 594-conjugated goat anti-mouse (1:250; Thermo Fisher Scientific Life Technologies) for the anti-α-SMA antibody. The 3D immunofluorescence (IF) images were acquired using a confocal laser scanning microscope (LSM 880; Carl Zeiss Microscopy GmbH, Germany). Z stack imaging was used and followed by image processing (Imaris x64 9.5.1; Bitplane, CT). The excitation wavelengths of the lasers were 594, 488, and 405 nm, corresponding to α-SMA, Col I and III and DAPI, respectively. To test nonspecific binding of the antibodies, negative controls consisting of the same tissue samples were stained with only secondary antibodies. The histogram scale was adjusted to be invisible for the unspecific fluorescent signal based on the control tissue staining. The same histogram scale was applied to every staining section, defining the specificity of the positive signals of the IF staining. Moreover, RS was utilized to scan the IF staining sections. The Raman signals showed great correlation with the IF signals of α-SMA, Col I and III staining and the

acquired spectra were consistent with previous literatures.[36,37] Quantitative analysis of the IF images was performed based on the volume of each component and normalized by the whole tissue volume.

Raman spectroscopy. RS was performed with a Raman microscope (WITec alpha 300 R; WITec GmbH, Ulm, Germany) equipped with a charge-coupled device camera (WITec GmbH) to analyze the deparaffinized sections. The Control Five 5.2 software (WITec GmbH) was utilized to manage every scanning operation. A green laser (532 nm) with a power of 50 mW was used. Every section was maintained hydrated in PBS and imaged with a 63× objective (W Plan-Apochromat 63×/1.0 M27; Carl Zeiss GmbH, Jena, Germany). The samples were measured as follows: (1) to obtain the ECM reference spectra, IF-stained sections were imaged using a green fluorescence filter to localize positively stained areas as regions of interest for Raman image acquisition. The spectral information colocalizing with the pixel of positive fluorescence staining was extracted to generate the reference spectra. (2) Raman imaging of unstained sections was performed for each group on defined areas within the fibrotic capsules, localized in the brightfield mode. An acquisition time of 0.05 s per spectrum and a pixel resolution of 1 × 1 μm were applied to generate the spectral maps.

Spectral analysis. The Project Five 5.2 software (WITec GmbH) was used for analysis. Spectra were cropped to the wavenumber range from 200 to 3000 cm^{-1}. Artifacts originating from cosmic rays were removed. Subsequently, the graph background was subtracted and the area for every spectrum was normalized to 1. True component analysis (TCA) was then exerted to generate intensity distribution images that assess the localization of the previously defined reference components. For quantitative analysis, intensity distribution images for Col I, Col III, and α-SMA were extracted and analyzed in ImageJ.

For qualitative analysis of the molecular composition of the collagen fibers, principal component analysis (PCA) has been used to differentiate subtle molecular shifts, as described previously.[38] Col I spectra (400–1800 cm^{-1}) were extracted to undergo PCA calculation (The Unscrambler X; CAMO Software AS, Oslo, Norway). Interpretation of PCA results has been described previously.[39,40] Average score values and loadings were compared between implant materials and disease states.

Statistics

Statistics were performed using Prism 8 (GraphPad, La Jolla, CA) software. Results were presented as mean values ± standard deviation. Unpaired *t*-tests with parametric and nonparametric tests were conducted for the comparison between two groups. One-way parametric analysis of variance tests were used to compare the four groups in this study. Significant difference was only accepted when $p < 0.05$.

Experiment

Fibrous capsule thickness analysis

Visualization of soft tissue structures was permitted by passive uptake of a contrast agent. Three-dimensional reconstruction of high-resolution scans allowed for thresholding of the fibrous capsule (Fig. 2A). As previously described by Dolan *et al.*,[7] the region of interest was determined to be the tissue adjacent to the porous membrane beneath the "dome" of the DSR device; capsular measurements were only taken within this region. No significant change in mean fibrotic capsule thickness was seen across the groups (Fig. 2B). STZ-induced diabetes did not have an effect on the capsule thickness compared with the control ($p = 0.2350$). Subsequently, for additional qualitative analysis, the samples were bisected in half, processed and imaged using a scanning electron microscope (Fig. 2A). A clear visual representative was apparent, which strengthened our μCT findings that no change in fibrotic capsule thickness was seen. Histological sectioning for Masson's trichrome imaging resulted in slight destruction of the fibrous capsular area of interest. Clear representative fibrous capsule quantitative areas were not present across all groups (Fig. 2A).

Macrophage content analysis

To examine the macrophage response to the porous and nonporous DSR devices, the tissue sections were stained with a pan-macrophage marker (CD68), used in conjunction with a CCR7 or CD163 antibody and imaged at the region of interest (Fig. 3A). CCR7 and CD163-positive macrophages point toward M1 and M2 phenotypes, respectively.[41–43] As shown (Fig. 3B), the ratio of M1 (CCR7) and M2 (CD163) to CD68 was a similar in the diabetic state when compared with the healthy control. This suggests the ratio of macrophages was not affected by the diabetes disease state or the porosity of the devices.

Collagen content analysis

To examine the collagen fibers composition of the fibrous capsule in both diabetic and healthy animals, samples were stained with picrosirius red and imaged using polarized light microscopy (Fig. 4A). The overall coherency of the tissue was determined (Fig. 4B). No significant difference was seen in porous and nonporous samples in healthy and diabetes-induced animals ($p = 0.5827$, $p = 0.5998$). Diabetes did not affect the coherency of the capsule suggesting no compositional change in the capsule ($p = 0.3997$). Mature and immature fibers (Fig. 4C, D respectively) could be identified using color segmentation (red/orange = mature; green/yellow = immature collagen).[44,45] There was no significant difference seen between porous and nonporous samples in healthy and diabetes-induced animals (red/orange: healthy $p = 0.4152$, diabetic $p = 0.1649$; green/yellow: healthy $p = 0.4086$, diabetic $p = 0.2333$). Diabetes did not have an effect on the collagen maturity within the capsule (red/orange $p = 0.7190$; green/yellow $p = 0.8918$). The addition of pores into the DSR device, similarly, did not affect the collagen content within the capsule (Fig. 4B).

3D IF imaging of the fibrous tissue

To investigate the extent of the fibrous capsule formation, the tissue sections with the porous and nonporous devices in healthy and diabetic sections were stained with Col I, Col III, and α-SMA (Fig. 5A), to examine ECM deposition and the presence of myofibroblasts, which play a vital role in ECM remodeling and fibrosis.[46–48] Three-dimensional IF imaging was applied on the three biomarkers followed by image processing of the samples (Fig. 5B–D). The expression

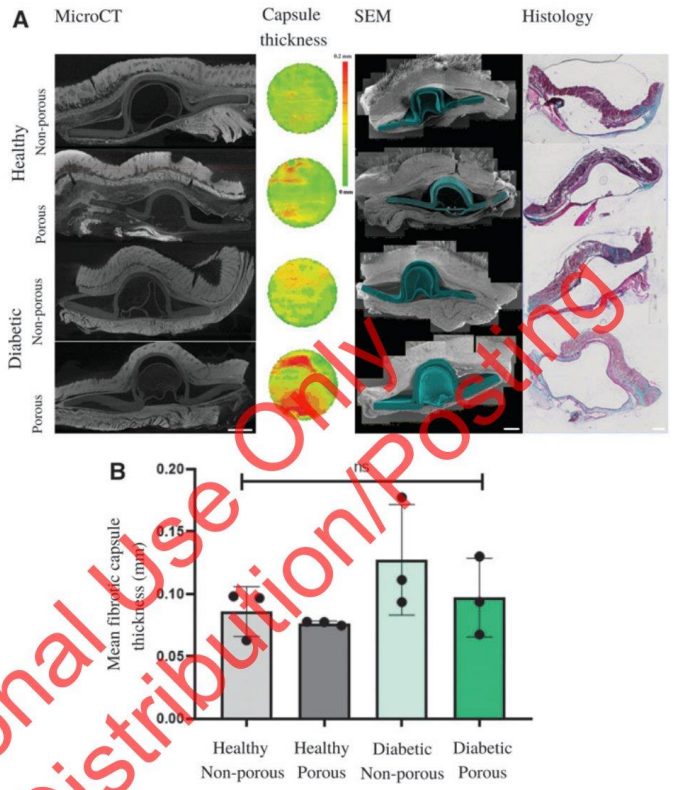

FIG. 2. Quantitative μCT analysis revealed no change in mean fibrotic capsule thickness analysis when comparing healthy with diabetes-induced animals. **(A)** (From *left* to *right*) Coronal slices through μCT dicom files. Fibrous capsule was mapped using segmentation and 3D reconstructions of the area of interest after segmentation can be seen. The color intensity of the circle highlights the thickness of that region (*green* = thin, *red* = thicker). Qualitative SEM reinforced the μCT analysis. Traditional histological methods did not provide us with clear quantitative areas for comparative thickness analysis. **(B)** No statistically significant difference in mean fibrotic capsule thickness is seen across the groups ($p = 0.2350$). $N = 3$/group; one-way ANOVA; mean ± SD; scale bars = 1 mm. STZ-treated animals have a slightly higher overall capsule thickness, indicating a trend toward a higher fibrotic capsule thickness. 3D, three-dimensional; μCT, micro-computed tomography; ANOVA, analysis of variance; SD, standard deviation. Color images are available online.

levels of α-SMA ($p = 0.6965$), Col I ($p = 0.7335$), and Col III ($p = 0.8927$) showed no significant differences between porous and nonporous samples and the diabetic state.

Raman imaging of the fibrotic capsule

ECM Raman reference spectra of α-SMA, Col I, and Col III were generated and validated on IF-stained sections and located in the tissue section by Raman imaging and TCA. The resulting color-coded intensity heat maps recapitulate the distribution patterns and expression levels of the α-SMA (red), Col I (green), and Col III (yellow) for each tissue (Fig. 6A). The morphology of the components shows no structural difference in porous and nonporous groups as well as diabetic and healthy groups. Image quantification demonstrated no significant changes in expression levels of α-SMA ($p = 0.3216$), Col I ($p = 0.2230$), and Col III ($p = 0.4819$) in the fibrotic capsule, which is consistent with the IF data (Fig. 6B–D).

Principal component analysis

Single spectra were extracted from the Col I-positive heatmap regions and further analyzed by PCA with regard to assess submolecular spectral variations. The PC-3 versus PC-1 scores plot demonstrates a cluster formation between collagen structures signatures of healthy and diabetic rats (Fig. 7A). The data of the healthy group significantly shift to the positive PC-3 range compared with the diabetic group (Fig. 7B). Positive peaks in the loadings plot correspond to dominating spectral features found in data with positive PC-3 score values, whereas negative bands provide insight on spectral signatures of the data clustering in the negative score range (Fig. 7B, C). The corresponding PC-3 loadings plot explains the underlying molecular information indicated by peak shifts in the specific wavenumbers (Fig. 7D). The spectral differences were identified at several peak positions. Biological assignments of Raman spectrum are given (Supplementary Table S1). The peak amplitude levels that are relatively higher in the diabetic group than in the healthy group include the 1684 and 1277 cm^{-1} bands (Supplementary Fig. S1A, B), representing amide I and amide III, respectively.[49] Furthermore, peak positions at 1404, 1322, and 1004 cm^{-1} correspond to CH deformation, CH3CH2 twisting of collagen and phenylalanine.[50] Those findings correspond to conformational differences in Col I. The healthy groups showed an increase in these specific peaks compared with the diabetic groups. Of interest, increased peaks in the wavenumber ranging between 820 and 980 cm^{-1} might indicate the presence of advanced glycation end-products

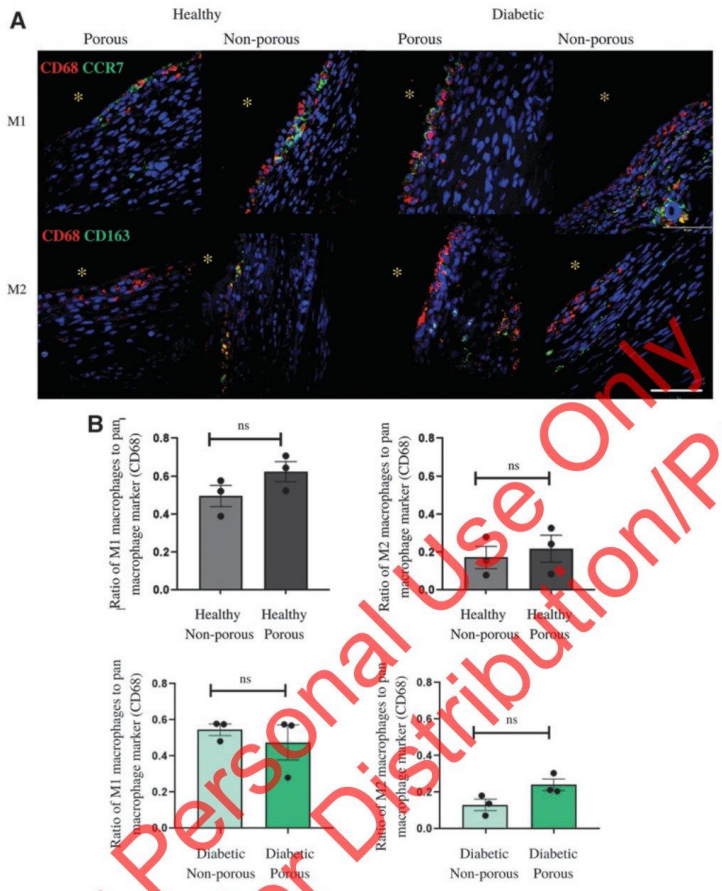

FIG. 3. Pan-M1- and M2- macrophage immunofluorescence staining showed no changes across groups, regardless of porosity or diabetes. **(A)** Representative immunofluorescence images of all groups (M1 panel = *red*, CD68; *green*, CCR7; *blue*, Hoechst) (M2 panel = *red*, CD68; *green*, CD163; *blue*, Hoechst). **(B)** Healthy M1, healthy M2 and diabetic M2 were all normally distributed, diabetic M1 was non-normally distributed and the appropriate statistical analysis was performed for each group. No significant difference was seen across any of the groups (M1 healthy $p = 0.1704$; M1 diabetic $p = 0.4000$; M2 healthy $p = 0.6401$; M2 diabetic $p = 0.0703$). $N = 3$/group; Students *t*-test with Welch's correction or Mann–Whitney *U*-test, mean ± SD. *Yellow asterisk*: implant side; scale bars = 50 µm. Color images are available online.

(AGEs), which were previously shown in diabetic or aging populations.[51] The features identified by RS discriminate the Col I composition between diabetic and healthy groups; however, within both groups no further differences were identified based on membrane porosity variations.

Discussion

The presence of any foreign material in the body will elicit an immune response of varying degree depending on implantation site and properties of the material itself.[52] Understanding this response and employing suitable techniques to overcome the associated response is paramount to the success of any implantable device.

We assess our soft robotic drug delivery device in a diabetic rodent model. Previous studies have shown the potential of this device for sustained, repeated dosing[41] and reduction of fibrous capsule thickness using the drug delivery method itself, in healthy animals.[7] Mimicking the devices environment in preclinical studies is essential for its clinical translation. It has been documented for decades that the diabetic population suffer from immune system dysfunction.[14,53–55] Prior studies revealed that diabetes reduces the FBR caused by the implant,[56,57] including reduced collagen deposition, leukocyte infiltration, pathogen recognition, and cytokine production.[58,59] In this study we have explored a range of biomarkers using several techniques to determine the FBR to our implantable device in a diabetic environment.

The size, shape, and roughness of implantable biomaterials play a pivotal role in the development of the FBR.[60,61] Owing to the unusual shape of this device, the area of fibrotic capsule that is directly in contact with the membranous part of our device is of upmost importance. The entire DSR device is made out of a biocompatible material; however, the membranous region in the DSR device is also smooth and flat, designed as such for optimal drug delivery. We have shown fibrous capsule thickness, in this region, does not differ between healthy and diabetic animals. Understanding the capsular thickness

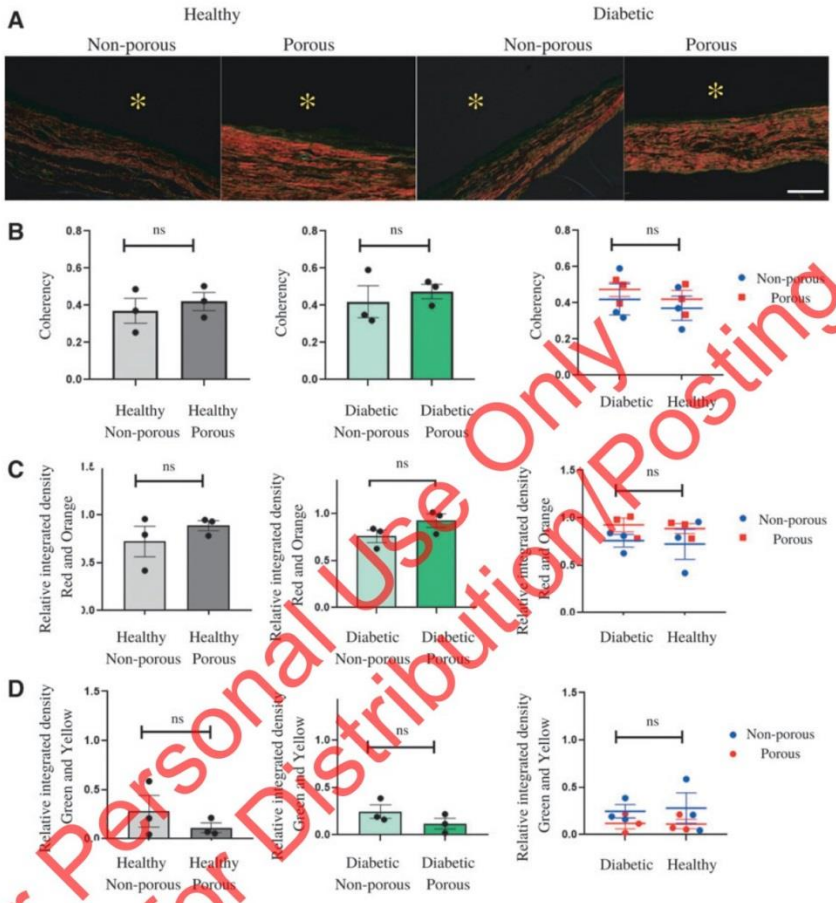

FIG. 4. The overall coherency and collagen maturity was not affected by the diabetic state or porosity. **(A)** Fiber direction and orientation was analyzed using picrosirius red and fast green staining. **(B)** No difference in overall coherency of the fibrous capsule was present between porous and nonporous samples in healthy or diabetes-induced animals (healthy $p = 0.5827$; diabetic $p = 0.5998$; healthy vs. diabetic $p = 0.3997$). **(C)** Mature collagen content was determined by color analysis (*red* and *orange*). No difference was seen between groups (healthy $p = 0.4152$; diabetic $p = 0.1649$; healthy vs. diabetic $p = 0.7190$). **(D)** Immature collagen was characterized by *green* and *yellow* fibers. Diabetes and porosity had no effect on mature and immature collagen content (healthy $p = 0.4086$; diabetic $p = 0.2333$; healthy vs. diabetic $p = 0.8918$). *Yellow asterisk*: implant side; $N = 3$/group; Students *t*-test with Welch's correction, mean ± SD. Scale bars = 100 μm. Color images are available online.

surrounding an implantable medical device for drug delivery is critical.[9] Although μCT analysis allows nondestructive sampling of the fibrous capsule, traditional methods of histological sectioning and imaging (Fig. 2A) results in partial destruction of the capsular area. Therefore, determining the capsule thickness from histological sampling, in this instance, would not provide a reliable estimate, highlighting the importance of whole sample imaging by μCT in analyzing fibrous capsule thickness owing to its nondestructive nature.

Macrophages have been shown to play a pivotal role in the FBR.[17] No change in the ratio of CCR7-positive macrophages was observed between healthy and diabetic samples. Similarly, CD163-positive macrophages showed no changes across the groups. This confirms the incorporation of the device into a diabetic animal does not alter the host's macrophage immune response to the implant, which is consistent with the literature.[62,63] Owing to the highly tuneable nature of our membrane fabrication methods, we were successful in creating pores 10 μm in diameter. Porous implants have been shown to modulate macrophage polarization in the past[42]; however these pores were 15 times larger than the samples in this study, which would not be suitable as an immune-

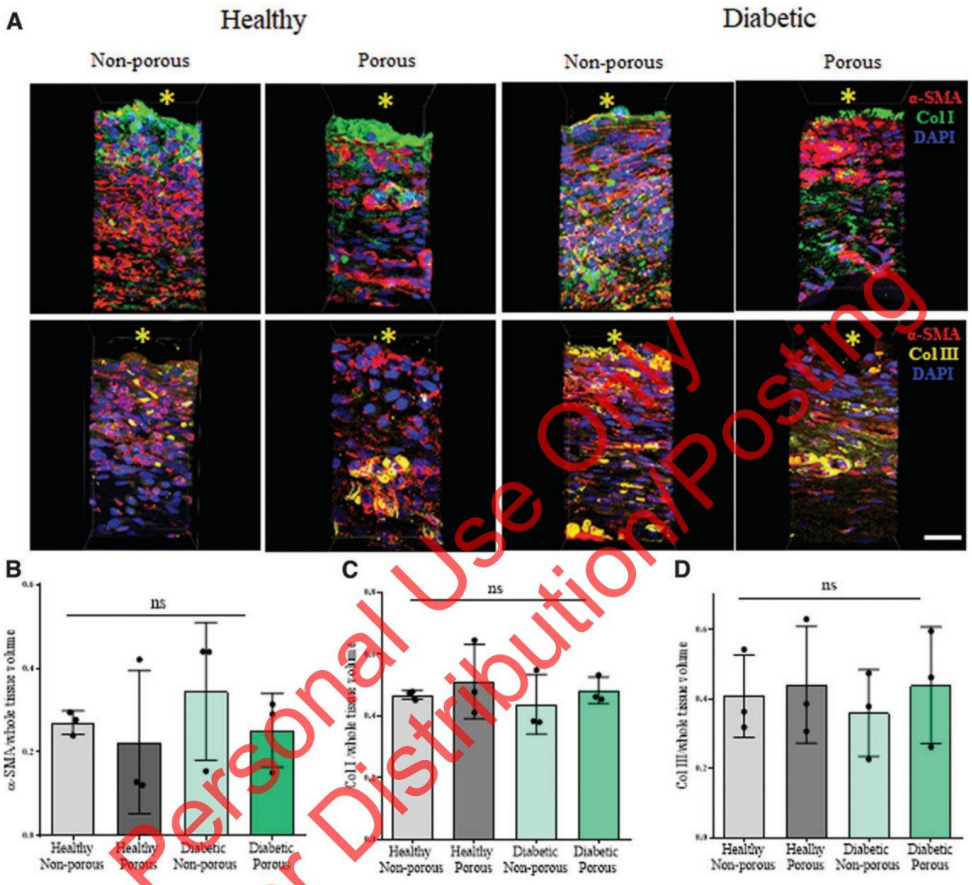

FIG. 5. Three-dimensional immunofluorescence imaging demonstrated the structure of the fibrotic tissue and no expression level differences in the ECM components. **(A)** Z-stack imaging of fibrotic tissue around porous and nonporous implant material in healthy and diabetic animals (*red*, α-SMA; *green*, Col I; *yellow*, Col III; *blue*, DAPI). **(B)** No significant difference was seen in the quantification of α-SMA based on relative distribution in the tissue (ratio to total volume) ($p = 0.6965$). **(C)** No significant difference in protein expression levels of Col I were present ($p = 0.7335$). **(D)** No change in Col III protein expression levels was seen ($p = 0.8927$). *Yellow asterisk*: implant side; $N = 3$/group, one-way ANOVA, mean ± SD; scale bars = 20 μm. ECM, extracellular matrix; α-SMA, alpha-smooth muscle actin. Color images are available online.

protective barrier required for repeated drug delivery dosing. The addition of pores in both disease states does not negatively impact the number of macrophages.

In-depth analysis of fibrotic capsule structures demonstrated high similarities of ECM structures between every group in this study. ECM remodeling and inflammatory response are highly correlated with myofibroblasts. One feature of myofibroblasts is the expression of α-SMA in well-aligned stress fibers.[64] α-SMA involves in myofibroblast maturity, focal adhesion, and scar contraction, although its role in modulating the functionality of myofibroblasts still requires further investigation.[46] The α-SMA expression levels were similar between all groups, indicating no significant additive effects on fibrotic capsule formation directed by membrane porosity or diabetes (Fig. 6B).

Col I and III are the main components of the fibrotic capsule, which were deposited by activated myofibroblasts and fibroblasts.[65] The distribution pattern of Col III in the fibrous tissues is unorganized and randomly distributed (Fig. 5A). It has been reported to show an increased expression in wound and scar tissue compared with normal skin tissue.[66] At the early stage of fibrosis, Col III is secreted dominantly in the fibrotic process and it is relevant to the regulation of the fibrillogenesis.[67] However, for the late stage, the abundant expression of dense Col I is then identified in the fibrous tissues. In addition to quantitative analysis and localization of the proteins, PCA was

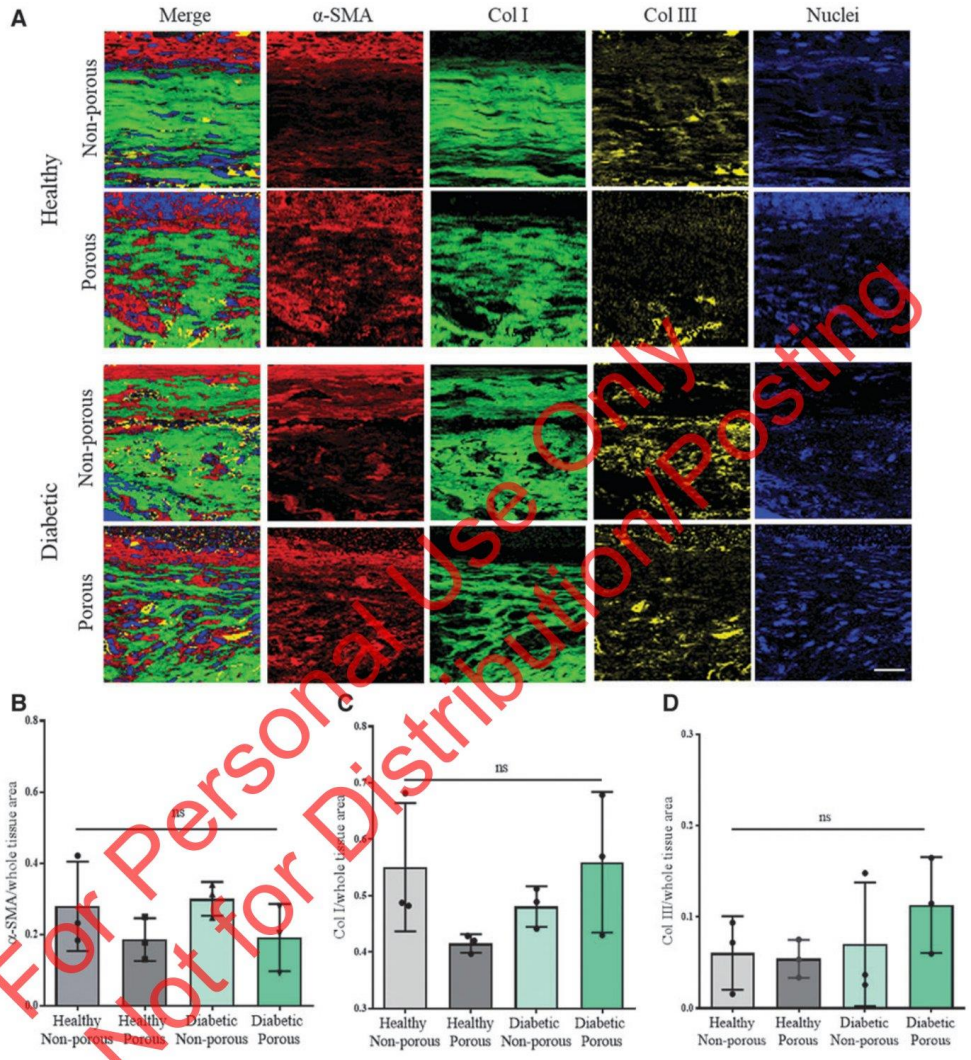

FIG. 6. Raman imaging and quantification showed no difference in the fibrotic capsules in diabetic and healthy animals and membrane porosity variations. **(A)** TCA of the spectral maps acquired of fibrotic tissue sites at porous and nonporous implant material in healthy and diabetic mice localized (*red*, α-SMA; *green*, Col I; *yellow*, Col III; *blue*, Nuclei). **(B)** Quantification of α-SMA based on the relative distribution of the whole area of the tissue reveals no significant differences between implant materials and animal models, respectively ($p = 0.3216$). **(C)** Quantification of Col I based on the relative distribution of the whole area of the tissue reveals no significant differences between the groups ($p = 0.2230$). **(D)** Quantification of Col III based on the relative distribution of the whole area of the tissue reveals no significant differences between the groups ($p = 0.4819$). All the implant sites are on the top of the images. $N = 3$/group, one-way ANOVA, mean ± SD; scale bars = 20 μm. TCA, true component analysis. Color images are available online.

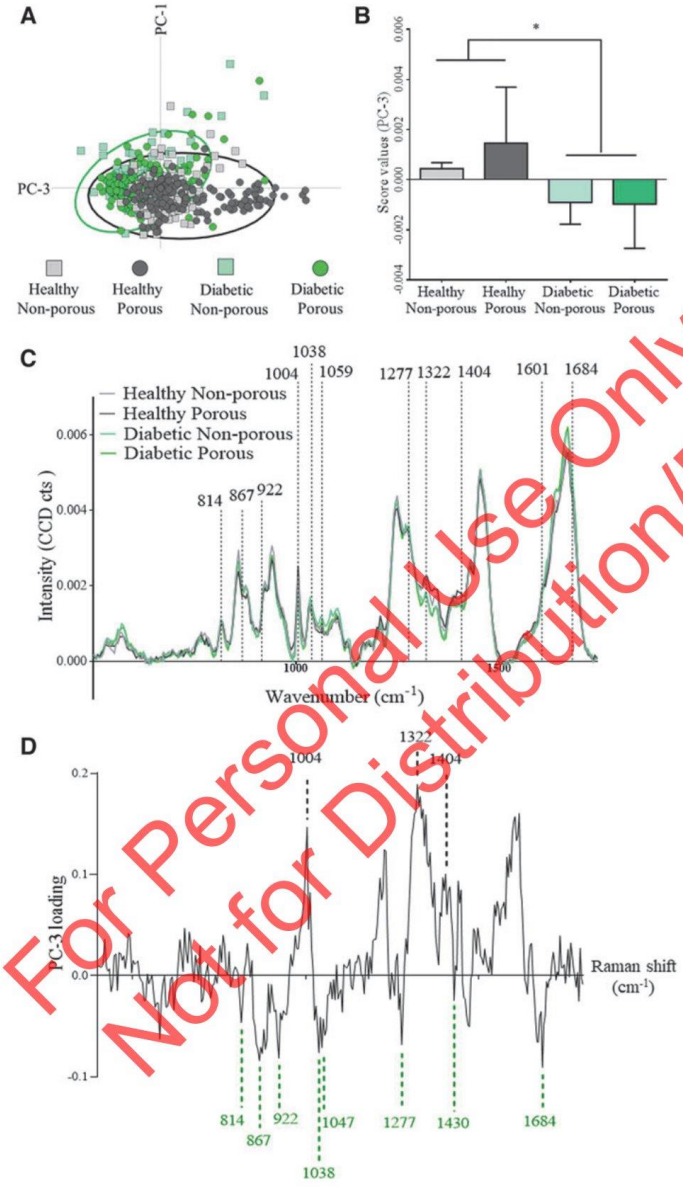

FIG. 7. Multivariate data analysis of fibrotic capsule Col I spectra discriminates molecular features between healthy and diabetic rats. **(A)** PCA demonstrates a separation of Col I features between healthy and diabetic rats but not between porous and nonporous implants in the PC-3 versus PC-1 scores plot. **(B)** A significant separation of score values is demonstrated in PC-3 ($p = 0.0409$). **(C)** Representative Col I spectra extracted from the fibrotic capsule of healthy and diabetic rats. **(D)** Spectral differences contributing to the separation of healthy and diabetic group are indicated in the PC-3 loadings plot. Statistical comparison of the average PC-3 score values showed a significant difference between healthy and diabetic samples but a heterogeneous distribution between porous and nonporous groups. $N = 3$/group, unpaired t-test, mean ± SD. PCA, principal component analysis. Color images are available online.

able to identify a significant separation between healthy and diabetic groups, indicating differences in Col I conformation referring to diabetes but only marginally to the porosity of the selected biomaterials (Fig. 7B). Differences in molecular composition could be assigned to the groups according to correlating peak positions (Fig. 7D). The observed conformational differences might be indicative for the presence of AGEs, which contributes to nonenzymatic glycation on proteins in various conditions such as aging and hyperglycemic environment.[51]

High blood glucose levels in the body might result in glycation of plasma proteins and collagen, causing changes in their

secondary structures.[68] AGEs can induce irreversible cross-linkage between collagen fibers, which might be its physical properties and functionality.[69] Altering peak positions in our study include 1684 cm^{-1} (amide I), 1404 cm^{-1} (CH deformation), 1322 cm^{-1} (CH3/CH2 twisting, collagen), 1306 cm^{-1} (CH3/CH2 twisting or bending mode of collagen), 1277 cm^{-1} (amide III), and 1004 cm^{-1} (Phenylalanine), which are highly related to secondary structure of proteins. Furthermore, peak positions ~814, 867, 914, 1038, 1047, 1277, and 1430 cm^{-1}, corresponding to specific AGEs such as pentosidine and glucosepane, were recognized in the collagen fibers signature of the diabetic group.[70,71]

Recently, RS was utilized to identify the characteristics of AGEs in an *in vitro* study,[72] showing the variability of the particular wavenumbers of AGEs at 1650–1690 cm^{-1} (amide I band), 1225 cm^{-1} (lipids), 1010 cm^{-1} (Tryptophan ring breathing), and 800–1000 cm^{-1} (proline/hydroxyproline).[50] These previous studies support our findings of the significant difference in the PCA.

An interesting question arises based on this phenomenon: Does the AGE-induced structural alteration of Col I affect the FBR caused by the subcutaneous implantation of the DSR device? High expression level of AGEs is commonly observed in diabetic patients. Beside the cross-linked AGEs integrated with proteins such as collagens or hemoglobin, there are also free AGEs in the blood, which are suspected to interrupt molecular function at cellular level by binding to the receptors for AGE (RAGEs).[73,74] RAGEs activation induce the secretion of immunoregulatory cytokines and oxidative stress that are highly related to NF-κB signaling and NADPH oxidase and mitochondrial pathway.[51,75] Based on our results, there is no significant difference in the thickness of the fibrotic capsule, collagen coherency, as well as the ECM and macrophages composition in the different disease states. Furthermore, no studies have directly shown the cross-linkage of AGEs with Col I and those signaling receptors would affect the physical properties of the fibrotic capsule caused by the implants.

In this study, we used several approaches to demonstrate a well-rounded understanding of the diabetic impact on the FBR to our devices, which is comparable with other studies.[7] Moreover, the potential of RS to provide additional insights on the molecular difference across groups has also been highlighted. A main limitation of this study is the single time-point taken at day 14. Although numerous studies report 14 days as being a suitable time point for monitoring the FBR to implanted material,[60,61,76] it is important to determine the immunological engagement over longer time periods. Future studies will investigate the responses to longer term implantations to determine if a change in overall response is present. However, we have shown no change in macrophage content, collagen organization, and maturity and ECM expressions within 14 days. These findings allow us to conclude that diabetes did not influence the FBR to our implantable device.

Acknowledgments

The authors acknowledge the support of the Centre of Microscopy and Imaging, NUI Galway, Senior Technical Officers Mark Canney, Dave Connolly and Emma McDermott.

Disclosure Statement

No competing financial interests exist.

Funding Information

K.S.-L., G.P.D., and C.L. acknowledge funding from the DELIVER project which has received funding from the European Union's Horizon 2020 framework programme under grant agreement ID 812865. G.P.D. and R.E.L. acknowledge funding from the DRIVE project, which received funding from the European Union's Horizon 2020 framework programme under grant agreement ID 645991. R.B. and G.P.D. acknowledge funding from Science Foundation Ireland's (SFI) AMBER centre through their PhD program with grant number SFI/12/RC/2278. R.B. would like to acknowledge funding from the College of Medicine, Nursing and Health Sciences (CMNHS), NUI Galway under a co-funded PhD program with grant number RSF1591. K.S.-L. and C.L. would like to acknowledge funding from the Deutsche Forschungsgemeinschaft, under grant number INST 2388/64-1, Germany's Excellence Strategy, under grant number EXC 2180-390900677, the Ministry of Science, Research, and the Arts of Baden-Wuerttemberg, under grant number 33-729.55-3/214 and SI-BW 01222-91, and the State Ministry of Baden-Wuerttemberg for Economic Affairs, Labour and Housing Construction.

Supplementary Material

Supplementary Figure S1
Supplementary Table S1

References

1. Yu, J., Wang, J., Zhang, Y., *et al.* Glucose-responsive insulin patch for the regulation of blood glucose in mice and minipigs. Nat Biomed Eng **4,** 499, 2020.
2. Vantyghem, M., Koning, E.J.P., De, Pattou, F., and Rickels, M.R. Series type 1 diabetes advances in β-cell replacement therapy for the treatment of type 1 diabetes 6736, 2019. [Epub ahead of print]; DOI: 10.1016/S0140-6736(19)31334-0.
3. Rogal, J., Zbinden, A., Schenke-Layland, K., and Loskill, P. Stem-cell based organ-on-a-chip models for diabetes research. Adv Drug Deliv Rev **140,** 101, 2018.
4. Allen, N., and Gupta, A. Current diabetes technology: striving for the artificial pancreas. Diagnostics **9,** 31, 2019.
5. Morais, J.M., Papadimitrakopoulos, F., and Burgess, D.J. Biomaterials/tissue interactions: possible solutions to overcome foreign body response. AAPS J **12,** 188, 2010.
6. Major, M.R., Wong, V.W., Nelson, E.R., Longaker, M.T., and Gurtner, G.C. The foreign body response: at the interface of surgery and bioengineering. Plast Reconstr Surg 135, 1489, 2015.
7. Dolan, E.B., Varela, C.E., Mendez, K., *et al.* An actuatable soft reservoir modulates host foreign body response. Soft Robot **4,** 7043, 2019.
8. Goswami, D., Domingo-Lopez, D.A., Ward, N.A., *et al.* Design considerations for macroencapsulation devices for stem cell derived islets for the treatment of type 1 diabetes. Adv Sci (Weinheim, Baden-Wurttemberg, Ger) **8,** e2100820, 2021.
9. Oviedo-Socarrás, T., Vasconcelos, A.C., Barbosa, I.X., Pereira, N.B., Campos, P.P., and Andrade, S.P. Diabetes alters inflammation, angiogenesis, and fibrogenesis in intraperitoneal implants in rats. Microvasc Res **93,** 23, 2014.
10. Barrientos, S., Stojadinovic, O., Golinko, M.S., Brem, H., and Tomic-Canic, M. Growth factors and cytokines in wound healing. Wound Repair Regen **16,** 585, 2008.

11. Guo, S., and DiPietro, L.A. Critical review in oral biology & medicine: factors affecting wound healing. J Dent Res **89,** 219, 2010.
12. Falanga V. Wound healing and its impairment in the diabetic foot. Lancet **366,** 1736, 2005.
13. Baltzis, D., Eleftheriadou, I., and Veves, A. Pathogenesis and treatment of impaired wound healing in diabetes mellitus: new insights. Adv Ther **31,** 817, 2014.
14. Broadley, K.N., Aquino, A.M., Hicks, B., *et al.* The diabetic rat as an impaired wound healing model: stimulatory effects of transforming growth factor-beta and basic fibroblast growth factor. Biotechnol Ther **1,** 55, 1989.
15. Seifter, E., Rettura, G., Padawer, J., Stratford, F., Kambosos, D., and Levenson, S.M. Impaired wound healing in streptozotocin diabetes. Prevention by supplemental vitamin A. Ann Surg **194,** 42, 1981.
16. Norris, S.O., Provo, B., and Stotts, N.A. Physiology of wound healing and risk factors that impede the healing process. AACN Adv Crit Care **1,** 545, 1990.
17. Kim, Y.K., Chen, E.Y., and Liu, W.F. Biomolecular strategies to modulate the macrophage response to implanted materials. J Mater Chem B **4,** 1600, 2016.
18. Papadimitrakopoulos, F., and Burgess, D.J. A review of the biocompatibility of implantable devices: current challenges to overcome foreign body response. J Diabetes Sci Technol **2,** 1003, 2008.
19. Sheikh, Z., Brooks, P.J., Barzilay, O., Fine, N., and Glogauer, M. Macrophages, foreign body giant cells and their response to implantable biomaterials. Materials (Basel) **8,** 5671, 2015.
20. Oviedo Socarrás, T., Vasconcelos, A.C., Campos, P.P., Pereira, N.B., Souza JPC, and Andrade, S.P. Foreign body response to subcutaneous implants in diabetic rats. PLoS One **9,** e110945, 2014.
21. Siqueira, M.F., Li, J., Chehab, L., *et al.* Impaired wound healing in mouse models of diabetes is mediated by TNF-α dysregulation and associated with enhanced activation of forkhead box O1 (FOXO1). Diabetologia **53,** 378, 2010.
22. Rai, N.K., Suryabhan, Ansari, M., Kumar, M., Shukla, V.K., and Tripathi, K. Effect of glycaemic control on apoptosis in diabetic wounds. J Wound Care **14,** 277, 2005.
23. Le, N.N., Rose, M.B., Levinson, H., and Klitzman, B. Implant healing in experimental animal models of diabetes. J Diabetes Sci Technol **5,** 605, 2011.
24. Maruyama, K., Asai, J., Ii, M., Thorne, T., Losordo, D.W., and D'Amore, P.A. Decreased macrophage number and activation lead to reduced lymphatic vessel formation and contribute to impaired diabetic wound healing. Am J Pathol **170,** 1178, 2007.
25. Gibran, N.S., Jang, Y.C., Isik, F.F., *et al.* Diminished neuropeptide levels contribute to the impaired cutaneous healing response associated with diabetes mellitus. J Surg Res **108,** 122, 2002.
26. Kharbikar, B.N., Chendke, G.S., and Desai, T.A. Modulating the foreign body response of implants for diabetes treatment. Adv Drug Deliv Rev 2021. [Epub ahead of print]; DOI: 10.1016/j.addr.2021.01.011.
27. Ramírez-Elías, M.G., Kolosovas-Machuca, E.S., Kershenobich, D., Guzmán, C., Escobedo, G., and González, F.J. Evaluation of liver fibrosis using Raman spectroscopy and infrared thermography: a pilot study. Photodiagnosis Photodyn Ther **19,** 278, 2017.
28. Griffiths, J. Raman spectroscopy for medical diagnosis. Anal Chem **79,** 3975, 2007.
29. Pence, I. Mahadevan-Jansen A. Clinical instrumentation and applications of Raman spectroscopy. Chem Soc Rev **45,** 1958, 2016.
30. Mieczkowski, M., Rakowska, B.M., Siwko, T., *et al.* Insulin, but not metformin, supports wound healing process in rats with streptozotocin-induced diabetes. Diabetes Metab Syndr Obes Targets Ther **14,** 1505, 2021.
31. Goodson, W.H., and Hunt, T.K. Studies of wound healing in experimental diabetes mellitus. J Surg Res **22,** 221, 1977.
32. Srivastava, L.M., Bora, P.S., and Bhatt, S.D. Diabetogenic action of streptozotocin. Trends Pharmacol Sci **3(C),** 376, 1982.
33. Dolan, E.B., Hofmann, B., de Vaal, M.H., *et al.* A bioresorbable biomaterial carrier and passive stabilization device to improve heart function post-myocardial infarction. Mater Sci Eng C **103,** 109751, 2019.
34. Coulter, F.B., Levey, R.E., Robinson, S.T., *et al.* Additive manufacturing of multi-scale porous soft tissue implants that encourage vascularization and tissue ingrowth. Adv Healthc Mater **10,** 2100229, 2021.
35. Rezakhaniha, R., Agianniotis, A., Schrauwen, J.T.C., *et al.* Experimental investigation of collagen waviness and orientation in the arterial adventitia using confocal laser scanning microscopy. Biomech Model Mechanobiol **11,** 461, 2012.
36. You, A.Y.F., Bergholt, M.S., and St-Pierre, J.-P., *et al.* Raman spectroscopy imaging reveals interplay between atherosclerosis and medial calcification in the human aorta. Sci Adv **3,** e1701156, 2021.
37. Cárcamo, J.J., Aliaga, A.E., Clavijo, R.E., Brañes, M.R., and Campos-Vallette, M.M. Raman study of the shockwave effect on collagens. Spectrochim Acta Part A Mol Biomol Spectrosc **86,** 360, 2012.
38. Biermann, A.C., Marzi, J., Brauchle, E., *et al.* Improved long-term durability of allogeneic heart valves in the orthotopic sheep model. Eur J Cardiothorac Surg **55,** 484, 2019.
39. Marzi, J., Brauchle, E.M., Schenke-Layland, K., and Rolle, M.W. Non-invasive functional molecular phenotyping of human smooth muscle cells utilized in cardiovascular tissue engineering. Acta Biomater **89,** 193, 2019.
40. Zbinden, A., Marzi, J., Schlünder, K., *et al.* Non-invasive marker-independent high content analysis of a microphysiological human pancreas-on-a-chip model. Matrix Biol **85–86,** 205, 2020.
41. Song, Y., Li, L., Zhao, W., *et al.* Surface modification of electrospun fibers with mechano-growth factor for mitigating the foreign-body reaction. Bioact Mater **6,** 2983, 2021.
42. Yang, J., Zhu, Y., Duan, D., *et al.* Enhanced activity of macrophage M1/M2 phenotypes in periodontitis. Arch Oral Biol **96,** 234, 2018.
43. Jiang, G., Li, S., Yu, K., *et al.* A 3D-printed PRP-GelMA hydrogel promotes osteochondral regeneration through M2 macrophage polarization in a rabbit model. Acta Biomater **128,** 150, 2021.
44. Jan N-J, Grimm, J.L., Tran, H., *et al.* Polarization microscopy for characterizing fiber orientation of ocular tissues. Biomed Opt Express **6,** 4705, 2015.
45. Arun Gopinathan, P., Kokila, G., Siddeeqh, S., Prakash, R., and Pradeep, L. Reexploring picrosirius red: a review. Indian J Pathol Oncol **7,** 196, 2020.
46. Shinde, A.V., Humeres, C., and Frangogiannis, N.G. The role of α-smooth muscle actin in fibroblast-mediated matrix contraction and remodeling. Biochim Biophys Acta Mol Basis Dis **1863,** 298, 2017.
47. Cutolo, M., Ruaro, B., Montagna, P., *et al.* Effects of selexipag and its active metabolite in contrasting the

profibrotic myofibroblast activity in cultured scleroderma skin fibroblasts. Arthritis Res Ther **20,** 1, 2018.
48. Karayi, A.K., Basavaraj, V., Narahari, S.R., Aggithaya, M.G., Ryan, T.J., and Pilankatta, R. Human skin fibrosis: up-regulation of collagen type III gene transcription in the fibrotic skin nodules of lower limb lymphoedema. Trop Med Int Health **25,** 319, 2020.
49. Unal, M., Jung, H., and Akkus, O. Novel Raman spectroscopic biomarkers indicate that postyield damage denatures bone's collagen. J Bone Miner Res **31,** 1015, 2016.
50. Talari, A.C.S., Movasaghi, Z., Rehman, S., and Rehman, I.U. Raman spectroscopy of biological tissues. Appl Spectrosc Rev **50,** 46, 2015.
51. Perrone, A., Giovino, A., Benny, J., and Martinelli, F. Advanced glycation end products (AGEs): biochemistry, signaling, analytical methods, and epigenetic effects. Oxid Med Cell Longev 2020. [Epub ahead of print]; DOI: 10.1155/2020/3818196.
52. Araromi, O.A., Graule, M.A., Dorsey, K.L., *et al.* Ultrasensitive and resilient compliant strain gauges for soft machines. Nature **587,** 219, 2020.
53. Smud-Orehovec, S., Mance, M., Halužan D, Vrbanović-Mijatović, V., and Mijatović, D. Defect reconstruction of an infected diabetic foot using split- and full-thickness skin grafts with adjuvant negative pressure wound therapy: a case report and review of the literature. Wounds Compend Clin Res Pract **30,** E108, 2018.
54. McMurry, J.F. Wound healing with diabetes mellitus. Better glucose control for better wound healing in diabetes. Surg Clin North Am **64,** 769, 1984.
55. Covington, D.S., Xue, H., Pizzini, R., Lally, K.P., and Andrassy, R.J. Streptozotocin and alloxan are comparable agents in the diabetic model of impaired wound healing. Diabetes Res **23,** 47, 1993.
56. Soto, R.J., Merricks, E.P., Bellinger, D.A., Nichols, T.C., and Schoenfisch, M.H. Influence of diabetes on the foreign body response to nitric oxide-releasing implants. Biomaterials **157,** 76, 2018.
57. Schaper, N.C., Apelqvist, J., and Bakker, K. Reducing lower leg Amputations in diabetes: a challenge for patients, healthcare providers and the healthcare system. Diabetologia **55,** 1869, 2012.
58. Berbudi, A., Rahmadika, N., Tjahjadi, A.I., and Ruslami, R. Type 2 diabetes and its impact on the immune system. Curr Diabetes Rev **16,** 442, 2019.
59. Fahey, T.J., 3rd, Sadaty, A., Jones, W.G., 2nd, Barber, A., Smoller, B., and Shires, G.T. Diabetes impairs the late inflammatory response to wound healing. J Surg Res **50,** 308, 1991.
60. Matlaga, B.F., Yasenchak, L.P., and Salthouse, T.N. Tissue response to implanted polymers: the significance of sample shape. J Biomed Mater Res **10,** 391, 1976.
61. Veiseh, O., Doloff, J.C., Ma, M., *et al.* Size- and shape-dependent foreign body immune response to materials implanted in rodents and non-human primates. Nat Mater **14,** 643, 2015.
62. O'Brien, E.M., Risser, G.E., and Spiller, K.L. Sequential drug delivery to modulate macrophage behavior and enhance implant integration. Adv Drug Deliv Rev **149–150,** 85, 2019.
63. Witherel, C.E., Sao, K., Brisson, B.K., *et al.* Regulation of extracellular matrix assembly and structure by hybrid M1/M2 macrophages. Biomaterials **269,** 120667, 2021.
64. Wu, X., Zhao, X., Puertollano, R., Bonifacino, J.S., and Eisenberg, E.G.L.E. Adaptor and clathrin exchange at the plasma membrane andtrans-golgi network. Mol Biol Cell **14,** 516, 2003.
65. Karsdal, M.A., Nielsen, S.H., Leeming, D.J., *et al.* The good and the bad collagens of fibrosis—their role in signaling and organ function. Adv Drug Deliv Rev **121,** 43, 2017.
66. Clore, J.N., Cohen, I.K., and Diegelmann, R.F. Quantitation of collagen types I and III during wound healing in rat skin. Proc Soc Exp Biol Med **161,** 337, 1979.
67. Liu, X., Wu, H., Byrne, M., Krane, S., and Jaenisch, R. Type III collagen is crucial for collagen I fibrillogenesis and for normal cardiovascular development. Proc Natl Acad Sci U S A **94,** 1852, 1997.
68. Khan, N., Bakshi, K.S., Jaggi, A.S., and Singh, N. Ameliorative potential of spironolactone in diabetes induced hyperalgesia in mice. Yakugaku Zasshi **129,** 593, 2009.
69. Hudson, D.M., Archer, M., King, K.B., and Eyre, D.R. Glycation of type I collagen selectively targets the same helical domain lysine sites as lysyl oxidase-mediated cross-linking. J Biol Chem **293,** 15620, 2018.
70. Glenn J V., Beattie, J.R., Barrett, L., *et al.* Confocal Raman microscopy can quantify advanced glycation end product (AGE) modifications in Bruch's membrane leading to accurate, non-destructive prediction of ocular aging. FASEB J **21,** 3542, 2007.
71. Téllez, S.C.A. Confocal Raman spectroscopic analysis of the changes in type I collagen resulting from amide I glycation. Biomed J Sci Tech Res **1,** 629, 2017.
72. Alsamad, F., Brunel, B., Vuiblet, V., Gillery, P., Jaisson, S., and Piot, O. In depth investigation of collagen non-enzymatic glycation by Raman spectroscopy. Spectrochim Acta Part A Mol Biomol Spectrosc **251,** 119382, 2021.
73. Asadipooya, K., and Uy, E.M. Advanced glycation end products (AGEs), receptor for ages, diabetes, and bone: review of the literature. J Endocr Soc **3,** 1799, 2019.
74. Bierhaus, A., Humpert, P.M., Morcos, M., *et al.* Understanding RAGE, the receptor for advanced glycation end products. J Mol Med (Berl) **83,** 876, 2005.
75. Wautier, M.P., Chappey, O., Corda, S., Stern, D.M., Schmidt, A.M., and Wautier, J.L. Activation of NADPH oxidase by AGE links oxidant stress to altered gene expression via RAGE. Am J Physiol Endocrinol Metab **280,** E685, 2001.
76. Vegas, A.J., Veiseh, O., Gürtler, M., *et al.* Long-term glycemic control using polymer-encapsulated human stem cell-derived beta cells in immune-competent mice. Nat Med **22,** 306, 2016.

Address correspondence to:
Rachel Beatty, BSc
Anatomy and Regenerative Medicine Institute (REMEDI)
School of Medicine
National University of Ireland Galway
H91 TK33 Galway
Ireland

E-mail: r.beatty1@nuigalway.ie

Chuan-En Lu, MS
Department of Biomedical Engineering
Eberhard Karls University
Tübingen 72070
German

E-mail: chuan-en.lu@uni-tuebingen.de

Received: August 25, 2021
Accepted: September 13, 2021
Online Publication Date: October 19, 2021

Introduction

Type 1 diabetes mellitus is a metabolic disease characterized by the autoimmune destruction of pancreatic beta cells.[1] The advancements in diabetes treatment have greatly improved in the last decade. However, chronic hyperglycemia and severe hypoglycemic events remain a huge challenge for patients with type 1 diabetes mellitus.[2–4] The move to closed loop insulin delivery systems, along with cell-loaded macro-encapsulation devices may help to alleviate the burden faced by patients.[3] However, the long-term success of many implantable devices, including but not limited to drug delivery devices, is vastly hindered by an altered wound healing process known as the foreign body response (FBR).[5–8]

Several factors can affect wound healing, such as aging, chronic inflammation, therapeutic interventions, and systemic diseases.[9–11] The biological alterations that occur in the diabetic population, such as chronic hyperglycemia, impaired signaling, and circulatory dysfunction, are well documented.[12–15] Implantable medical devices induce chronic inflammation at the site of implantation.[9] Wound healing is a normal biological process involving several highly integrated stages.[10,16] Within minutes, nonspecific protein adsorption to the biomaterial surface initiates a cascade of events. Initially, macrophage recruitment and subsequent polarization to either M1 (proinflammatory) or M2 (anti-inflammatory) phenotypes plays a pivotal role in the host's response.[5,17,18]

The prolonged presence of the biomaterial leads to frustrated macrophages merging to form foreign body giant cells (FBGCs). Both macrophages and FBGCs release cytokines that encourage fibroblasts to deposit collagen around the foreign material, essentially "walling off" the implant from surrounding tissue (Fig. 1A).[17,19] This avascular, collagen-rich layer of tissue prevents the delivery of drugs and molecule diffusion over time, eventually leading to device failure.

In addition, the diabetic environment has been shown to alter the FBR to polyether–polyurethane implants located intraperitoneally. Increases in profibrogenic cytokine (TGF-β1) and inflammatory markers (TNF-α and MCP-1) resulted in alterations in collagen maturity in the diabetic group compared with the control.[9] Other studies revealed that after 10 days, subcutaneous implants in a diabetic model significantly increased TNF-α, MCP-1, and MPO activity but reduced levels of NAG, TGF-β1, and collagen expression.[20] The increase of TNF-α might be related to fibroblast apoptosis, resulting in a decrease in capsule formation.[20–22] It is also reported that the molecular pathogenesis of diabetes is not comparable with healthy groups.[23] The wound healing process in diabetic patients is deficient in chemokines expression, macrophage function, and collagen deposition, affecting the progress of wound closure.[10,24,25]

However, until now, most studies mainly focused on the wound healing process of diabetes, which cannot equally contribute to the understanding of FBR caused by implants in the diabetic population. Manipulating the host tissue through chemical, mechanical, or surface modifications can encourage better integration with reduced fibrosis.[5,17,19,26] Previously, our laboratory has developed a soft robotic drug delivery device, called the dynamic soft reservoir (DSR), which was shown to reduce the mean fibrotic capsule thickness in nonporous devices. An actuation profile was used every 12 h for 14 days in a rodent model. The reduction in mean fibrotic capsule thickness highlighted the potential of this technology to fine-tune the biological host response.[7] Understanding the diabetic response to biomedical implants is essential for improving device longevity.

This study looks at porous versus nonporous DSR devices to determine capsular development surrounding nonactuated devices in healthy and streptozotocin-(STZ) induced diabetic animals. We use micro-computed tomography (μCT) and Raman spectroscopy (RS) to examine the FBR to implantable drug delivery devices in the diabetic subcutaneous environment.[27] RS is a marker-independent method and was implemented here to examine the FBR by analyzing the extracellular matrix (ECM) proteins in the capsule. This label-free technique has the potential to monitor the pathological characterization for the future diagnosis with no invasive surgery procedure and any histological staining.[28,29]

Here, we aim to examine the host's response to our subcutaneous implantable DSR devices by utilization of traditional histological analysis, μCT imaging, and RS with multivariate tools to gain a well-rounded understanding of the diabetic impact on FBR.

Methods Section

Device manufacture

DSR devices were fabricated and sterilized using gamma radiation. The DSR device consists of two separate reservoirs, a therapeutic and actuating reservoir. 0.075 and 0.3 mm thick thermoplastic polyurethane (TPU) sheets (HTM-8001-M and HTM-1001 polyether TPU film; American Polyfilm, Inc.) were formed into hemispherical shapes (Yescom dental vacuum former). Both reservoirs are 3.9 mm in height and 3.5 mm in diameter, with the 0.3 mm TPU reservoir placed inside the 0.075 mm TPU reservoir. Two separate 3F TPU catheter tubing were added to the relevant channels and bonded using heat shrink tubing. The size and shape of the DSR can be easily altered by modifying the three-dimensional (3D) printed molds. The base of the therapeutic reservoir contains a porous membrane. A TRUMF Trumicro 5050 picosecond laser cutting technique with UV 353 nm wavelength was used to generate pores 10 μm in diameter. Pore size, pattern, and density can be varied depending on the specific clinical need (Fig. 1B).

Surgical procedure and implantation

Rodent studies were approved by the Italian Minister of Health (Authorization No. 66/2017-PR) and performed by Abiel Srl (Italy). Six, 12-week-old, female RccHan Wistar (ENVIGO) 150/200 g rats were used during this study. Two weeks before DSR implantation, diabetes was induced using 65 mg/kg STZ intravenously in three animals (Fig. 1C). STZ-induced type 1 diabetes in rodent models has been an established and accepted practice for the study of disease pathology and its associated complications including would healing since the 1960s.[23,30–32] Rats were anesthetized by isofluorane and hair was removed in the area of implantation on the dorsum. Six incisions, three on the left and right of the midline were made in each rat. Three porous and nonporous DSR devices were implanted subcutaneously following enlargement of the surgical incision by blunt dissection